Non-linear Dynamics in ETG Mode Saturation and Beam-Plasma Instabilities

Erinc K. Tokluoglu

Submitted in partial fulfillment of the

requirements for the degree of

Doctor of Philosophy

in the Graduate School of Arts and Sciences

COLUMBIA UNIVERSITY

2014

ABSTRACT

Non-linear Dynamics in ETG Mode Saturation and Beam-Plasma Instabilities

Erinc K. Tokluoglu

Non-linear mechanisms arise frequently in plasmas and beam-plasma systems resulting in dynamics not predicted by linear theory. The non-linear mechanisms can influence the time evolution of plasma instabilities and can be used to describe their saturation. Furthermore time and space averaged non-linear fields generated by instabilities can lead to collisionless transport and plasma heating. In the case of beam-plasma systems counter-intuitive beam defocusing and scaling behavior which are interesting areas of study for both Low-Temperature and High Energy Density physics.

The non-linear mode interactions in form of phase coupling can describe energy transfer to other modes and can be used to describe the saturation of plasma instabilities. In the first part of this thesis, a theoretical model was formulated to explain the saturation mechanism of Slab Electron Temperature Gradient (ETG) mode observed in the Columbia Linear Machine (CLM), based on experimental time-series data collected through probe diagnostics [1]. ETG modes are considered to be a major player in the unexplained high levels of electron transport observed in tokamak fusion experiments and the saturation mechanism of these modes is still an active area of investigation. The data in the frequency space indicated phase coupling between 3 modes, through a higher order spectral correlation coefficient known as bicoherence. The resulting model is similar to [2], which was a treatment for ITG modes observed in the CLM and correctly predicts the observed saturation level of the ETG turbulence. The scenario is further supported

by the fact that the observed mode frequencies are in close alignment with those predicted theoretical dispersion relations.

Non-linear effects arise frequently in beam-plasma systems and can be important for both low temperature plasma devices commonly used for material processing as well as High Energy Density applications relevant to inertial fusion. The non-linear time averaged fields generated by beam-plasma instabilities can be responsible for defocusing and distorting beams propagating in background plasma. This can be problematic in inertial fusion applications where the beam is intended to propagate ballistically as the background plasma neutralizes the beam space charge and current. We used particle-in-cell (PIC) code LSP to numerically investigate the defocusing effects in an ion beam propagating in background plasma experiences as it is exposed to the non-linear fields generated by Two-Stream instability between beam ions and plasma electrons. Supported by theory and benchmarked by the numerical solutions of governing E&M equations, the simulations were used to find and check scaling laws for the defocusing forces in the parameter space of beam and plasma density as well as the beam ion mass. A transition region where the defocusing fields peak has been identified, which should be avoided in the design of experimental devices. We further proposed a diagnostic tool to identify the presence of the two-stream instability in a system with parameters similar to the National Drift Compression Experiment II (NDCX-II) and conducted proof-of concept simulations. In the case of electron beam propagating in background plasma instability driven collisionless scattering and plasma heating is observed. 1-D simulations conducted in EDIPIC were benchmarked in LSP to study the excitation and time-evolution of electron-electron Two-Stream instability. Coupling of electron dynamics via non-linear ponderomotive force created by instability generated fields with ion cavities and Ion-Acoustic mode excitation was observed. Furthermore 2-D simulations

of an electron-beam in a background plasma was performed. Many of the effects in observed in 1-D simulations were replicated. Morever generation of oblique modes with transverse wave numbers were observed in the simulations, which resulted in significant transverse scattering of beam electrons and the time evolution of the turbulent spectrum was studied via Fourier techniques. It is plausible that the modes excited might be interacting non-linearly via mode-coupling, however further theoretical and numerical investigation of the turbulent spectrum is needed. The study of the more realistic 2-D system and the spectrum is important for the understanding of collisionless heating of plasmas by beams and the underlying energy delivery which can have important applications in especially low temperature plasma systems used primarily in etching and materials processing.

Table of Contents:

List of Figures:

List of Tables:

Acknowledgements:

My effort of earning a doctoral degree has been perhaps unusually difficult. In all honesty the blame should be mostly on me but also on the universe. Through the many ups and downs of the past six years, I have shaped into who I am today as a researcher, but more importantly as a free thinking, educated individual. There are many without the support of whom, this journey would be a lot more ardous if not entirely impossible. I would like to take this opportunity to thank them.

First of all I would like to thank my advisor Prof. A.K. Sen for giving me an opportunity to work on the Columbia Linear Machine. After a troublesome first year of graduate school, which was the eventual consequence of my utter lack of self-discipline, he recruited and introduced me to plasma physics which resulted in the publication of a journal paper on the study of slab ETG waves. I would also like to thank Dr. Vladimir Sokolov for his guidance and mentoring. My days at CLM was a crucial part of my training as a plasma physicist and in fact the first few sections I will present in this thesis are an immediate result of that work. Without their guidance and mentoring this research would not have been possible. I would also like to thank (future Dr.) Abed Balbaky and Dr. Xiao Wei for walking the same path with me.

I would like to thank Dr. Igor Kaganovich and Prof. Allen Boozer for giving me an opportunity to conduct research at Princeton Plasma Physics Laboratory. During tough times doing off-campus research was seemingly the only possible way for me to finish my degree and they made it possible, for which I will always be grateful. I would further like to thank Dr. Kaganovich for his supervision and mentoring during my stay at PPPL, also for my introduction to particle-in-cell codes and beam-plasma interactions. I would also like to thank Dr. Edward Startsev, Dr. Alexander Khrabrov, Dr. Yevgeny Raitses and Prof. Ronald C. Davidson for their supervision, Dymtro Sydrenko for his work and guidance on the e-beam reseach and Dr. Dale Welch and Dr. Mikhail Dorf for their support on the pic code LSP which I worked on for 2 years. I would like to thank Elliot Feibush for the preparation of the beamlet-simulation paper

figures, Andrea Moten and the rest of PPPL staff as well. Finally I would like to thank soon to be Dr. Mike Campenall, Anton Stepanov, James Mitrani and Della Wang, for doing the same sort of things that I do and making my Princeton experience pleasant.

Least but not last I would like to thank my family and friends. I should start with my mother, Serap Tokluoglu without the emotional, and also financial, support of whom none of this would be possible. The rest of the family members who I will not list here, your positive reinforcements were always appreciated. As for my friends, I apologize for any omissions, but I would like to thank Dr. Caner Gocmen, Dr. Ahmet Serdar Simsek, Berk Birand, Meric Uzunoglu, Burak Baskurt, Burak Ocal, Soner Bilge, Pamir Ozbay, Dr. Mehmet Saglam, Asli Tuncer, Can Savasan, Ibrahim Ulukaya, Cinar Kilcioglu, Michael Wang, Dr. Noam Ophir, Hande Ozturk, Derya Erdemli, Kerem Tuzcuoglu, Davide Crapis, Enrico Zanardo, Ozgun Saran, Nergis Gulasan, Cengiz Ucbenli Travis Ruscil, Jason Ruscil, Dr. Bora Toklu, Can Erdogan, Ozgun Ozdede, Neset Guner, Semra Comu, Dr. Tolga Bilgicer, Omer Bostanci and Mustafa Ersoy among many others, for their continuos support and friendship. Thank you all very much, it has been a privilege…

To My Family and Friends, without whom

this journey would have been a lot tougher.

Chapter 1

Literature Overview of Drift Waves, ETG Modes and Experimental ETG Studies Conducted in the CLM:

Part 1: Literature Overview of Drift Waves and ETG Modes:

I-Introduction:

Drift waves have in the past years become a study of interest in tokamak plasmas. The major cause of interest is the anomalous particle and thermal transport (in the case of temperature gradient modes) induced by these instabilities. While the ion branch of drift waves like the ITG wave is better understood in terms of transport (ion transport measured and simulated for tokamak plasmas generally agree with the neoclassical limit, ITG saturation and

suppression by mode coupling and effects of zonal flows are better understood), electron transport remains anomalously large. Thus it is important to study modes which may be culpable for anomalously large turbulent transport, one of which is the ETG mode. In this section we will give a brief literature review of of drift waves, providing a quick overview of the underlying theory. We will also look at some of the experimental evidence of their existence in large scale tokamaks, which is applicable to ITER and their effects on turbulent transport. Most of the discussion we present here will be based on the comprehensive literature review of Horton (1999) [5]. The familiar reader can proceed to part 2 of this chapter where we will briefly summarize slab ETG experiments conducted in the Columbia Linear Machine in the previous years.

As we mentioned earlier, drift waves have started to attract more attention due to their influence on particle and thermal transport. In the first part of this chapter we will make an overview of what can be expected in a large scale tokamak like ITER. In Section II we will give a theoretical description of drift waves, the underlying physical principles and the energy drive, the dispersion relation and the question of stability and we will look at the toroidal versions of these modes, those we can expect to see in a tokamak. In Section III we will first look at the observation of these modes in large tokamaks like TEXT and TFTR, and look at simulation results to address questions of saturation, effects of simulation noise and the question of scaling which would be rather important for ITER. In section IV we will make a brief summary of our general overview.

II-Theoretical Background

Drift waves stem from the diamagnetic drift velocity, which is also responsible for creating rotational diagmagnetic current in plasmas. By its nature the diamagnetic drift is a **F**x**B** velocity, where F denotes force. Replacing F with the pressure gradient divided by density , -∇p/n the diamagnetic drift velocity can be derived as:

$$v_{da} = (\frac{1}{e_a n_a B})\ (\partial p_a/\partial r) \quad (1)$$

Where for species a e, n, p denotes charge, density and pressure respectively and B is the magnetic field. If at some radial location r, we have an azimuthal distribution of phase fronts, given by some azimuthal spatial number $k_\perp = m/r$, in other words a wave number, following the simple relation ω=kv, we attain the diamagnetic drift frequency and what we would have is an azimuthally rotating wave, i.e. a drift wave created by the pressure gradient. This is the essence of the drift wave dispersion relation, the diamagnetic drift frequency is thus given by:

$$\omega_{ne}^{*} = \frac{k_\perp T_e}{eBL_n} \quad (2)$$

Eqn 2 gives the diamagnetic frequency for an electron drift mode (its ion counterpart will be in exactly the same form), L_n here denotes the gradient scale length in density, assuming our pressure gradient comes from the density gradient and T_e is the electron temperature. For temperature gradient waves, this gradient scale length parameter L will be of course the temperature gradient scale length. In slab geometry the perpendicular wave number will be given by $k_\perp = m/r$ a mode where m is the azimuthal harmonic number and r is the location of the mode.

Here we will summarize some characteristics of drift waves:

- Drift waves are electrostatic perturbations, $\boldsymbol{E} = -\nabla\phi$ where ϕ denotes the scalar potential,
- They are mostly rotational modes with $k_\perp >> k_{//}$
- The modes are quasineutral since $k_\perp \lambda_D << 1$, where λ_D denotes the Debye Length. This means the spatial variations of the modes are larger than the Debye Length, so in the scale length of drift wave variations quasineutrality is a good approximation.
- The existence of $\mathbf{E}_{//}$ and the electrostatic characteristic imply that the magnetic field lines should be defrosted, since generalized Ohm's law :

$$\boldsymbol{E} + \frac{1}{c}\boldsymbol{v_F} \times \boldsymbol{B} = 0 \qquad (3)$$

  Imply that **E.B**=0. The Defrosting of the magnetic field lines, bring in conditions for plasma collisionality and also set limits on the gradient scale length and the perturbation frequency.

- Drift waves are in fact the weak turbulence solutions to the Hasegawa-Mima Equation, which can be derived from the Drift-kinetic equation including polaziration drift effects and describes the convection of potential vorticity. In the high turbulence limit, where the **E**x**B** (1^{st} order) associated with the fluctuations are large, the solutions take the form of potential vortices.
- Since these modes are electrostatic, for frequencies when the particles would be fast enough to respond to the perturbations, we will employ an adiabatic-like response together with Poisson's equation. For collisionless drift waves, where energy dynamics of the modes is based entirely on resonant particle wave interactions, where the parallel

velocity of the particles match the parallel phase velocity of the wave, Vlasov's Equation is used with Poisson in order to kinetically compute the dispersion relation. This is called a self-consistent Vlasov-Poisson system and is widely used by simulation codes.

- For most cases the density response to potential perturbation is given by:

$$\delta n_{e,k} = \frac{Ne\phi_k}{T_e}\,(1 - i\delta_k) \qquad (4)$$

Where N is zero-order density, T_e is the electron temperature in and ϕ_k denotes a 1st order fluctuation in the scalar potential. Here the delta operator is an anti-Hermitian operator denoting the phase shift between the potential perturbation and density fluctuation. k here denotes a wave number, so in Eqn. 4 the operator is showing the phase shift caused kinetic wave-particle interaction. It is important to note that it is this phase shift that determines whether or not a mode will be growing and in collisional cases, can be created by resistivity which can either create growth or damping, and viscosity which will always create damping. The kinetic delta can of course cause either decay or growth depending on the sign of $\partial f/\partial v$ in velocity space at the point where $v = v_{phase}$. Studying Fig.1 one can see that the **E**x**B** drift created by the perturbation will be along the potential contours and will create a net influx of particles to the phase shifted maximum of the potential perturbation, due to the background density. Depending on the sign of the phase shift, the density fluctuation will either precede or follow the density perturbation, creating a negative feedback effect in the case of a damped mode, and a positive feedback effect in the case of a growing mode.

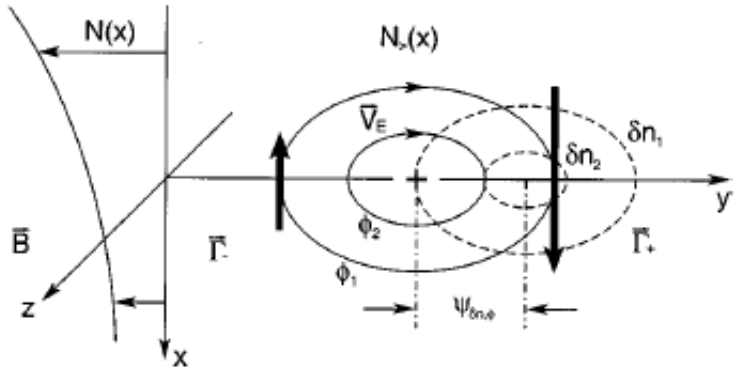

Fig 1 Phase Shifted potential and density fluctuation maxima creating a feedback effect [5]

The same figure with no phase shift between potential and density fluctuation can be used to show that the **E**x**B** convection creates a net flux of particles in the symmetry direction (y in Fig 1), if the time is calculated for a box of length delta y and height of delta x to be filled up by this influx of particles, then delta y be divided by this time, it can be shown that the structure will be propagating in y with the diamagnetic speed [5].

- The particle flux and the thermal flux of species a are given by the following:

$$\Gamma_a = \frac{1}{S} \int_S n_a \boldsymbol{v_E}.d\boldsymbol{a} \quad (5)$$

$$q_a = \frac{3}{2S} \int_S n_a T_a \boldsymbol{v_E}.d\boldsymbol{a} \quad (6)$$

$\mathbf{v_E}$ here denotes the **E**x**B** drift in the radial direction created by the azimuthal E field of the mode since for an adiabatic response the density fluctuation n and the v_E which is $-\nabla\phi/\boldsymbol{B}$ are exactly 180 degrees out of phase, both the particle flux and the heat flux averaged over a magnetic surface in space and time will be identically zero (since we use sinusoidal eigenfunctions for the modes). Thus only when there is a phase shift between the density and the potential will the drift wave create particle and thermal flux, resulting in transport and heat conduction.

The diffusivity created by the modes is neoclassical and the theory is essentially that of quasi-linear diffusion where a group of modes interact with resonant particles with matching parallel velocity and cause them to diffuse radially (on a time average, since n or T is larger in the interior plasma, the net effect is a radially outward flux) outward due to their EXB convection, while decelerating them axially (for an unstable mode). The diffusion coefficient is given by:

$$D = (\frac{\rho_s}{L})(\frac{c\,T_e}{eB}) \qquad (7)$$

$\rho_s = c_s\,\omega_{ce}$ is a larmor radius like quantity with c_s being the sound speed, ω_{ce} is the electron-cyclotron frequency, L is the scale length, c is the speed of light in vacuum, T_e is electron temperature and B is the magnetic flux density as usual.

- It is important to look at the Dispersion relation or the plasma dispersion function for the drift waves to understand the issue of stability. For this analysis we will briefly describe how a dispersion relation for a kinetic drift wave can be calculated, extend it to the temperature gradient case and look at the Nyquist technique and the eta-e/i parameter. Solving the dispersion relation using the Vlasov-Poisson system requires the delta-f

approximation, where we will assume that the background distribution is near-maxwellian and the perturbative delta-f is very small compared to f. Solving delta-f in terms of f using Vlasov Eqn, then integrating in velocity space will give delta n, the density fluctuation, which we can put into Vlasov's equation to get D(ω)φ = 0. Since φ cannot be zero complex ω values with D(ω) = 0 are the solutions of the system. The critical parameter defining stability is:

$$\eta_e = \frac{\partial_r ln\, T_e}{\partial_r ln\, n_e} \tag{8}$$

The η_e parameter, (η_i is analogous in nature). And the Plasma Dispersion function looks like:

$$D(k,\omega) = \Sigma_j \frac{n_j e_j^2}{T_j}\left[1 - \left\langle \frac{\omega-\omega_{*j}(\epsilon)}{\omega-\omega_{D_j}-k_\parallel v_\parallel} J_0^2 \right\rangle\right] \tag{9}$$

J_0 here is a bessel function resulting from gyro-averaging (phase averaging), gyrokinetic Vlasov equation, j denotes species of particles. In this equation

$$\omega_{*j} = \frac{k_y c T_j}{e_j n_j B}\frac{dn_j}{dr}\left[1 + \eta_j(\epsilon - \tfrac{3}{2})\right] \tag{10}$$

$$\epsilon = m_j v^2 / 2T_j \tag{11}$$

By sweeping complex ω in the positive half plane, where the imaginary frequencies are all positive and plotting the corresponding D(ω) in the complex plane we can investigate stability. If area enclosed by D(ω) contains the zero point that means there exists a solution for which D(ω) =0 for our ω values which all had positive real parts, meaning an unstable solution exists. Since the plasma dispersion can be reduced down to a polynomial function with rational coefficients, the rational root theorem dictates that the complex solutions come in stable/unstable pairs. But

we are only interested in growing solutions, since damped solutions with high imaginary will not exist in the plasma unless driven by some non-linear mechanism (i.e. mode coupling). This technique is called the Nyquist Diagram Technique. Fig 2 illustrates a case for which an unstable solution exists:

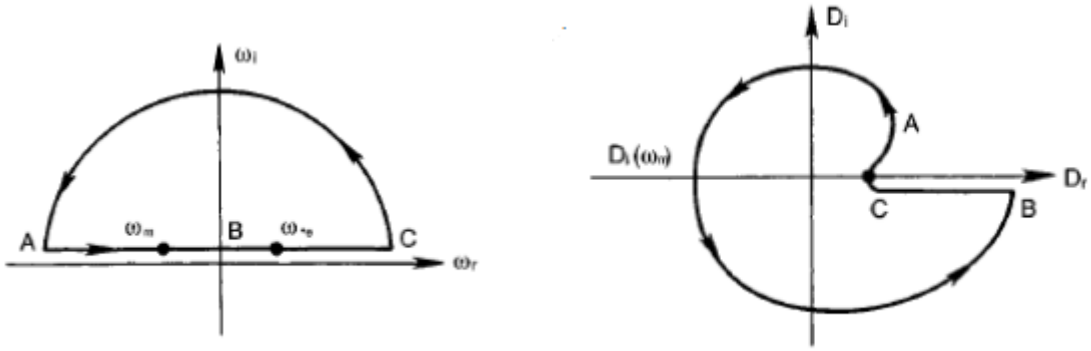

(a) (b)

Fig 2 a- The frequency upper half plane sweep $< 2/3$, b- Plasma dispersion function sweep $\eta > 2/3$.

It can be seen from Fig.2.b that the critical value for η above which unstable solutions exists is 2/3.

Drift wave dispersion relations can be derived from kinetic or gyrokinetic equations (the gyrokinetic equation would be taken moments of by velocity space integration after sometimes multiplying by a velocity containing term to create gyro-fluid equations). The calculation is in essence what we described in this section, and involves the use of Poisson's equation (Vlasov-Poisson system calculations). In the limit of $k_y\rho_s$ <1 , i.e long scale fluctuations the dispersion relation can be simplified to:

$$\omega_{ETG} \approx \frac{1}{2}\left(k_{\parallel}^2 v_{T_e}^2 \omega_{T_e}^* / \tau\right)^{\frac{1}{3}} + i\frac{\sqrt{3}}{2}\left(k_{\parallel}^2 v_{T_e}^2 \omega_{T_e}^* / \tau\right)^{\frac{1}{3}} \quad (12)$$

Here v_{T_e} is the electron thermal velocity and τ is T_e/T_i. This dispersion relation is true for slab geometry. Important thing to note here is that the imaginary part is larger than the real part for these sets of solutions (ITG case will also be analogous) which makes the quick detection and feedback suppression of these modes very difficult.

Since there is a threshold value above which the unstable modes exist, it is not surprising that the modes are local to regions of strong temperature/density gradient. The localization of the modes stems from the fact that due to the density gradient the particle distribution function is no longer uniform in space. Thus a mode can be resonant with the particles at one radial position r, but no longer resonant in r + Δr. This is reflected in the fact that the diamagnetic frequency, which determines the frequency of the modes is a function of L, the scale length of the gradient. Changing the r coordinate from the center of the mode, ω_{Tj} (j denotes ion or electron) and thus ω. Hence $\omega/ k_{//}$ will change with the radial coordinate and at a certain r, the mode will not be resonant or resonant with the particles as to create damping (in the case of ITG, phase velocity can fall to c_s limit, meaning the mode will be strongly landau damped by the ions and cease to exist). The radial width dependence is given by:

$$\Delta r = (\rho_s L)^{1/2} \quad (13)$$

The saturation and suppression mechanism of drift waves are not perfectly understood. It is known however that the zero order EXB rotation break up the potential contours or streamers along which particles diffuse, thus creating suppression. Fig 3. Illustrate this effect:

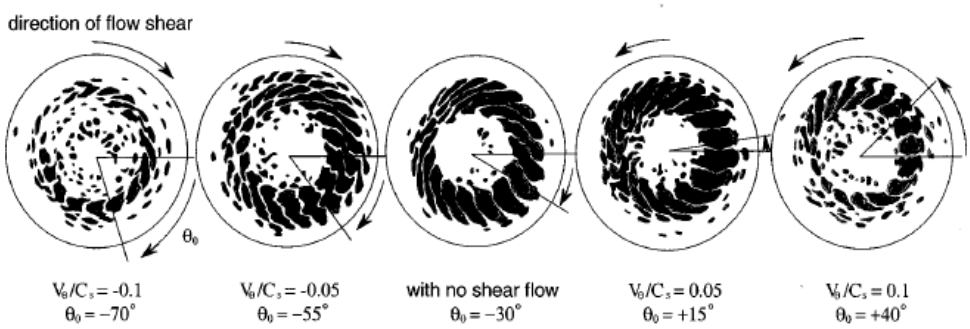

Fig 3 ExB shear flow suppression of drift waves

For ITG modes zonal flows, which are m=0, n= 0 uniform structures with only an imaginary linear frequency, have been shown to have a suppression effect. For ETG modes however zonal flows have been shown to be unimportant. The saturation of ETG modes is under investigation, one of the popular schemes used in simulation codes is the mode coupling of fastest growing modes to the damped ETG modes through 3 wave coupling, under frequency and wave vector matching conditions, thus creating saturation.

Having summarized the drift modes in general, let's take a look at what happens in toroidal geometry. In toroidal geometry, the magnetic field lines have curvature, so in the starting fluid, gyro-fluid or kinetic equations toroidal eigenfunctions should be employed along with the inclusion of ∇B drift in the appropriate continuity and/or Vlasov equations, (Fluid

equations with phase shifted adiabatic response where the phase shift term contain the kinetic effects are sometimes used) to get the drift-wave equation, which will give the same $D(\omega)\varphi = 0$ nature dispersion relation that we seek. We are not going to go any further into the details of these calculations but briefly summarize to very important results. The first important difference is that in toroidal geometry drift wave solutions will exhibit ballooning type behavior and be localized to regions of the plasma, near the plasma edge, where the curvature is destabilizing.

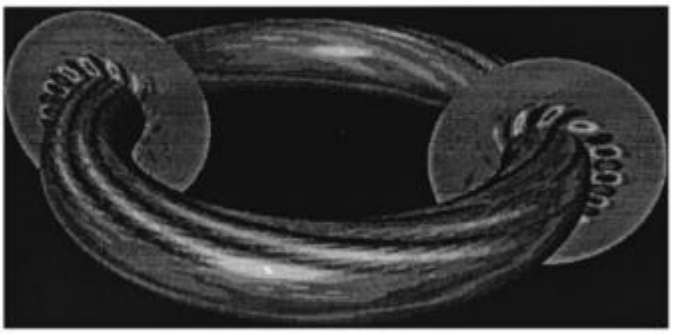

Fig 4 Contours of potentials of drift wave simulation showing localization to the outside of the torus and bad curvature localization.

The second important result is the resonant localization of the modes (resonant to the field lines) and the notion of magnetic shear induced damping. Using the following eigenfunction for the potential fluctuation:

$$\Phi = \Phi(r) + \sum_{m,n} \Phi_{m,n}(r) e^{im\theta - in\phi - i\omega t} + \text{c.c} \qquad (14)$$

where m and n are the polodial and toroidal rotation numbers associated with the mode, θ and ϕ are polodial and azimuthal coordinates respectively and c.c stands for complex conjugates. We

assume that in the tokamak the magnetic field takes the form $\boldsymbol{B} = B_\theta \widehat{e_\theta} + B_\phi \widehat{e_\phi}$ and iota or 1/q will become

$$\frac{1}{q(r)} = \frac{RB_\theta}{rB_\phi} \tag{15}$$

With R being the major and r being the minor radius. This will give the following expression for magnetic shear or the rate of change of the twist of magnetic field lines:

$$s = \frac{r}{q}\frac{dq}{dr} \tag{16}$$

As we noted before, $k_\parallel$is taken to be small for drift waves and $\omega/k_\parallel = v_{phase\parallel}$ determines the wave-particle resonance. Eq. 17 will determine $k_\parallel$ for this toroidal geometry:

$$k_\parallel^{m,n} = -i\,\hat{\boldsymbol{b}} \cdot \nabla ln\Phi_{m,n} = \frac{m-nq}{qR} \tag{17}$$

Eq 17 shows that $k_\parallel$is determined by the difference in the twist of the perturbation and the magnetic field lines. $k_\parallel$being very small is a characteristic of the drift wave and q being a function of r will change with the radial location and as a result $k_\parallel$will increase. In the case of an ion drift wave, an increase in $k_\parallel$will cause the parallel phase velocity to drop to c_s level and strong ion landau damping will kill the mode. Thus q's dependence on r, controls local width of the mode. Same reasoning can be employed for electrons where the change in parallel wave number will throw the mode off resonance. Thus the drift modes in toroidal tokamaks will be localized to magnetic surfaces with matching q, very similar in concept to magnetic islands and their widths will be determined by the rate of change of q with respect to r, or magnetic shear s, giving us the notion of magnetic shear induced damping.

III- Toroidal Drift Modes in Tokamak Experiments and Large Scale Simulations:

We first start by the observation of drift waves in TFTR (Mazzucato, Nazikian) and TEXT(Brower et.al. 1985). Table 1 Shows the applicable drift wave parameters in TEXT and TFTR:

	TFTR	TEXT
Magnetic field	4.8 T	2 T
Major/minor radii	2.45 m/0.8 m	1.0 m/.27 m
Electron temperature	6 keV	500 eV
Density n_e and	$4\times10^{13}\,\mathrm{cm}^{-3}$	$3\times10^{13}\,\mathrm{cm}^{-3}$
Gradient length L_n	20 cm	10 cm
Drift velocity v_d	3×10^{5} cm/s	1×10^{5} cm/s
k scattering experiment	1–20 cm^{-1}	1.5–15 cm^{-1}
ω scattering experiment	10–500 kHz	10–1000 kHz
$\tilde{n}_e/n_e$	5×10^{-3} to 0.02	0.01 to 0.1

Table 1 Drift Wave parameters in TFTR and TEXT.

Brower measured the electron density fluctuation in TEXT using far IR spectroscopy. It is important to note that in the Lab frame, the frequencies are Doppler shifted by the azimuthal 0 order background **EXB** rotation by mv_E where m is the azimuthal mode number and v_E is the azimuthal **EXB** which was measured using HI beam probe diagnostics. The power spectral density measured was in perfect alignment with the quasi-linear drift wave theory and the following measured dispersion was produced.

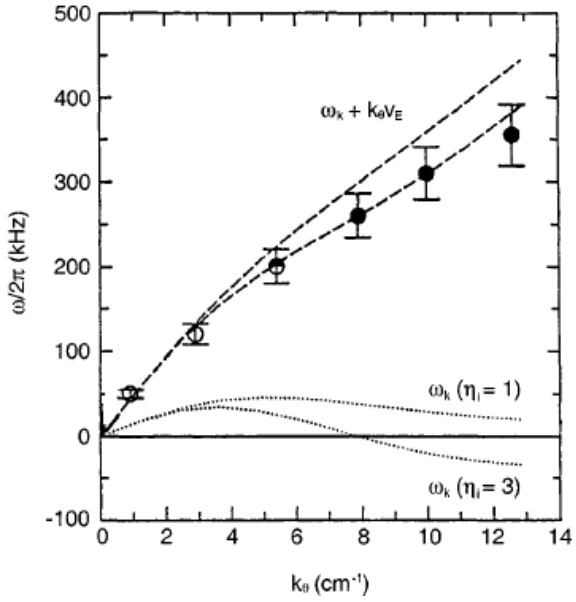

Fig 5 Spectral distribution (Dispersion) measured in the TEXT experiment.

It is important to note that in $k_y\rho_s < 1$ region, the mode frequency grows with k_y (since it grows with the diamagnetic drift frequency) and beyond that region decays, giving a maximum plasma frame frequency the imaginary part of which will be more or less the maximum growth rate. This is very typical of drift wave dispersion relations. The TEXT experiment's lab frame and plasma frame frequency calculations and the corresponding peak (max growth rate at max frequency in the plasma frame) agreement with the theoretical spectral density distribution was shown as incontrovertible evidence to the existence of these modes in TEXT.

In the TFTR experiment, the density fluctuation level n_1/n_0 was measured as a function of auxiliary heating in the core using microwave reflectometry. The increase in the fluctuation level with the increase in neutral beam heating measured at a location r, r/a = 0.3 a being the minor radius, is typical of drift wave turbulence, since stronger heating in the core creates a stronger drift wave which will saturate at a higher saturation level, giving a larger fluctuation in density. Fig 6 illustrates their results.

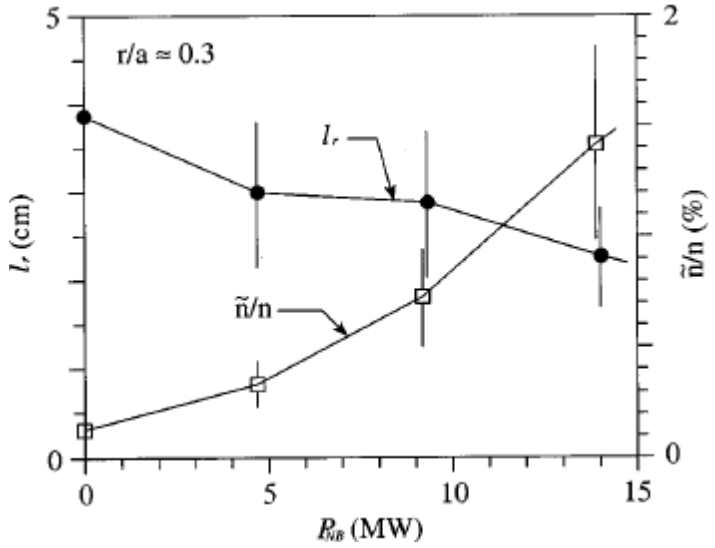

Fig 6. TFTR density fluctuation measurements with respect to increased Neutral Beam heating.

We will now focus on some of the more recent simulation work, that are applicable to ITER. The "Center for Gyrokinetic Particle Simulation for Turbulent Transport in Burning Plasmas" has been selected by the Department of Energy's program of "Scientific Discovery through Advanced Computing (SciDAC) – Advanced Simulation of Fusion Plasmas". This is a combined effort between PPPL, Columbia University, University of Colorado, University of Colorado, University of Tenesse, UC Irvine, UCLA and UCDAVIS. This is a collaborated scientific effort to better understand turbulent transport in fusion plasmas to better understand

turbulence in the regimes of operations for experimental fusion reactors like ITER and to create a framework for fusion simulation projects in the future. They have developed the GTC code (global toroidal code) which is a PIC (particle in cell) simulation code optimized in efficiency for large scale parallel computation complemented by a electromagnetic flux tube code (GEM). The GPSC group has published a number of papers in turbulence simulation addressing issues of particle noise that increases when the number of particles in the simulation is increased. Gyrokinetic Particle in Cell codes trace the velocity and space evolution of billions of particles using parallel computing using a Vlasov-Poisson system, where the particle distributions in space and velocity (through wave-particle interaction and also spatial distribution) result in E-fields through Poisson, the E-fields than accelerate and decelerate particles to modify the particle distributions creating a closed system. Using a large but finite amount of particles brings about the discrete particle noise problem. Using an insufficient number of particles tend to predict lower transport (generally lower in some cases higher)due to numerical noise, as the simulated spectral energy is contained partly in normal modes of the plasma dispersion relation as well, these normal modes being the numerical noise. However in their paper it is shown that they have overcome this problem as they show that they can calculate fluctuation levels independent of N. This is very important for the simulation of a large scale device like ITER which will require very large number of particles for turbulence simulation. Fig 7 shows that their fluctuation levels are independent of N for an slab drift wave simulation.

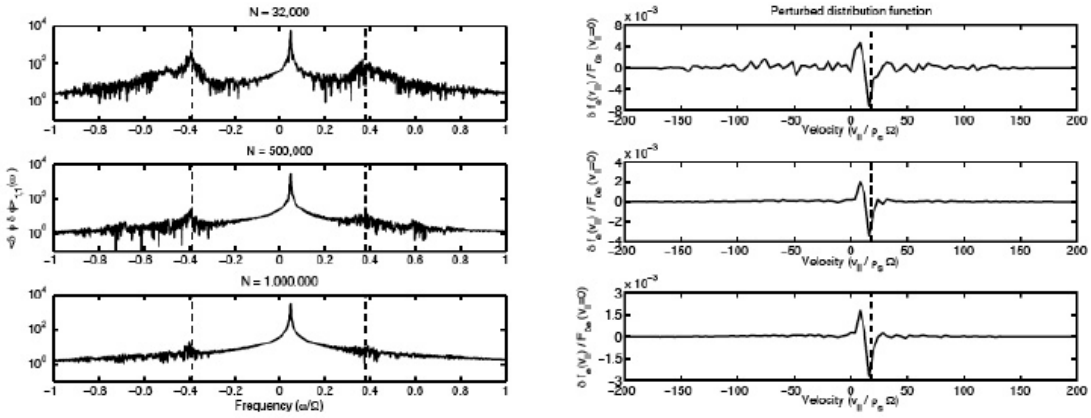

Fig 7 Drift wave fluctuation level simulations with varying N. The high frequency normal modes are suppressed with increasing N, while the low frequency drift mode fluctuation level remains independent of N, thus not having much of a noise issue.

The GTC code has some new interesting findings on the issue of scaling. The GTC simulation code was used to investigate the scaling effect of ETG streamers when the device size is significantly increased. Streamers are radial excursions of constant potential on which particles diffuse in and out due to EXB drift. The expected result of the simulation was to find that the streamers scale with the device radius, thus creating a long path between the core and the outer plasma where electrons would propagate, causing large particle and thermal transport. Their simulation results however indicate that the electrons do not in fact go all the way on these extended excursions and also saturate to within a few percent of T_e. This suggest that these modes will not create the anomalously large electron transport observed in large tokamaks, hinting that ETG modes may not be the only cause for large transport in large tokamaks. Fig 8 is a constant toroidal coordinate surface of their simulation results, where the radial streamers and the azimuthally propagating ETG mode structure is visible.

Part 2: Experimental Studies of ETG Modes Conducted in the CLM

The layout of CLM has been described in Ref. [9, 10]. CLM produces steady-state collisionless cylindrical plasma column in an uniform axial magnetic field (Fig.8).

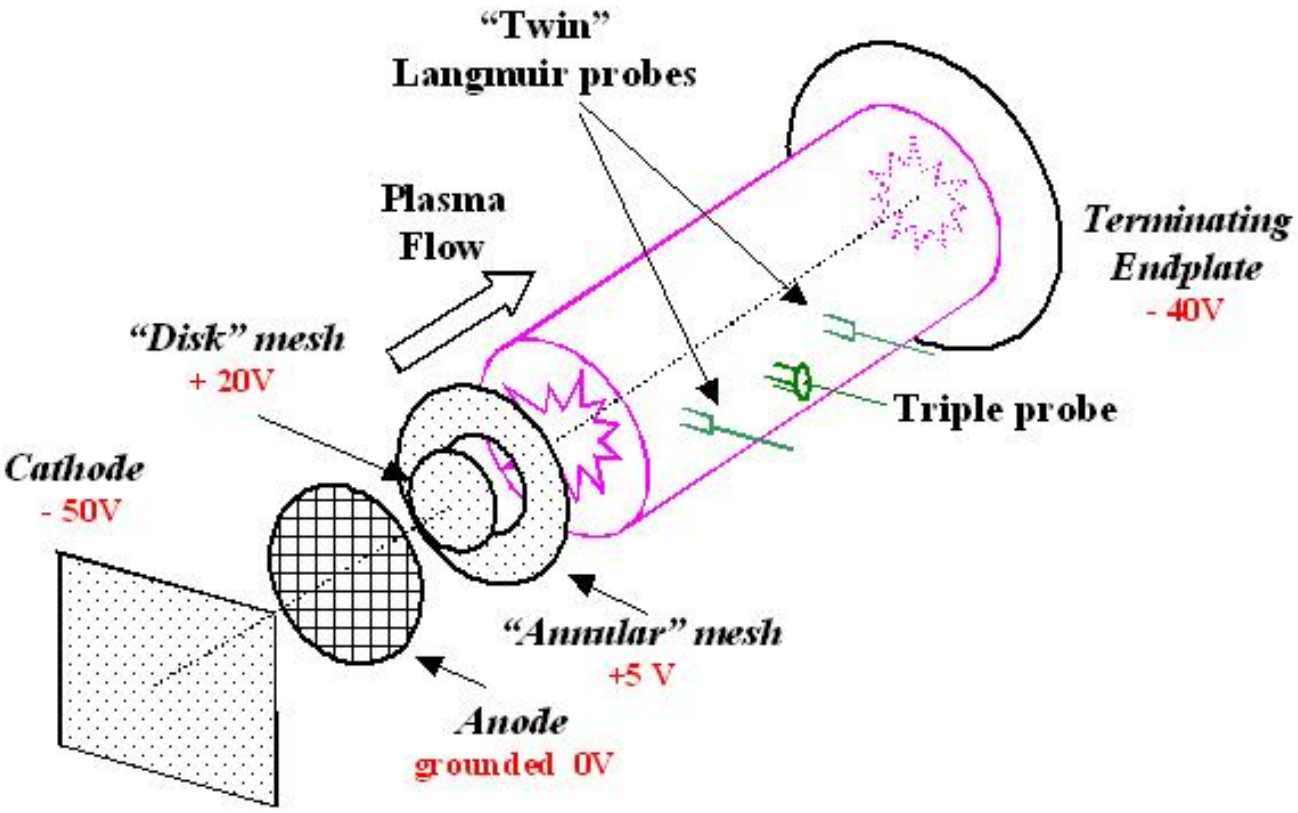

Fig .8. Scheme of CLM and electron heating method.

The typical plasma parameters in CLM are: $n \sim 5\times10^{9} cm^{-3}$, $B \approx 0.1T$, $T_e \approx 5-20eV$, and $T_i \approx 3-5eV$, the diameter of the plasma column is about ~ 6 cm and its length L is about ~ 150 cm, respectively [10]. The scheme of the electron heating method is shown in Fig.8. A positively biased (+20V) disk mesh is placed at the center of plasma column and accelerates the

electrons. The moderate neutral pressure in the transition region guarantees that the accelerated electrons are thermalized to a Maxwellian distribution.

Figure 9 shows the typical power spectra of potential fluctuations. The mode with frequency f ~ 2.4 MHz has been identified as ETG mode with azimuthal wave number *m~14–16* ($k_\perp \rho_e << 1, k_\perp \rho_i > 1$) and propagate in the electron diamagnetic direction. The characteristic of the drift waves, $k_{//} << k_\perp$, is also satisfied by this mode [10].

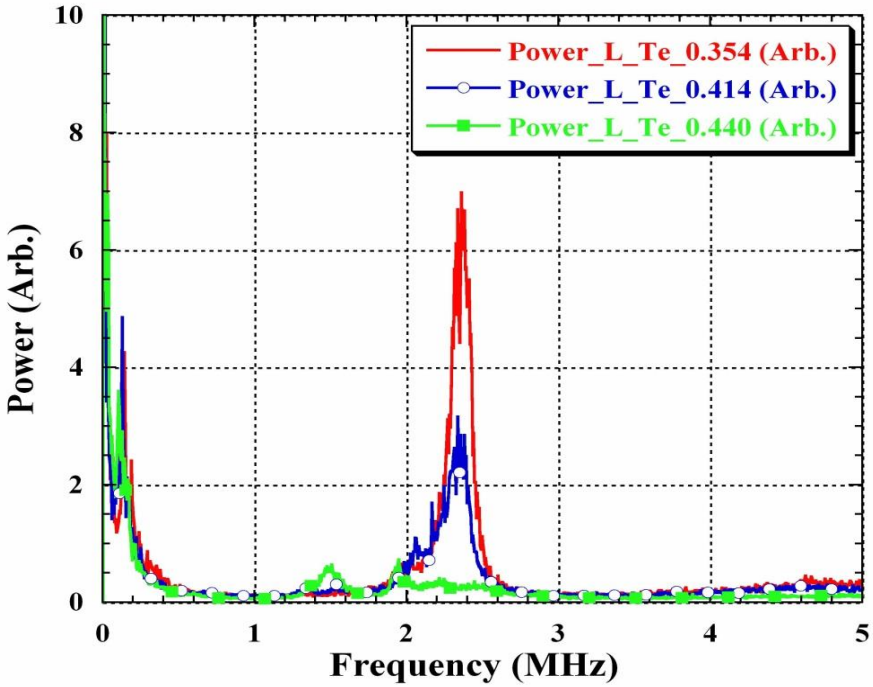

Fig.9. Power spectra of potential fluctuation with different L_{Te}

Chapter 2:

Non-linear Saturation Mechanism of ETG Waves

I-Introduction:

The Electron Temperature Gradient mode (ETG) is a very plausible candidate to explain the large electron particle transport and thermal conduction. Production and identification of slab electron temperature gradient (ETG) modes and measurement electron transport have been already reported [10]. Now we develop a theoretical model of non-linear saturation mechanism of ETG mode based on the three wave coupling of an unstable high frequency ETG mode with a damped ETG radial harmonic and a damped ion acoustic (IA) mode. Bicoherence analysis of CLM data show coupling between ETG modes (~2.4 MHz) and a low frequency mode (~50 kHz). The large damping drive of the ETG radial harmonic accompanied by the smaller but finite damping of the IA mode present an energy sink for the unstable ETG mode, thus causing saturation. This model predicts a saturation level of ~10% and agrees with the observed levels of ETG modes in the CLM.

Electron transport still remains as an unresolved issue for magnetically confined plasmas. The most plausible physics scenario for this anomalous electron transport seems to be based on Electron Temperature Gradient (ETG) instabilities [5,11,12]. In contrast, experimental validation

of theories of electron transport is lacking. Extensive theoretical and simulation work clearly establish its dynamic behavior, both linear and nonlinear [5,13-19].

The number of experiments with identifications of ETG mode and consequent electron transport is very limited [20-22] due to certain diagnostic problems with the high frequency and short wavelengths of electron turbulence.

Production and identification of slab ETG mode have been successfully demonstrated in a basic experiment in Columbia Linear Machine (CLM) [29]. This result has been recently verified partially in numerical simulation [30]. Now we present a new model of nonlinear ETG mode saturation mechanism based on the three wave coupling and the experimental evidence of this mode coupling through bicoherence of potential fluctuations.

This chapter is organized as follows. Section II presents evidence of mode coupling between ETG modes and a low frequency mode. Section III A. presents the derivation of the non-local ETG dispersion relation and shows the radial variation of the drive parameter $1/k_{//} L_{Te}$ will lead to radial harmonics which can explain the existence of the low frequency mode if coupling between radial harmonics happens. In III.B. we present a model to determine the ETG saturation level based on three mode coupling between an ETG mode, its damped radial harmonic and an m=0 IA mode which is the most likely candidate for the low frequency mode. Finally, the conclusion and the discussions are given in section IV.

II- Bispectral Analysis of CLM Data:

In the lab frame the ETG frequencies will be Doppler shifted by the ExB rotation: and $\omega_{ETG\_Lab} = \omega_{ETG\_Plasma} + m\,\omega_{EXB} \sim 2\pi$ (2.4 MHz) for $\omega_{ExB} \sim 2\pi$ (140kHz) ,where m = 15 is the azimuthal mode number. Fig 10 Top shows the fluctuation spectrum where the ETG mode packet at 2.4 MHz and low frequency fluctuations below 100kHz are visible.

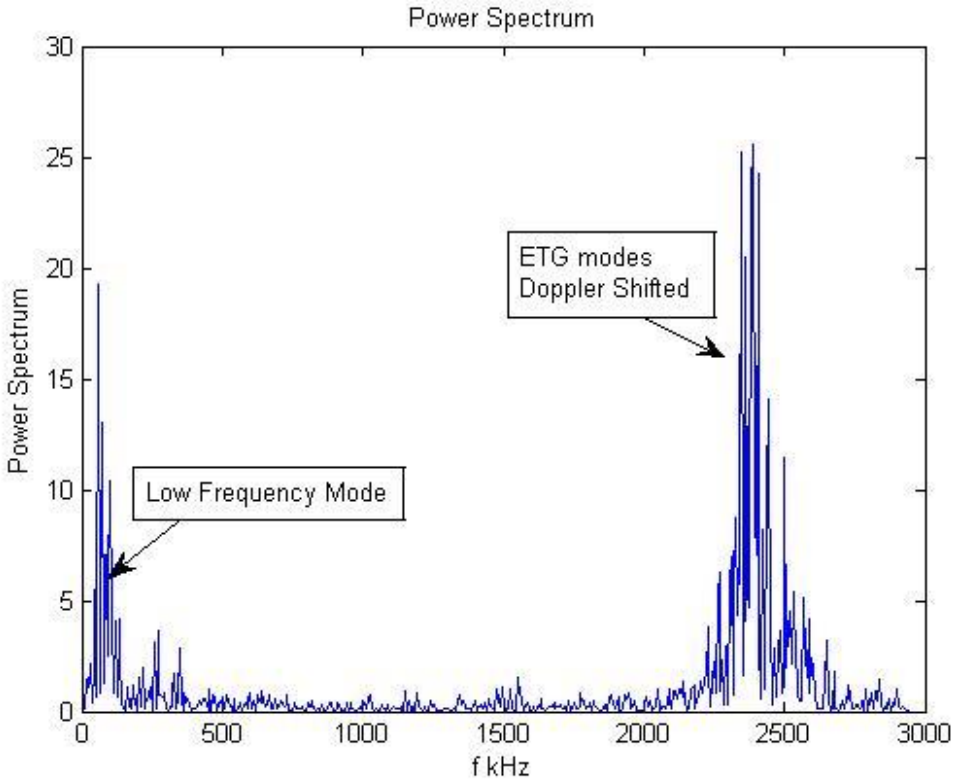

a-

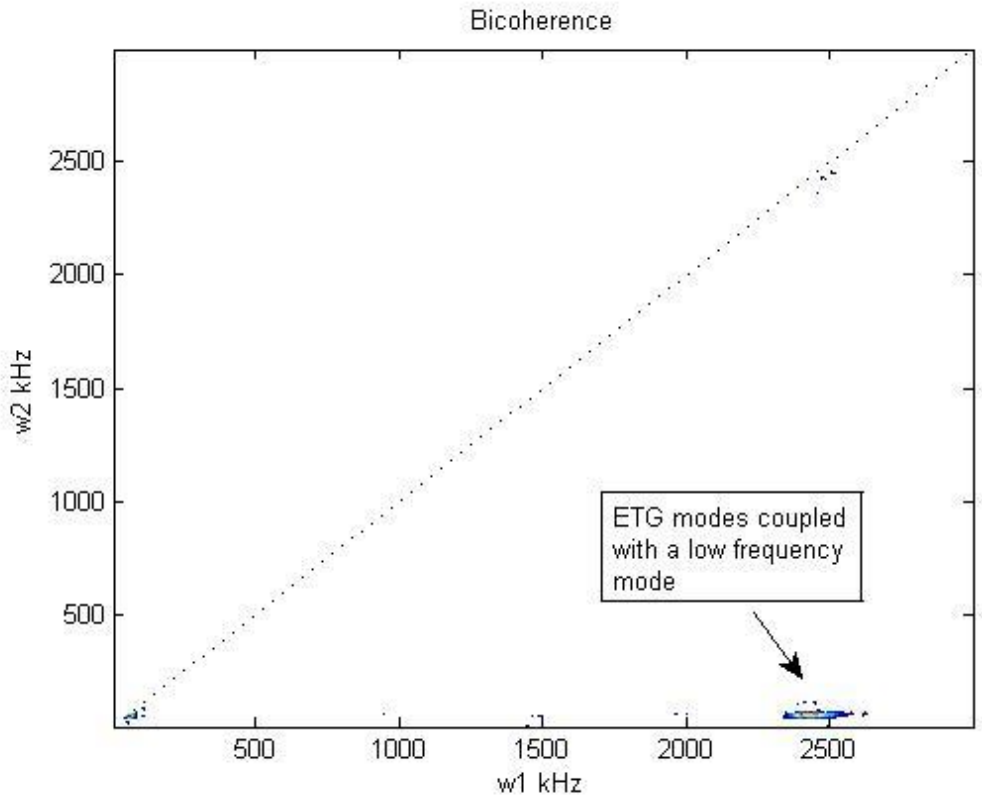

b-

Fig.10. a- Power Spectral Density of CLM potential fluctuations, showing the coexistence of ETG modes with a low frequency mode. B- Bicoherence showing coupling of the ETG modes with a low frequency mode.

Bicoherence is often used as the signature of mode coupling [25] and is given by:

$$b^2(\omega_1, \omega_2) = \frac{|<X(\omega_1)\, X(\omega_2)\, X^*(\omega_1+\omega_2)>|^2}{<|X(\omega_1)X(\omega_2)|^2><|X^*(\omega_1+\omega_2)|^2>}$$

X(ω) here denotes the complex amplitude of the fluctuation spectrum at frequency ω.

Bicoherence is a normalized version of bispectrum that gives the relative phase difference of the fluctuations at 3 discrete additive frequencies averaged over Fourier windows. In the absence of

coupling, this relative phase will be random and average to zero. If coupling is to happen as an independent event in each window, then the relative phase difference from different Fourier windows will be correlated and will converge to a non-zero value, signifying phase coupling.

Figure 10 bottom shows the bicoherence of the CLM fluctuation spectrum. Strong phase coupling of the ETG modes with a low frequency mode is evident.

If we zoom in the lower coupling island and apply a simple filter for the bicoherence noise level, it appears that the strongest coupling interaction occurs between a low frequency about ~ 50 kHz mode and the ETG modes at around 2.4 MHz in the lab frame. Fig.11. shows the bicoherence island corresponding to coupling between ETG modes (~2.4 MHz) and low frequency mode at ~50 kHz. In the next section we will show that this can be explained by the coupling of a ETG mode with its radial harmonic.

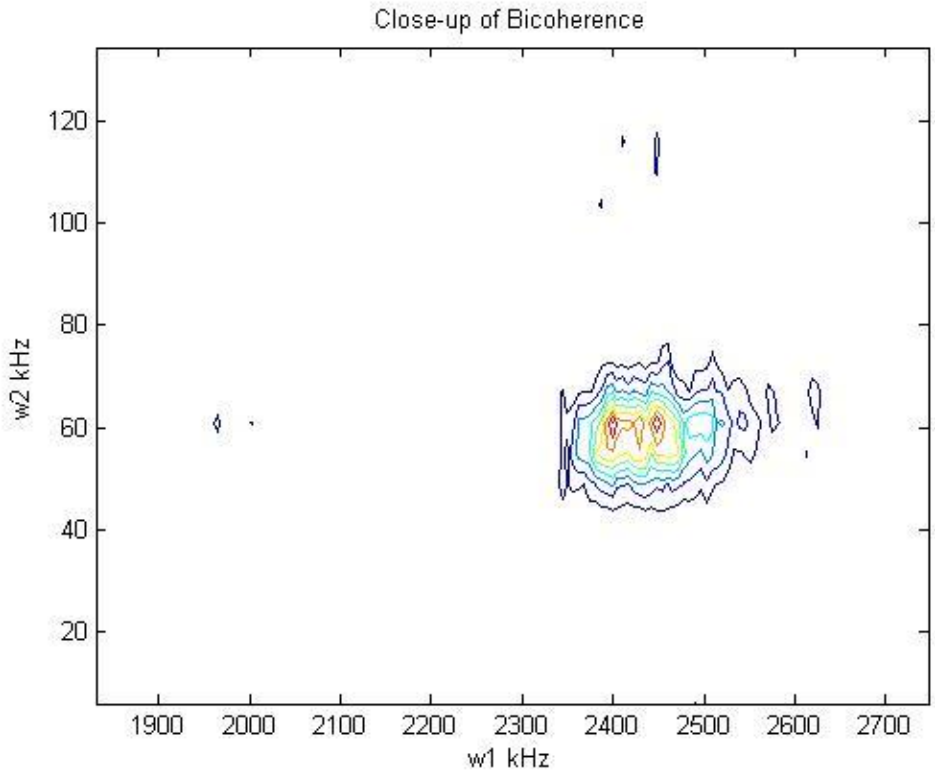

Fig 11. The close-up of Bicoherence. This plot shows strong coupling of the ETG modes with a low frequency mode around 50kHz.

IV. Theoretical Calculations:

A. Dispersion Relation of the ETG Modes:

In this section we derive a dispersion relation for slab ETG modes. In order to derive the dispersion relationship, we start with the following fluid equations which are produced by taking moments of a gyrokinetic Vlasov's equation in anology with ITG radial harmonics [2]. The following fluid equations include ExB non-linearity, non-linearities of higher order are ignored:

$$\frac{\mathrm{dn_e}}{\mathrm{dt}} + \frac{\partial \mathrm{v}_{\parallel \mathrm{e}}}{\partial \mathrm{z}} + (\kappa_{\mathrm{n}} + \frac{1}{\tau} \nabla_{\perp}^{2} (\kappa_{\mathrm{n}} + \kappa_{T_e})) \frac{\partial \varphi}{\partial \mathrm{y}} = 0 \quad (18)$$

$$\frac{dv_{\parallel e}}{dt} + \frac{\partial p_e}{\partial z} - \left(1 + \frac{\nabla_{\perp}^{2}}{\tau}\right) \frac{\partial \varphi}{\partial z} = 0 \quad (19)$$

$$\frac{dp_e}{dt} + \frac{\partial v_{\parallel e}}{\partial z} + (1 + \frac{\nabla_{\perp}^{2}}{\tau})(\kappa_{\mathrm{n}} + \kappa_{T_e}) \frac{\partial \varphi}{\partial \mathrm{y}} = 0 \quad (20)$$

In the above equations we have used the following definitions:

$$L_{T_e} = \left(\frac{\frac{dT_e}{dx}}{T_{e0}}\right)^{-1}, L_{n_e} = \left(\frac{\frac{dn_e}{dx}}{n_{e0}}\right)^{-1}$$

$$\tau = \frac{T_e}{T_i}, \kappa_n = \frac{\rho_e}{L_n}, \kappa_{T_e} = \frac{\rho_e}{L_{T_e}}$$

$$\frac{d}{dt} = \frac{\partial}{\partial t} + \vec{v}_{\vec{E}\times\vec{B}} \cdot \vec{\nabla}, \ \vec{v}_{\vec{E}\times\vec{B}} = \hat{z} \times \vec{\nabla} \varphi \quad (21)$$

Here we have used x,y and z to denote radial r, azimuthal rθ and axial coordinates; $v_{//e}$, n_e , n_{e0} and p_e denote perturbation in parallel electron velocity, perturbed electron density, equilibrium electron density and perturbed total electron pressure respectively. It is also important to note that in the above equations the potential is in the units of T_e/e , all length scales are in the units of ρ_e the electron cyclotron radius and the time scales are in the units of Ω_e the electron cyclotron frequency. The perturbed density n_e is normalized by n_{e0} the equilibrium density. In the CLM the density profiles are nearly flat making L_n go to infinity, thus κ_n can be dropped from the above equations. Assuming that the ions respond adiabatically ($k_{\perp}\rho_i > 1$) we have:

$$\tilde{n_i} = -\frac{e\tilde{\varphi}}{T_i} = -\tau\varphi \quad (22)$$

Since ETG waves are electrostatic in nature, we employ Poisson's equation which under the above conditions becomes:

$$\nabla_{\perp}^{2}\varphi = \widetilde{n_e} + \tau\varphi \tag{23}$$

In Eqns 22,23 $\widetilde{n_e}$ and $\tilde{\varphi}$ denote 1st order density and potential perturbations. For the potential perturbation we will use the following eigenfunction:

$$\varphi = \tilde{\varphi}(x)e^{ik_m + ik_{\parallel}z - i\omega t} \tag{24}$$

In Eqn 24, m denotes the azimuthal mode number, k_m = m/r = 2πm/L is the azimuthal wave number L being the system length in the azimuthal direction. Using Eqns 18-21,24 together with Eqn 23, we obtain the following equation for ETG modes:

$$\frac{d^2\tilde{\varphi}}{dx^2} - \left(k_m^2 - \frac{\left(\frac{k_{\parallel}v_{Te}}{\omega}\right)^2 \frac{\omega_{T_e}}{\omega} + \tau}{\rho_e^2\left(\left(\frac{k_{\parallel}v_{Te}}{\omega}\right)^2 \frac{\omega_{T_e}}{\omega} - 1\right)} \right)\tilde{\varphi} = 0 \tag{25}$$

In Eqn 25 v_{T_e} is the electron thermal velocity and ω_{Te} , electron temperature diamagnetic frequency is given by:

$$\omega_{T_e} = \frac{k_m T_e}{eBL_{T_e}} \tag{26}$$

In the radially local limit, the dispersion relation is obtained by equating the second term in Eqn 25 to zero. Now we proceed to perform the calculations for the radially nonlocal problem. Here we will denote the radial location at which the temperature gradient is maximum as x=0. This radial position will also be the center of the main ETG mode. We then proceed to expand ω_{Te} around its maximum at x=0:

$$\omega_{T_e}(x) = \omega_{T_e}(0) + \frac{\omega''_{T_e}(x)\, x^2}{2} \tag{27}$$

Where '' denotes the 2nd derivative with respect to the radial coordinate x. Using this expansion we find the following differential equation:

$$\tilde{\varphi}''(x) + (A + B^2 x^2)\tilde{\varphi} = 0 \tag{28}$$

$$A = -k_m^2 + \frac{a+\tau}{\rho_e^2\,(a-1)}, B^2 = \frac{(\tau+1)a\omega''_{T_e}}{2\,(a-1)^2\,\omega_{T_e}\,\rho_e^2}, a = \left(\frac{k_\parallel v_{Te}}{\omega}\right)^2 \left(\frac{\omega_{T_e}}{\omega}\right)^3 \tag{29}$$

Eqn 28 is a Weber Equation, the solution for which is known to be Hermite Polynomials, denoted by $H_l(x)$ in this paper, where l denotes the order of the polynomial and the radial mode number of the ETG wave. Thus the full solution for the potential perturbation takes the following form:

$$\tilde{\varphi}(x) = H_l\left(\sqrt{iB}x\right) e^{-\frac{iBx^2}{2}} \tag{30}$$

It is important to note here that in the absence of magnetic shear, the radial width and the localization of the mode will be determined by the radial dependence of the diamagnetic drift frequency [5].Furthermore the following truncation condition for the Hermite Polynomials can be utilized to derive the dispersion relation:

$$A = (2l+1)Bi \tag{31}$$

For long wave perturbations with low azimuthal mode number, i.e $k_m^2\,\rho_e^2 \ll 1$, the dispersion relation becomes:

$$\left(\frac{k_\parallel v_{Te}}{\omega_{Te}}\right)^2 \left(\frac{\omega_{T_e}}{\omega}\right)^3 + \tau = (2l+1)\left(\frac{k_\parallel v_{Te}}{\omega_{Te}}\right)\left(\frac{\omega_{T_e}}{\omega}\right)^{3/2} \sqrt{\frac{(\tau+1)\,|\omega''_{T_e}|\,\rho_e^2}{2\,\omega_{T_e}}} \tag{32}$$

Note here that the term on the left hand side of Eqn 32 is a small correction term. Equating the LHS of Eqn 32 to zero, one can easily obtain the familiar linear ETG dispersion for the central frequency of the slab ETG mode.

$$\frac{\omega_0}{\omega_{T_e}} = \frac{1 + i\sqrt{3}}{2\,\tau^{\frac{1}{3}}} \left(\frac{k_{\parallel} v_{Te}}{\omega_{Te}}\right)^{\frac{2}{3}} \tag{33}$$

Using $\omega = \omega_0 + \delta\omega$ Eqn 16 can be solved perturbatively to give:

$$\frac{\delta\omega}{\omega_{T_e}} = \frac{-\sqrt{3}+i}{6\,\tau^{\frac{5}{6}}} (2l+1) \left(\frac{k_{\parallel} v_{Te}}{\omega_{Te}}\right)^{2/3} \sqrt{\frac{(\tau+1)\,|\omega''_{T_e}|\,\rho_e^2}{2\,\omega_{T_e}}} \tag{34}$$

Thus modes with different radial mode numbers, will have different radial profiles. Since ω_{Te} essentially determines the frequency of the mode and depends on the radial coordinate, a slightly off-centered mode, i.e. a radial harmonic will have a frequency that is different from the fundemental ETG mode (i.e. l=0 mode) by a small but finite amount.

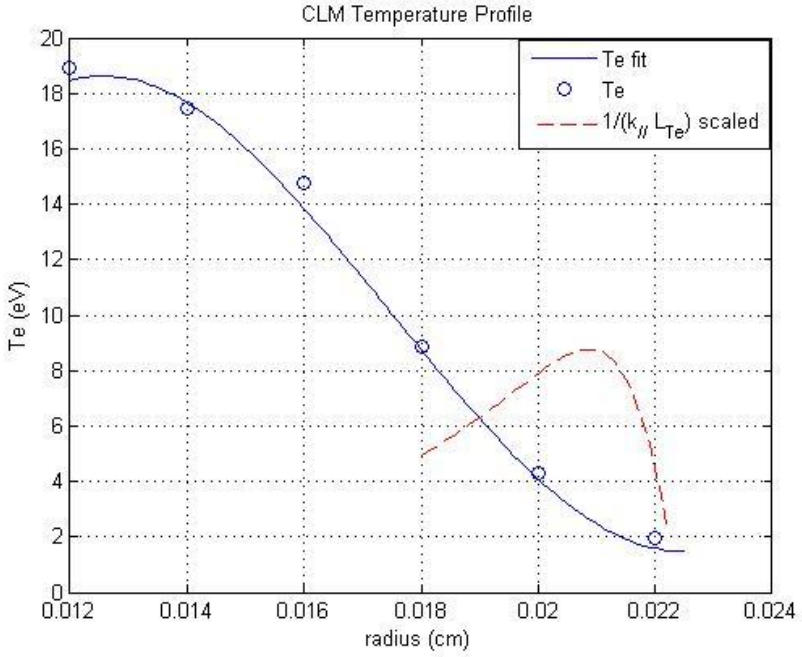

Fig.12. CLM Electron Temperature Profile. The profile shows the maximum drive is around r~ 2 cm and is strongly dependent on the radial coordinate, which will lead to radial localization and the creation of radial harmonics.

Using a typical CLM profile as in Fig.12. we can compute the following parameters $\frac{|\omega''_{T_e}|\rho_e^2}{\omega_{T_e}}$ ~0.0034, L_{Te} ~ 0.2cm, ω_{T_e}~$4.5MHz \times 2\pi$, T_e ~8eV, ρ_e~ 10^{-2} cm which yield a frequency difference $\Delta\omega \sim 2\pi \times (30)kHz$ between m=15, l= 0 mode and m=15,l=1. This shows that the coupling between an m=15 l=0 ETG mode and a m=15, l=1 ETG radial harmonic can explain the existence of phase coupling between 2 ETG modes and a low frequency (~50 kHz) we have shown in Section II. The coupling between these two modes will require that the low frequency mode will be an m=0 mode. Since the frequency of this mode is relatively low, this

mode is likely to be related to ion dynamics. Thus the most likely candidate for the low frequency mode is an ion acoustic mode.

B. Calculation of ETG Saturation Level Based on Three mode coupling:

In this section we will discuss our theoretical calculation of the rms ETG saturation level based on three wave coupling, prompted by experimental evidence. Consistent with experimental observation we consider a suitable three wave coupling to be an unstable m=15, l=0 ETG mode coupling into an m=15, l=1 damped radial harmonic and an m=0 damped IA mode, where m denotes the azimuthal mode number and l denotes the radial harmonic number. As a result of the coupling interaction the unstable ETG mode non-linearly saturates through combined damping drives of the stable ETG radial harmonic and the ion acoustic mode. In order to produce the coupled wave equations we will use two sets of fluid equations, 1st set to describe the high frequency dynamics created by electrons and a 2nd set to describe low frequency dynamics created by ions. We first start with fluid equations describing high frequency electron dynamics [5,27-30]:

$$\frac{\partial n_e}{\partial t} + n_{e0}\frac{\partial v_{\parallel e}}{\partial z} = 0 \tag{35}$$

$$m_e\frac{\partial v_{\parallel e}}{\partial t} = qE_{\parallel} - (\tau n_{e0})^{-1}\frac{\partial p_e}{\partial z} - m_e\,(v_{\perp}\cdot\nabla v_{\parallel e}) \tag{36}$$

$$\frac{3}{2}\left(\frac{\partial p_e}{\partial t} + v_{\perp}\cdot\nabla p_0\right) + \frac{5}{2}\,p_0\frac{\partial v_{\parallel e}}{\partial z} = -\frac{3}{2}\,(v_{\perp}\cdot\nabla)p_e \tag{37}$$

In these equations n_e is the high frequency perturbed electron density of ETG modes, n_{e0} is the equilibrium electron density, $v_{//e}$ is the high frequency perturbation in parallel velocity, $E_{//}$ is the perturbation in parallel electric field, τ is the ratio of electron and ion temperatures, m_e is the electron mass, $v_{\perp e}$ is the perturbation in ExB drift velocity, p_e is the perturbation in electron pressure and p_0 is the equilibrium pressure. Equation 19 is the electron momentum balance in the parallel direction with a ExB convection non-linearity. Finally equation 20 is an energy equation.

Similarly we describe the low frequency ion dynamics in the presence of an IA mode using the following fluid equations:

$$\frac{\partial n_i}{\partial t} + n_{i0}\frac{\partial v_{\|i}}{\partial z} = 0 \tag{38}$$

$$m_i \frac{\partial v_{\|i}}{\partial t} = qE_{\|} - (\tau n_{i0})^{-1}\frac{\partial p_i}{\partial z} - m_i\,(v_{\perp}\cdot\nabla v_{\|i}) \tag{39}$$

$$p_i = \Gamma\, p_0 \frac{n_i}{n_{io}} \tag{40}$$

In equations 38-40 n_i is the perturbation in ion density and Γ is the adiabatic index.

In the first order, the parallel electric field and the parallel gradient of pressure are functions of $k_{//}$ for both ETG drift waves and the IA mode and thus are small. The ExB velocities used in these equations are created by the 1st order electrostatic perturbations of the ETG modes, since for the IA mode the ExB drift is essentially zero. It is important to note that ExB convection due to ETG modes of the perturbation in perturbation in parallel velocity will result in coupling. The ExB drift velocity created by ETG mode j is given by $v_{\perp j} = (-\nabla\varphi_j\, x\, \hat{b})/B$ where φ denotes the potential perturbation created by the ETG mode. The continuity equation for electrons and ions can be used to relate $v_{//}$ and φ, the perturbation in parallel velocity and the

perturbation in potential due to a mode. The high frequency electron continuity equation can be used to give a relation between the high frequency perturbation in the parallel velocity and the electrostatic potential:

$$v_{//j} = \frac{\omega_j q \varphi_j}{k_{//j} T_i} \tag{41}$$

In Eqn 24, we have used an adiabatic ion response and quasineutrality. The index j denotes an ETG mode, either m=15,l=0 or its radial harmonic m=15,l=1..

Similarly the low frequency ion continuity equation produces the following relation for the perturbation in the parallel flow velocity created by the IA mode and the electrostatic perturbation of the IA mode:

$$v_{//IA} = \frac{\omega_{IA} q \varphi_{IA}}{k_{//IA} T_e} \tag{42}$$

Here we have assumed there will be a low frequency background electron response to the IA mode, which will be adiabatic. We have also made use of quasineutrality as before.

It is important to note that for resonant three wave coupling to happen, the mode frequencies and wave vectors have to be commensurate:

$$\omega_i \pm \omega_k = \omega_j \quad , \quad k_i \pm k_k = k_j \tag{43}$$

As discussed in Section A, ETG modes and thus any modes driven by unstable ETG modes will be localized to the region of maximum temperature gradient, approximately r_0 ~2 cm

for CLM with a small radial width and that radial harmonics created by the dependence of ω_{Te} on r will have radial profiles described by Hermite Polynomials [26,27]. In cartesian coordinates where we have substituted $r\text{-}r_0 \rightarrow x$ for the radial coordinate, $\theta r \rightarrow y$ for radial arc length, we have the following eigen functions for the ETG modes:

$$\varphi_j(x,y,z,t) = a_j(t)\varphi_l(x)\exp(ik_m y) + c.c \tag{44}$$

$$\varphi_l(x) = H_l(\frac{x}{\Delta x})\exp(-\frac{x^2}{2(\Delta x)^2}) \tag{45}$$

For the IA mode we have:

$$\varphi_{IA}(x,z,t) = a_3(t)\varphi_0(x) + c.c \tag{46}$$

$$\varphi_0(x) = \exp(-\frac{x^2}{2(\Delta x)^2}) \tag{47}$$

Where m is the azimuthal mode number, $k_m = 2\pi m/L$ is the azimuthal wave number as before, L is the system length in y, H_l is a Hermite polynomial of order l describing the radial mode profile and $\Delta x \sim \rho_e^{\,2}(|\omega_{Te}''|\rho_e^2/2\omega_{Te})^{-1/2}$ is the radial mode width due radial dependence of $\omega_{Te,}$ as described in Sec A. the diamagnetic frequency due to electron temperature gradient, with respect to x, " denotes 2nd derivative in x, and ρ_e denotes the electron gyro-radius and c.c. denotes the complex conjugate. Inserting expressions for $v_{\perp j}$, $v_{//j}$ (Eqns 40-42), the mode eigenfunctions (Eqns 44-47) into the momentum balance equations (Eqns 35,38) and using the resonance condition (Eqn 43) as a selection rule we derive the following coupled wave equations after significant manipulations:

$$\frac{da_1}{dt} = -\frac{\omega_3}{\omega_1}\frac{k_{//}}{k_{//IA}}\frac{T_i}{T_e}\frac{k_m A_1 a_2 a_3}{\Delta x B} + \gamma_1 a_1 \tag{48}$$

$$\frac{da_2}{dt} = \frac{\omega_3}{\omega_2}\frac{k_{//}}{k_{//IA}}\frac{T_i}{T_e}\frac{k_m A_2 a_1 a_3^*}{\Delta x B} - \gamma_2 a_2 \tag{49}$$

$$\frac{da_3}{dt} = \frac{k_{//IA}}{k_{//}}\frac{T_e}{T_i}\frac{k_m A_3 a_1 a_2^*}{\Delta x B} - \gamma_3 a_3 \tag{50}$$

where γ_j is the growth/damping rate of mode j, and $k_{//}$ is the parallel wavenumber of ETG modes and $k_{//IA}$ is the parallel wavenumber of the IA mode .The above equations are derived by spatially integrating the eigenfunctions in the radial coordinate normalized by the mode width $\bar{x} = \frac{x}{\Delta x}$, $< \cdots > = \int d\bar{x}$, to isolate the time dependent complex amplitude:

$$|A_1| = \left|\frac{<\varphi_0 \frac{\partial \varphi_0}{\partial \bar{x}} \varphi_1>}{<\varphi_0^2>}\right| = 0.54 \tag{52}$$

$$|A_2| = \left|\frac{<\varphi_0 \frac{\partial \varphi_0}{\partial \bar{x}} \varphi_1>}{<\varphi_1^2>}\right| = 0.27 \tag{53}$$

$$|A_3| = \left|\frac{<\varphi_0 \frac{\partial \varphi_1}{\partial \bar{x}} \varphi_0> + <\varphi_0 \frac{\partial \varphi_0}{\partial \bar{x}} \varphi_1>}{<\varphi_0^2>}\right| = 0.54 \tag{54}$$

Evaluating the coupled wave equations in steady state by equating them to zero and using the following normalizations for time dependent complex mode amplitudes,

$$X_1 = \omega_1^{1/2}\, e a_1 / T_e, \quad X_2 = \omega_2^{1/2} e a_2 / T_e \text{ and } X_3 = \omega_3^{1/2}\frac{k_{//}}{k_{//IA}}\frac{T_i}{T_e} e a_1 / T_e$$

We put the coupled wave equations into standard form:

$$\gamma_1 X_1 = VA_1 X_2 X_3 \tag{57}$$

$$\gamma_2 X_2 = VA_2 X_1 X_3^* \tag{58}$$

$$\gamma_3 X_3 = VA_3 X_1 X_2^* \tag{59}$$

In the above equations, V denotes the coupling coefficient and is given by:

$$V = \frac{c_s^2 k_m}{\Omega_i \Delta x} \frac{\omega_3}{\sqrt{\omega_1 \omega_2 \omega_3}} \tag{60}$$

Using the coupled wave equations in standard form the rms saturation level normalized by electron temperature is given by:

$$|\phi_{rms}| = \sqrt{|\phi_1|^2 + |\phi_2|^2} = \sqrt{\frac{\gamma_3}{V^2 |A_3|}\left(\frac{\gamma_2}{|A_2|\omega_2} + \frac{\gamma_1}{|A_1|\ \omega_1}\right)} \tag{65}$$

Using the nonlocal dispersion relation we have derived in the previous section Eqn 15 for the ETG modes and using a simple kinetic dispersion relation for the IA mode, the complex frequencies are calculated. Using the complex frequencies calculated this way in Eqn 48, the saturation level is found to be ~ 9%. This result is in agreement with the ETG modes produced in CLM experiments.

Chapter 3:

LSP Particle-In-Cell Code

I-General Introduction:

LSP is an advanced, customizable, multi-dimensional, electromagnetic, fully-kinetic (it can also be run as hybrid), parallelizable particle-in-cell (PIC) code, capable in modeling in 1-D, 2-D and 3-D spatial systems in cartesian, cylindrical and spherical geometries. In this chapter we will give a general description of the code with emphasis on aspects important to modeling plasmas, beams and beam-plasma systems. Developed by Vosscientific, the code comes with a

basic user manual, installation instructions, a graphical user interface (GUI) and a P4 post-processor and detailed information about LSP is readily available [33-36]. It can also be run as a cloud-in-cell code, which is useful for noise reduction which will discuss in more detail when we discuss particle pushers in 3.4.

LSP is written in C in object oriented fashion [35]. Important PIC code elements like grid cells and particles are instances of their respective classes and have added functionality through member functions. Physics related functions are implemented separately and the whole code is linked through the extensive use of header (*.h) files. Object Oriented implementation is extremely sensible for parallelization of the code since different objects are allocated to different CPUs. We will discuss parallelization in more detail in 3.3. The inter-CPU communication is handled using the Multi-Processor Intreface (MPI), Since objects reside in the heap, all memory allocation is fully dynamic and is actively performed during runtime. The source files *.c and the header files *.h are accessible and can be modified by the user which allows the user to carry out modifications as deemed necessary.

II - Compiler Flags and Control:

LSP is an extremely flexible code, capable of running in many different settings, handling different creation models, solvers, pushers and geometries. This extreme flexibility comes from the fact that a new executable is to be created every time a new system is modeled

forsimulation and this executable is specific to the new system described by an input. The input file is a essentially a text file (though the extension is typically .lsp), following a sequential straightforward syntax of setting up important options and parameters in the code, essentially describing the system to be modeled. A user can simply type his/her input file or use the GUI which automatically generates it. The simulation code parses this input file and sets up parameters in the code accordingly. The top portion of the input file is the compiler flags, which are options that customize many important aspects of the code including the geometry, the dimensionality, parallelization, surface interactions and the solver and the pusher to be used. The flexibility comes from the fact the source contains #if n_def COMPILER_FlAG #endif code blocks. These compiler flags are specified in the makedef file (LINUX) in the source code directory and should match exactly with the compiler flags that are referred to in the input file. So everytime a compiler flag is included, the code in between the if-end if block referring to that compiler flag gets compiled. This structure of LSP allows the user to create input specific executables and makes the code extremely flexible and capable of modeling a wide range of physical systems.

The next portion of the input file is the control sequence. This part essentially specifies essential time and time-step dependent parameters of the code including, the runtime, the time step, the diagnostic and restart dump intervals as well as intervals for load balancing which evenly re-allocates macro-particles to CPUs. If an implicit solver is used which is iterative in

nature, implying that the solution is in fact best fit from a regression problem, the maximum number of iterations for convergence as well as the maximum tolerance for the residuals are also specified in this section. If a beam simulation is performed, it may be wise to use the moving frame algorithm, the velocity of the inertial frame and the time this frame starts to move are also specified in this section.

III-Grid, Regions and Domain Decomposition:

Particle-in-cell codes divide the spatial simulation to cells, specified by the grid. This essentially converts the electromagnetic or electrostatic partial differential equations to partial difference equations which are solved using numerical techniques, which we will discuss in 3.5. The particles in the cell are allocated to grid points with a given weight and provide the source terms for the non-homogeneous difference equations. If a particle has contribution to the total charge or the current density at more than one grid point, which essentially changes the "shape" of the macro-particle the code essentially becomes a cloud-in-cell, a feature that LSP supports in a somewhat simplified form. Regardless of this feature, the determination of the grid size is essential to stability and convergence of the solution as well as resolution of physical phenomena such as sub-Debye length dynamics. The grid-size is typically chosen so as to resolve the sheath or the Debye length. LSP supports both uniform and non-uniform grids. One important point to note is that LSP is inherently 3-D in space. This is to say that in lower dimension simulations, the unused dimensions are specified as one cell thick with a length of one centimeter.

If a parallel run is to be performed, the spatial simulation space is divided into regions, which reside on different CPUs. This region split is performed in one direction which can be any direction for higher dimensional simulation. One restriction is that each region should at least be 3 cells thick. Parallelization in LSP requires the multi-processor compiler flag to be turned on and the regions in the input file to be appropriately defined as outlined above. Inter-CPU communication is carried out using the Multi-Processor-Interface protocol. This requires the code to be linked using the mpicc C-linker rather than the standard gcc linker.

IV- Objects and Medium Models:

Surfaces and volumetric objects are defined in the LSP input file under the section Objects. Note that these objects are not to be confused with instances, objects referred to in this section are simply cell properties that are used to define physical structures such as metal walls, dielectric surfaces and vacuum chambers. Objects can either be solid or vacuum. The range of the object is defined by specifying a start and a stop point in each direction. LSP has an inherent property of overriding the object property in the cells. This is to say that if objects overlap, the latter defined objects overrides the property defined by the previous objects. Thus complicated hollow physical structures, such as vacuum chambers, can be defined using sequential definition of solid and vacuum block objects. Once and object is defined it can be given a potential, which will be a Dirichlet type boundary condition for the solver.

LSP also supports medium models. An object can be a conductor or can be made up of a user defined medium. The permeability and the permittivity of the medium are defined as

parameters that are in the units of their free space counterparts. Fig.13. shows the rendering and graphical representation of the simulation physical space prepared to model a hall thruster.

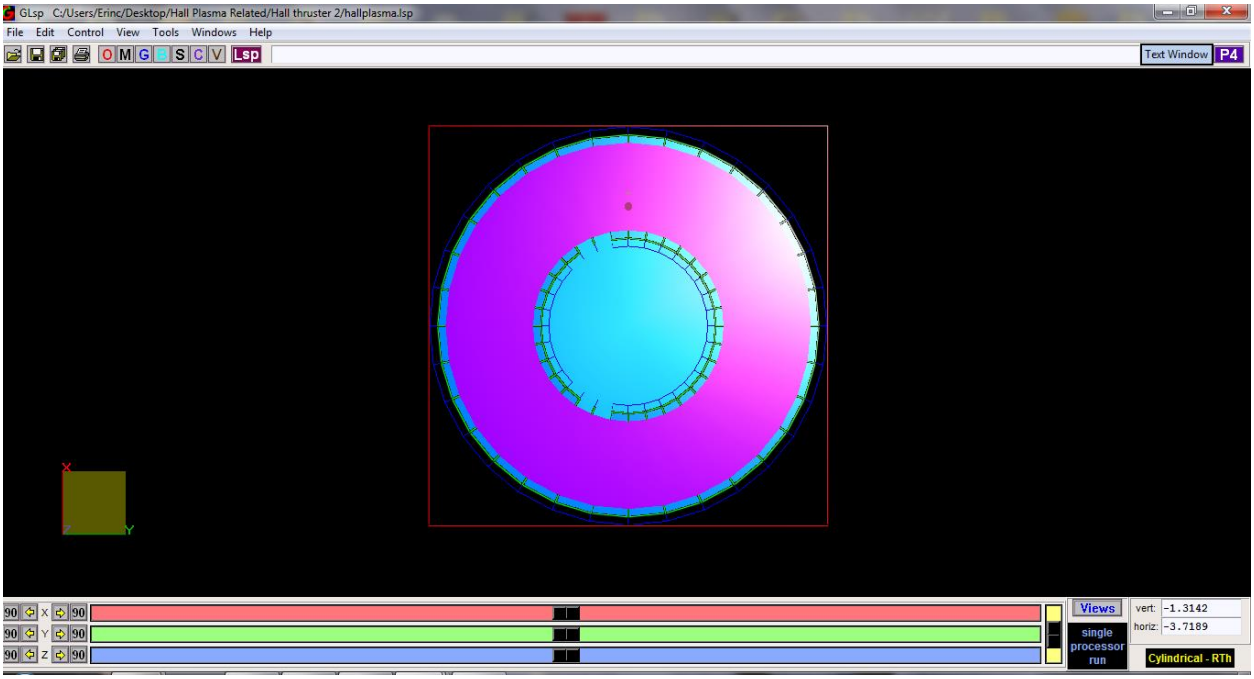

Fig.13. Screen Capture from the LSP GUI showing the rendering of the grid and objects used to model a hall thruster. The outer and the inner rings are user defined dielectric mediums. The space in between these layers, shown in pink, is the vacuum chamber where the plasma resides. The outer square box is a SOLID object defining the initial cell property which is metal in this case.

V- Solvers, Stability Considerations and Particle Pushers

LSP supports a wide range of solvers for both electrodynamic and electrostatic fields. The classical electrodynamic explicit field solver is essentially the well-known leap-frog algorithm. This is a fast solver, however can become numerically Von Neumann unstable if the time step becomes larger than the Courant Limit, where the speed of light is replaced by the

velocity of the fastest moving species in the simulation. LSP also supports a range of implicit solvers, including the Alternating Direction Implicit (ADI) solver which is an extension of Crank-Nicholson Scheme. Implicit solvers are generally more stable compared to explicit solvers in terms of stability. However there is a trade-off as the difference equation matrix becomes non-sparse and non-tridiagonal. Some of the implicit solvers supported by LSP are thus iterative regression solvers, where the solution is a best fit given the maximum allowed number of iterations between time steps and the solution tolerance. LSP also supports a Matrix solver, which requires a linear algebra library and an electrostatic FFT solver which is appropriate for simulations with periodic boundary conditions. Table 2 below is taken from Ref.33 (PPPL notes) and makes a comparison of the electromagnetic field solvers of LSP, in terms of asymptotic complexity and the relaxation of convergence conditions.

Comparison of EM field solvers

Solution technique	Speed	c Δt constraint	ω_c Δt constraint	ω_p Δt constraint	Use/Comments
Explicit	fast	Slightly relaxed with time biasing	< 2	< 2	Default Efficient parallelization
IMPLICIT_FIELDS Iterative ADI	moderate	< 2--4	< 2 with ω_p Δt >1	>> 10	Used with **DIRECT_IMPLICIT**
EXACT_IMPLICIT ADI-Zheng divergence_perserving_flag off	fast	>>1	< 1	>> 10	Used with **DIRECT_IMPLICIT** charge not exactly conserved
EXACT_IMPLICIT ADI-Zheng divergence_perserving_flag on	fast	>>1	<1	>>10	Best for slow moving neutral plasma magnetic divergence not 0
MATRIX_SOLUTION	moderate	< 10	< 5	>> 10	Used with **DIRECT_IMPLICIT**

All these solvers can have a electrostatic fields initialized with field_initialization_flag

Table.2. Comparison of Electromagnetic Field Solvers supported by LSP [36].

There are several particle pushers that LSP uses. The default particle pusher is momentum conserving. The momentum conserving particle pusher suffers from grid heating or the so called Debye Length instability which artificially heats particles until the Debye Length reaches the grid size. There is an implementation for an energy conserving particle pusher which avoids the grid heating problem. Using the compiler flag EXTENDED_PARTICLES, LSP can be converted into a Cloud-In-Cell code. This is a simple CIC implementation where the particle weight is distributed equally to the nearest 2 grid points. The shape of the simulation macro particle is essentially a rectangle of 2 cell thickness. More complicated weighting schemes are known in literature, where the macro-particle shape can be triangular or even a spline. These

weighting schemes are known to reduce numerical noise. More over LSP also has the option of treating the particles implicitly as well, which can be used both in the PIC and the CIC setting. Table.3. below summarizes LSP particle pushers [36].

Comparison of particle movers

Solution technique	Speed	$\lambda_{Debye}/\Delta x$ constraint	$\omega_c \Delta t$ constraint	$\omega_p \Delta t$ constraint	Use/Comments
Momentum conserving	fast	< 1	< 2	< 2	Default *AVERAGED* forces
Energy conserving	fast	>> 1	< 2 with $\omega_p \Delta t > 1$	< 2	*PRIMARY* forces best with EXTENDED_PARTICLES
Cloud-in-cell	fast	>> 1	< 2	< 2	EXTENDED_PARTICLES
Direct Implicit	slower	>> 1	< 5	>> 10	*Best with* MATRIX_SOLUTION

Table.3. Summary of LSP Particle Pushers.

VI. Boundaries, Potentials and External Fields:

LSP supports several boundary conditions for the field solver and the particle pusher. The two most relevant conditions are the outlet and periodic boundary conditions. The outlet boundary condition in the case of an electromagnetic simulation allows an EM wave to leave the simulation domain at the specified surface. When used with an electrostatic solver, the outlet boundary condition turns into a Neumann boundary where the gradient of the scalar potential is specified to be zero. The periodic boundary condition ensures that the fields are periodic at the

two specified surfaces. One other implication of periodic boundaries is that the particles who cross these boundaries re-emerge at the other boundary and thus are recycled. Potentials are defined at surfaces when objects are created. These potentials serve as Dirichlet boundary conditions for the electrostatic field solver when defined.

LSP also supports the inclusion of external fields. One important point to note here is that most physical quantities are specified in LSP through the use of functions. There are more than 30 predefined functions available for the user, where the coefficients are user determined. Using the USE_PYTHON complier option and using a Python-like syntax the user can define his/her own functions. Once constructed, the functions are given reference numbers and physical quantities in the input file are set using these reference numbers. LSP has the innate notion that spatial and temporal dependencies are separable. Thus for almost any given physical quantity including the external fields there is a temporal and a spatial function, the end result for the physical quantity is then determined as the multiplication of these two functions.

VI. Particle Species and Particle Creation Models:

LSP can model any particle species using a class description. The macro particles belonging to a particle species are instances of this class description. Using this class description allows the user to distinguish particles belonging to different physical groups in the simulation, i.e. it is possible to treat electrons of a beam and the electrons of the background plasma as two different species. The particle pusher for the specific species is also specified in this section. When the code is running in hybrid mode, a particle species can be defined as migrant, meaning particles of this class below a certain energy defined by the user will be treated as a “fluid particle”, in other words will not be treated kinetically that is standard of PIC codes. According

to the evolution of their kinetic energies particles belonging to a migrant particle species will migrate between the fluid and kinetically described groups. The mass and the charge of the particles are in the units of the mass of electron and the charge of a positron respectively.

There is a wide range of particle creation models supported by LSP. In this section we will briefly describe those that are most relevant to the simulation of beam-plasma simulations. The first model we will discuss is the plasma creation model. Using this model the user can create particles at the beginning of the simulation in a volume of space within the simulation domain, typically in vacuum. The particle in cell number is specified in each direction. The velocity distribution default is an isotropic Gaussian with zero drift velocity in the plasma model. However one can also define an average fluid velocity functionally. All velocity quantities defined in the code are in the units of gamma-beta product. The density is specified functionally. Beams can be modeled using either an injection model or one of the emission models which include thermal, Child-Langmuir field stress and secondary emission. Creating large potential gradients to extract particles from a surface often result in the fast loss of simulation particles, which have to be resupplied using either an ionization or repopulation model. The ionization model implemented in LSP is an extension of the collisional plasma model and uses Monte-Carlo scattering. However this method requires a user created resource file containing a table of interactions specifying parameters such as collisional cross sections, momentum and energy transfer rates versus the kinetic energy. Hence an accurate description of the ionization of a particular gas is not straightforward. Moreover the loss of faster particles throughout the run of the simulation results in the cooling of the plasma and a lowering of the ionization rate. Thus achieving a quasi-static density level for long simulations using the ionization model is also a major difficulty in LSP. Thus injection is often the most convenient way of simulating a beam

with a given axial directed kinetic energy in LSP. Unlike the plasma model, beam injection is not volumetric, i.e. the beam has to enter the simulation domain from a line or a surface. The particle-in-cell number, distribution and temperature are specified identically to the plasma model. However the density is specified indirectly, by specifying a current density in the units of A/cm^2. The beam profile can be specified by the spatial dependence function of the current density. There is also the option of specifying a convergence length for non-collimated beams.

VII. Diagnostics:

LSP offers a wide range of diagnostic tools for the post-processing of simulation data. The graphical tools for analyzing are written in IDL and output files have .p4 extension. The depending on the requested data, the data is either dumped as a separate file at specified time intervals or can be lumped together. Most common data dumps are the scalars, the fields and the phase space. The scalar data includes densities of certain species and the scalar potential, however for the scalar potential to be computed the solver should be electrostatic, in other words upon calculating the electric field LSP does not separate the field into its electrostatic, i.e. the negative gradient of scalar potential, and electrodynamic, i.e. the negative time derivative of the vector potential in the case of an electrodynamic simulation. Thus in electrodynamic simulations it is not possible to observe the scalar potential. The field dumps contain the data related to the electric field, the magnetic field and the current density at the specified directions. Both the scalar and field data contain data vs spatial field position. This data can be exported to a text file, parsed with a numerical tool package like MATLAB and the further customized analysis can be performed. The phase space data is the compilation of the velocities and the positions of all

simulation macro particles. When plotted in velocity versus position space an individual particle is identified as an individual dot and the whole collection is presented. Velocity versus position data is essential in the observations of velocity space fluctuations which result from plasma instabilities and are also essential in determining saturation mechanism dynamics such as wave-particle trapping. The scalar, field and phase space dumps can be concatenated into movie files which can be displayed using the built-in postprocessor or can be exported to image files which can then be concatenated into a movie file format like .avi for display. LSP also provides data dumps for the distribution function with respect to either velocity in a certain direction or the total kinetic energy. While creating these dumps the user identifies a region of interest in the simulation domain and provides the number of bins which is used to discretize the velocity space. LSP also supports other dumps including energy and charge deposition at surfaces.

In addition to the dumped data, LSP collects data in a separate file called history. The history file can contain a range of information. The most typical data contained in the history file is the probe diagnostics. These are very similar to actually probes in an experiment and display data at a given location versus time. Typical probes can collect field and velocity data and can be taken in a window as opposed to a single point. The history file can also be used to collect global data like total energy, total kinetic energy, total field energy and total macro particle count. The global energy probes can be used to identify whether or not the simulation has energy conservation problems due to numerical mechanisms like grid heating. The macro particle count can become important for long-time scale simulations where one is trying to balance the loss at the walls by a resupply mechanism like ionization to achieve quasi-static levels in density. In addition to global data the history file can be used to observe the number of iterations for convergence and the residuals for simulations where iterative implicit field solvers are employed.

Chapter 4:

Simulation of Ion-Beam Driven Two Stream Instability and its Non-linear Effects.

Part 1: Effects of two-stream instability on an intense ion beam propagating in background plasma.

I-Introduction

The current and charge neutralization of intense charged particle beams by background plasma enables ballistic beam propagation and has a wide range of applications in inertial fusion and high energy density physics. However, beam-plasma interactions can result in the development of collective instabilities that may have deleterious effects on ballistic propagation of the ion beam. We study an intense ion beam pulse propagating in a background plasma, which is subject to two-stream instability between the beam ions and the plasma electrons. Making use

of the particle-in-cell code LSP we have simulated this interaction over a wide range of beam and plasma parameters. We show, depending on the beam and plasma parameters, that there are two different regimes where the instability saturates due to nonlinear wave-trapping effects of either the beam ions or the plasma electrons. Two regimes have different scalings for the self-electric and self-magnetic fields of the ion beam pulse propagating in background plasma.

Beam-plasma systems have a wide range of applications in inertial fusion and high energy density physics. For heavy ion fusion in particular, the background plasma presents a means of current and charge neutralization, enabling the ballistic propagation of the intense beam pulse. However the free energy source presented by the beam can lead to the development of plasma instabilities. The theory of these instabilities was developed using a kinetic framework [37]. The non-linear time-averaged electric and magnetic forces associated with the instabilities can lead to collisionless relaxation and anamolous transport, effects which have been studied numerically using both a Vlasov and a multi-fluid model [38]. In the case of an electron beam propagating in back ground plasma, the non-linear current driven by the mode can result in current enhancement which was demonstrated using a PIC code [39]. and was experimentally observed [40]. In the case of an intense ion beam, the non-linear time-averaged current driven by the two-stream instability between the beam ions and the plasma electrons has been shown to reverse the total current and thus also the self-magnetic field [41]. Thus in the case of a ion beam-plasma system experiencing the two-stream instability both the radial electric field resulting from the pondermotive field pressure of the axial electric field of the mode, and the reversed magnetic field act together to defocus the beam as it propagates. This can have a large deleterious effect for ion beam-plasma devices used in experimental heavy ion fusion. In this work we simulate a H+ beam with beam velocity $v_b = c/2$, where c is the speed of light in

vacuum, propagating in a cold carbon plasma using the particle-in-cell code LSP [42]. We change the ratio of beam density n_b and plasma density n_p and show that this ratio controls the magnitudes of the self-fields at saturation, which in turn determine the defocusing forces the intense beam pulse experiences during propagation.

Part 1 of this chapter is organized as follows. In Sec.II. we give a brief description of the simulation set-up and the particle-in-cell code LSP. In Sec.III. we present a theoretical description of the non-linear self-fields generated by the beam driven two-stream instability and how they depend on beam-plasma parameters. In Sec.IV we present the results from the numerical experiments and make comparisons with theoretical predictions. Finally we summarize the important results in Sec.V.

II- Setup of Simulations:

In this work we simulate an intense Gaussian proton (H+) beam pulse with beam density $n_b = 2 \times 10^{10}\ /cm^3$, pulse duration $t_{pulse} = 12\ ns$ axial directed beam with velocity v_b = c/2 where c is the speed of light in vacuum. The background plasma density $n_p > n_b$ is varied in the simulations, details of which will be discussed in Sec.IV. The radial profile of the intense proton beam is also Gaussian with radius $r_b = 2\ cm$. In the range of simulated background densities n_p, the plasma skin depth δ_{skin} remains smaller than this radius. The simulations are performed using particle-in-cell code LSP using the collisionless plasma model. Thus any radial scattering observed in the simulations is solely due to collisionless scattering of particles due to self-fields. LSP supports multi-dimensional simulations in both phase and physical space. We use LSP in a 2D slab geometry setting in physical space, x denoting the radial extent and z denoting the

direction of beam propagation, and 3D in velocity space with y denoting the azimuthal extent. The field solver used for the simulation is explicit and electro-dynamic with the time step chosen in each particular run to satisfy both the Courant condition and also $\Delta t \ll 1/\omega_k$, where $\omega_k \sim \omega_{pe}$ is the resonant mode frequency and ω_{pe} is the electron plasma frequency of the background plasma, since the resonant mode frequency and the plasma frequency change with the background density. The axial grid size Δz is chosen to satisfy $\Delta z \sim 1/(30k_z)$, where k_z is the resonant wave number, to achieve a fine resolution of the axial mode structure. The radial grid size is fixed at $\Delta x = 0.1\ cm$ which provides enough resolution to observe changes in the beam radius and the radial displacement of beam ions. The domain size for the simulation is x: [-11,11] cm and z: [0,240] cm. We also employ the moving frame algorithm which starts tracking the beam when it reaches the center of the simulation domain which takes 15.5 ns. Figure 14 below is an excerpt from one of the runs showing the beam density pulse profile after the pulse has reached the center of the simulation domain and the moving frame algorithm has started and is descriptive of the physical simulation setup.

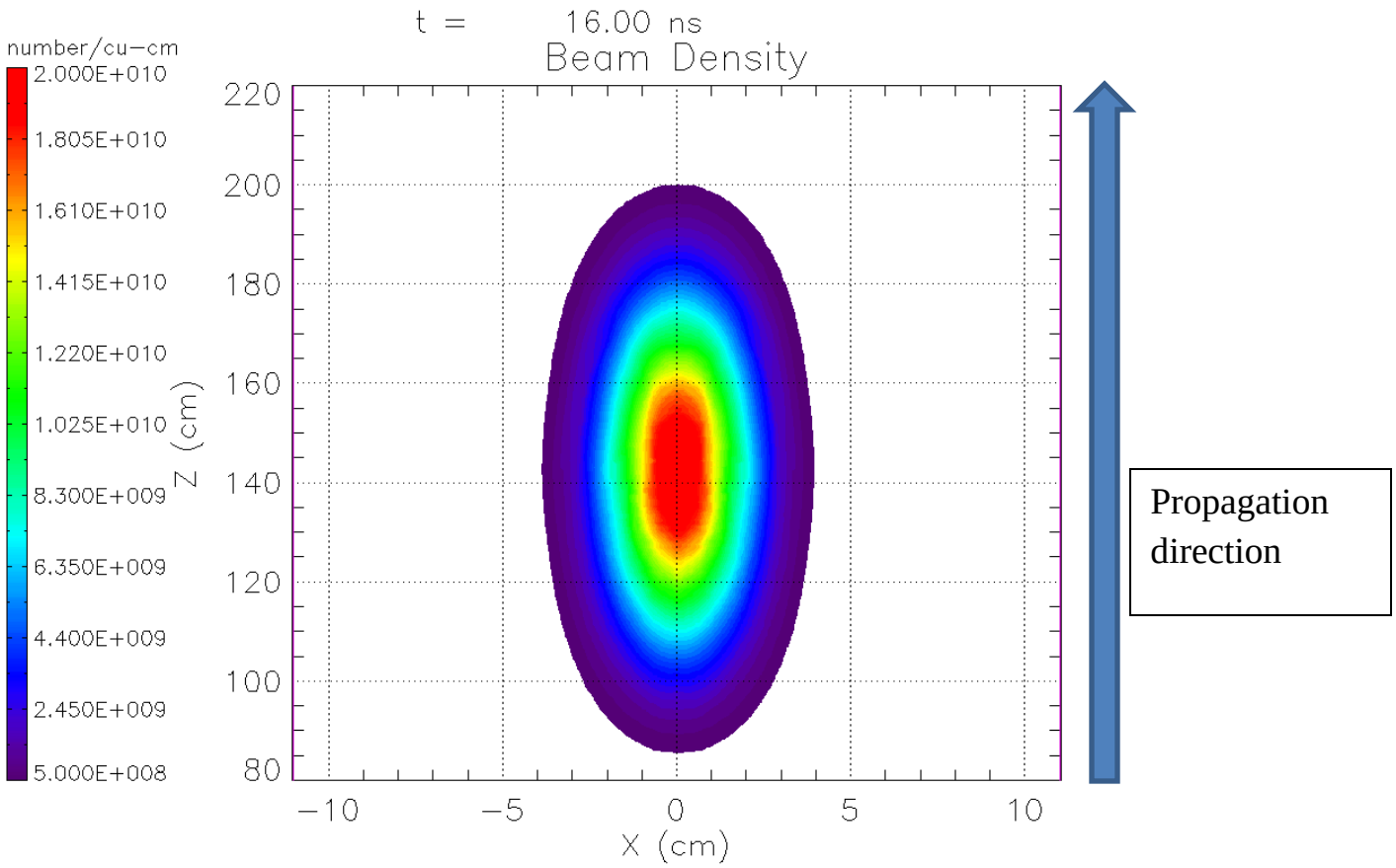

Fig.14: Density Profile prior to instability for $\mathbf{n}_p = 1.0 \times 10^{12}/cm^3$, $n_b = 2 \times 10^{10}/cm^3$, $r_b = 2\ cm$, $t_{pulse} = 12\ ns$, v_b = c/2, t = 16 ns.

III-Non-linear Effects of the Ion Beam Driven Two-Stream Instability:

In the case of an ion beam propagating in background plasma, the beam plasma system will be subject to beam driven two-stream instability between the beam ions and the plasma electrons. The mode will be driven kinetically by resonant beam ions. For a cold plasma and beam, the plasma dispersion function $D(k, \omega)$ for the absolute instability will be:

$$D(k,\omega) = 1 - \frac{\omega_{pe}^2}{\omega_k{}^2} - \frac{\omega_b^2}{(\omega_k - k v_b)^2} = 0 \quad (61)$$

Here $\omega_k, \omega_{pe}, \omega_b, k \; and \; v_b$ are the resonant mode frequency, the background electron plasma frequency, the beam ion plasma density, the resonant wave number and the axial directed beam velocity respectively.

In this work, the main interest is in the effects of the two-stream instability, namely the non-linear fields the instability generates. There are two fields that can create radial defocusing of a charged particle beam: E_x, the radial electric field and B_y, the azimuthal magnetic field. In the case of two stream instability, large amplitude oscillations in E_z, the axial electric field, develop. Due to the transverse beam profile and its finite extent, the radial electric field strength has a transverse gradient, $\nabla_x |E_z|^2$. This gradient creates a ponderomotive force in the radial direction. Plasma electrons get radially displaced and the beam ions are pulled away by the resulting ambipolar field. The radial electric field generated this way is thus defocusing for the beam ions. The defocusing force due to the radial electric field, E_x is given by:

$$-eE_x = \frac{-e^2 \nabla_x |E_z|^2}{4 m_e \, \omega_k} = -\frac{1}{4} \, m_e \nabla_x (v_m^e)^2 \quad (62)$$

Here v_m^e is the axial electron velocity oscillation amplitude, ω_k is the resonant mode frequency and m_e is the electron mass. The field is a quadratic function of v_m^e, the electron velocity oscillation amplitude due to the instability. This is a perturbation, i.e a 1st order quantity. Hence the radial electric field is non-linear. Due to the negative sign of the gradient, it is defocusing for the beam ions.

The second field to look at is B_y, the azimuthal magnetic field. To understand the effects of two-stream instability on the azimuthal magnetic field, we first look at the current. The total electron current now has a component $<\delta n_e\ \delta v_m^e>$ which is the averaged non-linear current resulting from the perturbations in electron density and electron axial velocity due to the instability, in addition to the classical inductive electron return current[5,6]. With the inclusion of this time-averaged non-linear term, the total current, which is the sum of the beam current J_z^b and total electron current J_z^e becomes:

$$J_{tot} \sim J_z^b + J_z^e = \frac{J_z^b}{(1+r_b^2\omega_{pe}^2/c^2)} \left(1 - \frac{1}{2}\ \frac{n_p}{n_b}\ \left(\frac{v_m^e}{v_b}\right)^2\right) \tag{63}$$

The second term in the parenthesis comes from the average $<\delta n_e\ \delta v_m^e>$. Here n_p, n_b, r_b are plasma density, beam density and beam radius respectively. It is important to note that when $n_p \gg n_b$, which is typically the case for neutralization, the non-linear term will exceed one and the total current will be reversed. This is to say that due to the contribution of the non-linear current driven by instability the beam current will be overcompensated. In the absence of the two-stream instability the beam current will be reduced or neutralized by the electron current, depending on the skin depth, creating a classical pinching azimuthal magnetic field. But with the introduction of the non-linear current, the total current will be reversed and for $n_p \gg n_b$ will be substantial in magnitude. The end result is that B_y the azimuthal magnetic field will also become reversed and the magnetic force it applies on the beam will be defocusing:

$$B_y = \frac{2\pi n_b r_b \beta_b}{(1+r_b^2\omega_p^2/c^2)} \left(1 - \frac{1}{2}\ \frac{n_p}{n_b}\ \left(\frac{v_m^e}{v_b}\right)^2\right) \tag{64}$$

It is important to notice again the quadratic dependence of B_y on the electron velocity oscillation amplitude, v_m^e. In the presence of the instability we no longer have the classical force balance between azimuthal magnetic field and radial electric field. In this case both fields will introduce defocusing forces and the beam profile can become significantly disrupted. Fig. 15 is a beam density contour plot excerpt from the same simulation from which figure 14 in Sec.II was generated. Fig.14. shows the density profile at t = 16 ns, which is right after the beam has traveled to the center of the simulation domain. This is prior to the development of the instability. Figure 15 is the same beam at t = 40 ns, after nearly 6 m of propagation in plasma. This is after the full development and the saturation of the instability. The increase in radius and the distortion of the radial beam due to the non-linear defocusing forces is evident.

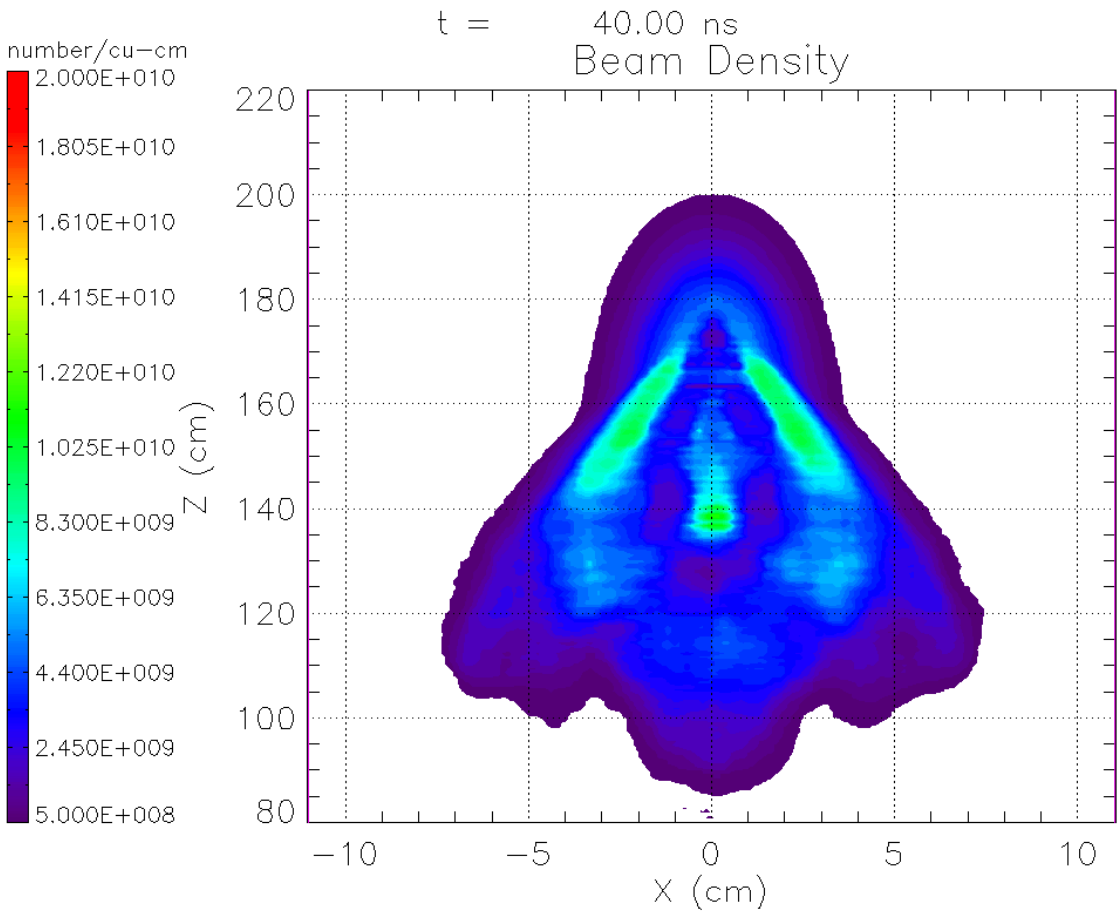

Fig.15. Density Profile after ~ 6 m of propagation for $n_p = 1.0 \times 10^{12}/cm^3$, $n_b = 2 \times 10^{10}/cm^3$, $r_b = 2\ cm$, $t_{pulse} = 12\ ns$, v_b = c/2

Looking at Eqns.2 and 4 we can arrive at the very important conclusion that the non-linear fields generated by the instability depend strongly on the axial electron velocity oscillation amplitude. Thus the saturation fields which will be responsible for defocusing of the beam, will depend on the saturation value of the electron axial velocity oscillation amplitude. Hence it is important to understand how the instability saturates, given the beam-plasma system parameters.

Depending on the parameters of the beam-plasma system, the two-stream instability can saturate either by trapping plasma electrons, or by trapping beam ions[5]**.** In the case of electron trapping saturation of the instability will occur when the electron oscillation amplitude reaches the phase velocity of the resonant mode $v_m^e \sim \omega / k_z$, which will be comparable to v_b the beam velocity. In the case of ion trapping, beam ions will be oscillating with axial velocity $v_m^b \sim v_b - \omega_k / k_z \sim (\gamma / k_z) \sim (\gamma / \omega_{pe}) v_b$ at saturation, where ω_{pe}, ω_b are the plasma frequencies of the background plasma electrons and the beam ions respectively. γ is the growth rate of the resonant mode given by $\gamma \sim \omega_p (\omega_b / \omega_{pe})^{2/3}$. As the electrons and beam ions both experience the same electric fields, both species attain the same momentum in a given amount of time. This momentum balance gives: $m_e \omega_k v_m^e = m_b (\omega_k - k_z v_b) v_m^b$. Solving for v_m^e we get $v_m^e \sim \left(\frac{m_b}{m_e}\right)\left(\frac{\gamma}{\omega_{pe}}\right) v_m^b$. Depending on which species reach their respective saturation level oscillation amplitude first, the instability will saturate by the particle trapping of either beam ions or the plasma electrons. Under this picture of saturation, the saturation value of electron velocity oscillation amplitude normalized by beam velocity will be given by:

$$\left(\frac{v_m^e}{v_b}\right) = \sim \min[\alpha,\ 1],\ \alpha = \left(\frac{n_b}{n_p}\right)^{\frac{2}{3}} \left(\frac{m_b}{m_e}\right)^{1/3} \tag{65}$$

The first limit is the case when the instability saturates by ion trapping, and the second limit is the case when the instability saturates by electron trapping.

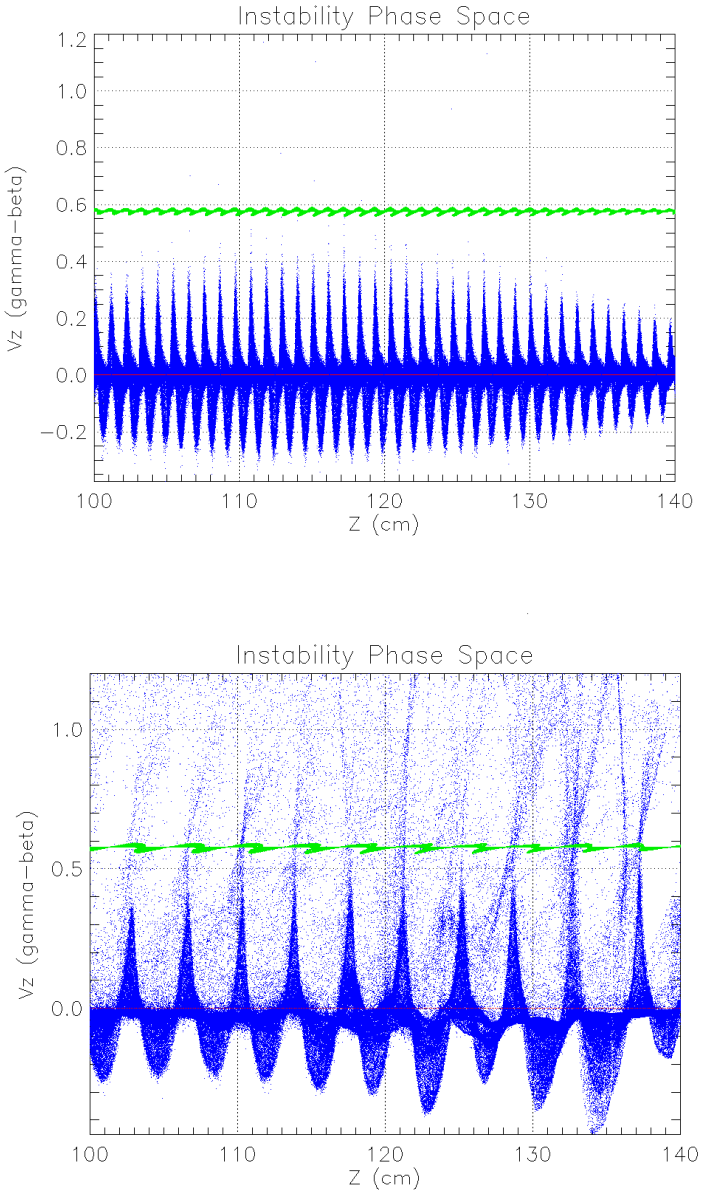

Blue: Plasma Electrons, Red: Plasma Ions, Green: Beam ions. Phase space at saturation V_z vs z.

Fig.16. Identification of Saturation Mechanism using Phase Space diagnostics. Top: $n_p = 2.422 \times 10^{12}/cm^3$ ion trapping regime, Bottom: $n_p = 1.6481 \times 10^{11}\ /cm^3$ electron trapping regime. $n_b = 2\ \times 10^{10}\ /cm^3$, $r_b = 2\ cm$, $t_{pulse} = 12\ ns$, v_b = c/2

The saturation mechanism and consequently the electron velocity amplitude is determined by a parameter, we denote by α, which is a function of the beam-plasma density and beam-electron mass ratio. Thus for a given beam density and beam ion mass, having relatively less plasma density will cause the instability to saturate by electron trapping and the electron oscillation velocity amplitude at saturation will be of order ~v_b. In the dense background plasma limit, the instability will saturate by ion trapping of the beam ions and the electron velocity oscillation amplitude normalized by beam velocity will be given by the scaling parameter α itself. This understanding of electron velocity amplitude dependence on beam parameters can be tested using PIC code LSP. Fig.16. top shows a high background density $\alpha = 0.5$ simulation phase space. Notice the electron oscillation amplitude is roughly half of beam velocity as expected. Fig.16. bottom shows $\alpha = 3$ beam plasma system in the lower background density limit. Since the scaling parameter is greater than 1, electron velocity oscillation amplitude is comparable to v_b. A significant population of plasma electrons wave-trapped by the instability is observed in this case, which results in the saturation of the instability.

IV-Scaling of The Self-Fields and the Defocusing Force:

In order to understand the scaling of defocusing forces with respect to changes in system parameters, we need to change the scaling parameter which will change electron oscillation velocity amplitude and consequently the non-linear fields. We do this by changing the background density in the range $n_p \in \left[5 \times 10^{12}, 8 \times 10^{10}\right]/cm^3$ which corresponds to $\alpha \in [0.3,5]$ while keeping other system parameters constant. As described in detail in Sec.II. we simulate a proton beam with a Gaussian radial profile with radius $r_b = 2\ cm$, peak density $n_b = 2 \times 10^{10}\ /cm^3$, pulse duration $t_{pulse} = 12\ ns$ and axial directed beam velocity $v_b = c/2$,

c is the speed of light in vacuum. Fig.17. shows the scaling of electron velocity oscillation amplitude and radial electric field when the scaling parameter is changed by altering the background plasma density.

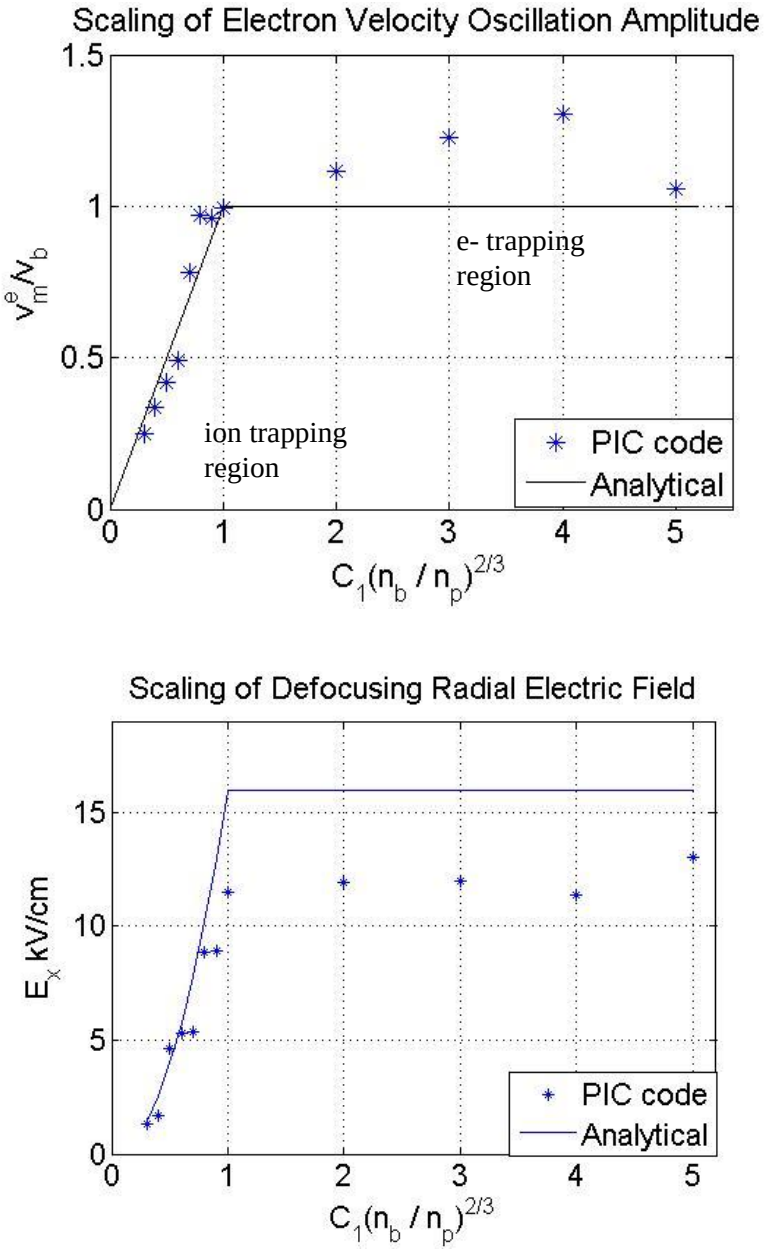

Fig.17. Top: Scaling of rms electron velocity oscillation amplitude measured on axis. The analytic estimate is given by Eqn.65. Bottom: Scaling of radial defocusing electric field from LSP simulation, measured at $r_b \sim 1\ cm$ which corresponds to the maximum field

strength. $\boldsymbol{\alpha = C_1(n_b/n_p)^{2/3}}$, $\boldsymbol{C_1 = \left(\frac{m_b}{m_e}\right)^{1/3} \sim 12.24}$ for H+ beam. The Analytic estimate is given by Eqn.62.

Fig.17. Top is the confirmation of electron velocity oscillation amplitude (at saturation) scaling given by Eqn.65. Fig.17. bottom shows the scaling of radial electric field. Notice here that in the low density electron trapped limit ($\boldsymbol{\alpha = C_1(n_b/n_p)^{2/3}} > 1$) radial electric field saturates at a maximum value. This is expected since in this region $E_x \sim \nabla_x \, (v_m^e)^2 \sim \nabla_x \, v_b^2$, which is constant irrespective of the scaling parameter and the background density. Therefore in the electron trapping regime the radial electric field is insensitive to changes in background plasma density.

For the investigation of azimuthal magnetic field, we compare the results of the PIC code LSP with the analytical estimation (Eqn.64) as well as the numerical solution of Ampere's Law for the vector potential with the inclusion of the non-linear electron current term introduced by the instability, which we solve for the same set of parameters used in the simulations. For the numerical solution of the ODE, we used the same Gaussian radial beam profile for the beam density and the step size as with the simulations $\Delta x = 0.1$ cm.

$$\nabla^2 A_z = \frac{-4\pi}{c} J_b - \left(\frac{\omega_{pe}}{c}\right)^2 A_z - \frac{4\pi e}{c} \frac{1}{2} \frac{n_p}{n_b} \left(\frac{v_m^e}{v_b}\right)^2 J_b \tag{66}$$

$$J_b = e n_b v_b, B_y = -\frac{\partial A_z}{\partial x} \tag{67}$$

Fig.18. shows the comparison of the analytical solution and the numerical solution of the modified Ampere's law including the instability driven time-averaged non-linear electron current with the results from the particle-in-cell code for different n_b / n_p. The data points from the numerical solutions and the PIC simulations contain the maximum value of the azimuthal

magnetic field strength, which are located at around x = 1 cm with small variation. The analytical solution is a rough estimate with no explicit positional dependence except through beam density profile, for which we have used the peak value. The curves from the PIC code, the analytical solution and the numerical solution for Ampere's law are in good agreement, and they each show the same trend. In the transition region, where $\alpha \sim 1$ and the mode saturation mechanism changes from ion trapping to electron trapping or vice versa, the azimuthal magnetic field strength is maximized. This is intuitive since azimuthal magnetic field depends on the total current, where the non-linear electron current dominates. In the electron trapping regime the electron perturbed velocity is maximum with amplitude $\sim v_b$, however the background plasma density is low. In the ion trapping regime the background plasma density is high, but the electron velocity oscillation amplitude is low $\sim \alpha$. Thus transition region is an optimum regime in the parameter space where the electron velocity is close to is maximum, and the background density is still large, thus yielding a large non-linear current, and consequently a large azimuthal magnetic field. This azimuthal magnetic field is defocusing. It is also important to point out that the radial electric field reaches its maximum in the transition region and then remains constant in the electron trapping regime. Thus the total defocusing force will be maximum at this region in parameter space. Therefore the transition region is a regime to avoid for the design of experimental beam-plasma devices where the two-stream instability is expected to develop.

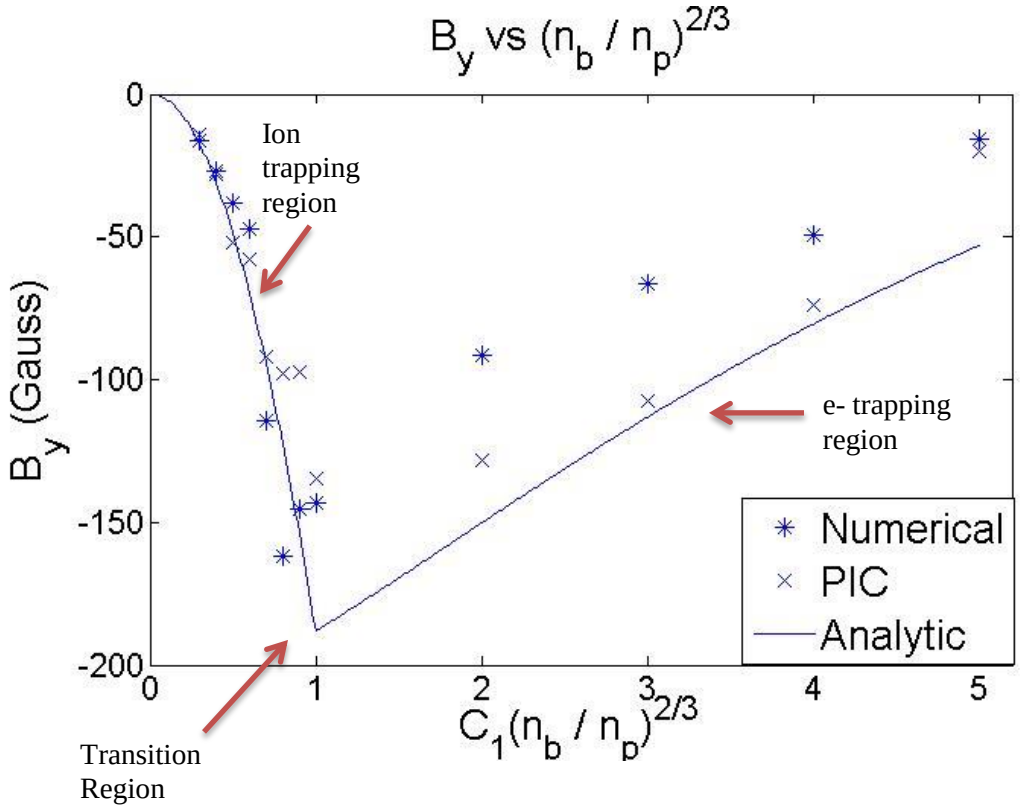

Fig.18. Confirmation of azimuthal magnetic field scaling, which is reversed and defocusing. $\boldsymbol{\alpha = C_1(n_b/n_p)^{2/3}}$ ***** $\boldsymbol{C_1 = \left(\frac{m_b}{m_e}\right)^{1/3} \sim 12.24}$ **for H+ beam. Note that the maximum magnetic field strength is attained at the transition region.**

Having described the behavior or the radial electric field E_x and the azimuthal magnetic field B_y as the background density is changed, we can now look at how the Lorentz Force that will be exerted on a beam ion scales.

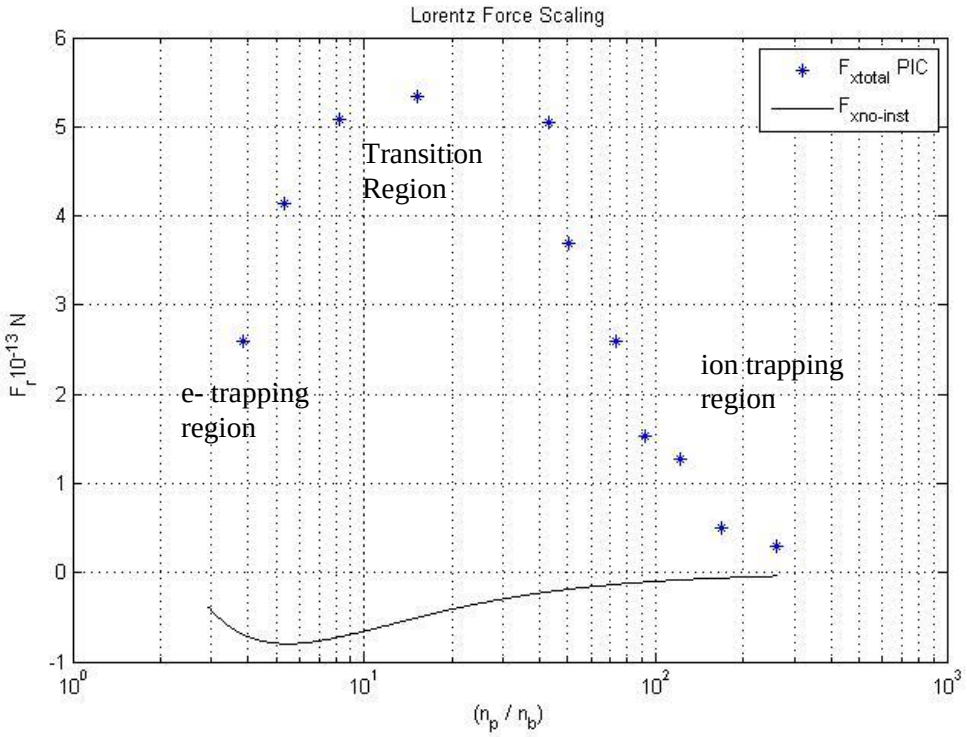

Fig.19. Lorentz Force (radial) F_x vs $n_p/\ n_b$ log-scale. The points are LSP PIC code results where the instability is present, the continuous curve is the analytical estimate of the total defocusing force for the case of no instability.

Looking at Fig.19. we can compare the Lorentz force curves in the presence and the absence of the instability. The no-instability case can correspond to a system where $1/\gamma \gg L/v_b$. Here γ is the growth rate of the instability and L is the system size in the axial direction. In this case the instability does not have enough time to develop to saturation as it transits the finite size system.

The first thing to note when comparing the classical and non-linear forces is the difference in the sign. The classical case where the non-linear fields due to the instability is ignored predicts a pinching force [43,44], whereas in the presence of the instability the transverse total force will in fact be defocusing. The second thing to note is the difference in the magnitude of the forces. As can be seen from Fig.19. for the same set of parameters the non-linear force can be significantly

larger than the classical estimation where the non-linear effects are not taken into consideration. The scaling of the non-linear forces with back ground density reveal a potential device design problem. For a beam-plasma device with background plasma density larger than the beam density by an order of magnitude for the case of a proton beam, it can be seen that the instability will saturate by electron trapping. To improve the neutralization performance, it is intuitive to introduce more background plasma, i.e. increase n_p, after all the purpose of the plasma is to reduce the space charge and the total current and thus reduce the self-fields. However in the presence of the instability increasing the plasma density for a device operating in the electron trapping regime, will put the system closer to the transition region ($n_p / n_b \sim 40$ which corresponds to $\alpha \sim 1$ for a proton beam) in the parameter space where the maximum defocusing force is attained. Thus increasing plasma density in the electron trapping regime will actually increase the total defocusing force, and deteriorate the neutralization performance of the beam plasma device. This counter-intuitive conclusion can be of crucial importance for device design.

V-Conclusion:

In this work, we investigated the effects of beam-driven two-stream instability on the transverse defocusing of an ion beam propagating in background plasma. We showed that the non-linear fields generated by the instability can result in significant defocusing of the beam and that the saturation values of the fields depend strongly on the saturation amplitude of axial electron velocity oscillations. By identifying a scaling parameter which is a function of beam plasma density, and beam ion and electron mass we studied the scaling behavior of the non-linear fields, when the scaling parameter is changed by sweeping the background density. Using PIC code LSP we showed that in the low background density limit, where the instability

saturates by electron trapping, the radial electric field will become independent of the background density. The azimuthal magnetic field and the total defocusing force will be maximized for the transition region between the high and low background density limits and we identified this region as a least favorable design space for a beam-plasma device in the presence of the two-stream instability. We also showed that in the electron trapping regime (low background density limit) increasing the plasma density will counter-intuitively increase the total defocusing force and reduce device performance in terms of the ballistic propagation and field neutralization.

Part 2 : Detection of two-stream instability in an ion beam plasma system through beamlet extraction.

I-Introduction

In Part 2 of this chapter we again study an ion beam pulse propagating in a background plasma, which is subject to two-stream instability between the beam ions and plasma electrons, using PIC code LSP. The non-linear effects of the instability can be much more pronounced in thin beams, as the density gradient is increased. Therefore we propose that a beamlet extracted from even a slow heavy-ion beam can be used as a diagnostic tool to identify the presence of the two-stream instability and quantify for its effects. We test this idea by simulating a cold, low-emittance thin beamlet extracted from a $v_b \sim c/30$ Li+ beam parameters similar to the proposed NDCX-II and show that the presence of the instability can be investigated tracking the spot size of the extracted beamlet.

In the case of heavy ion beams, the displacements and the distortion created by the two-stream mode can be small and its detection difficult. In this paper we propose a diagnostic method, whereby a beamlet is extracted from the original beam and propagated an equal distance with the original beam. Tracking the spot size of the extracted beamlet will reveal whether or not the instability is present. We demonstrate this idea using a fully-kinetic multidimensional PIC code in a 2-D setting using a moving-frame electrostatic solver for 3 different cases.

II- Simulation of an Ion Beam with NDCX-II Parameters Propagating in Background Plasma:

In the case of the proposed NDCX-II experiment there is a Li+ beam with axial directed velocity $v_b = c/30$, $n_b = 2 \times 10^9\ /cm^3$, r = 2 cm propagating in background carbon plasma with density $n_p = 0.55 \times 10^{11}\ /cm^3$. However the relatively small axial velocity implies that the non-linear fields will be small in magnitude, and Li ions will be harder to displace due to their larger inertia. Therefore macroscopic changes to the beam profile will not occur and the presence of the instability will much harder to detect. To test this idea, we simulated an NDCX-II like beam with a radial flat top profile and an axial Gaussian pulse with $\Delta t = 20\ ns$ with PIC code LSP using a moving frame algorithm where $v_{frame} = v_b$. Fig.20. shows the phase space of the beam plasma system at saturation.

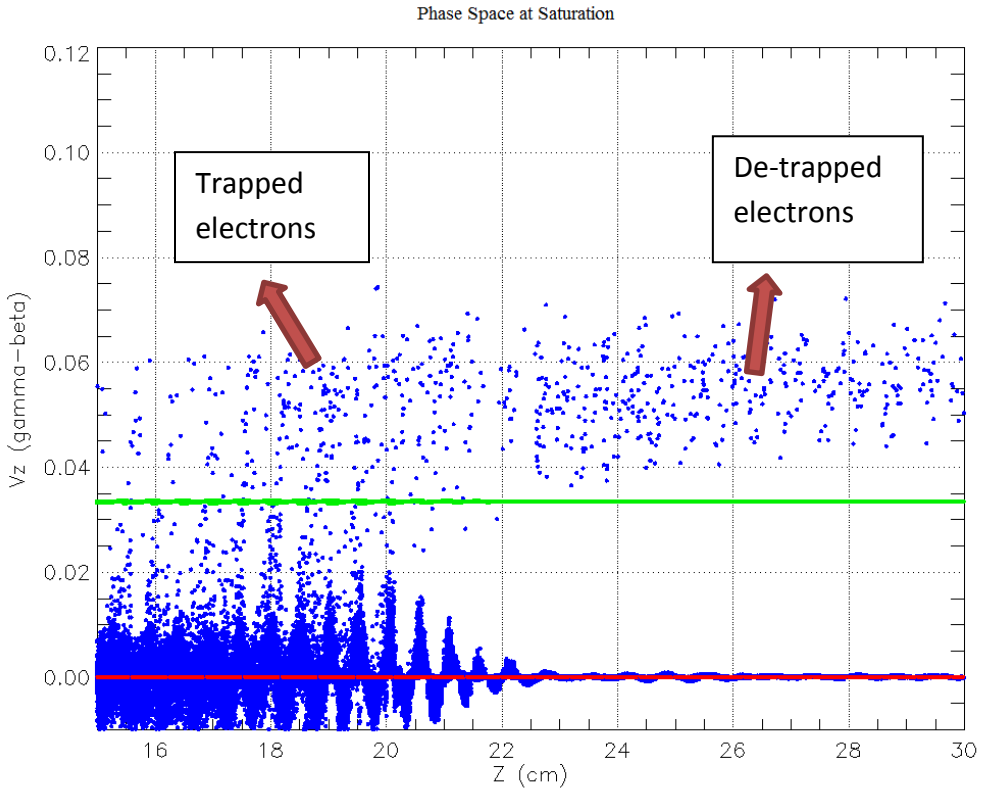

Fig.20. Beam-Plasma system phase space at saturation of the two-stream instability t = 240 ns. Blue- Plasma electrons, Red-Plasma Ions, Green – Beam Ions.

Fig.20. clearly shows the modulation of electron velocity due to the instability. Note here that this instability has saturated by the wave-trapping of electrons and the oscillation amplitude of electron velocity at saturation is consequently comparable to the beam velocity which is expected for the given beam-ion mass, plasma and beam densities [41]. There is also a population of electrons that have escaped trapping due to the axial gradient in $|E_z|$. They appear as a precursor e- current preceding the beam. To study any possible defocusing effects, we next look at the density contours and radial cross-sections of the beam at different times.

a-

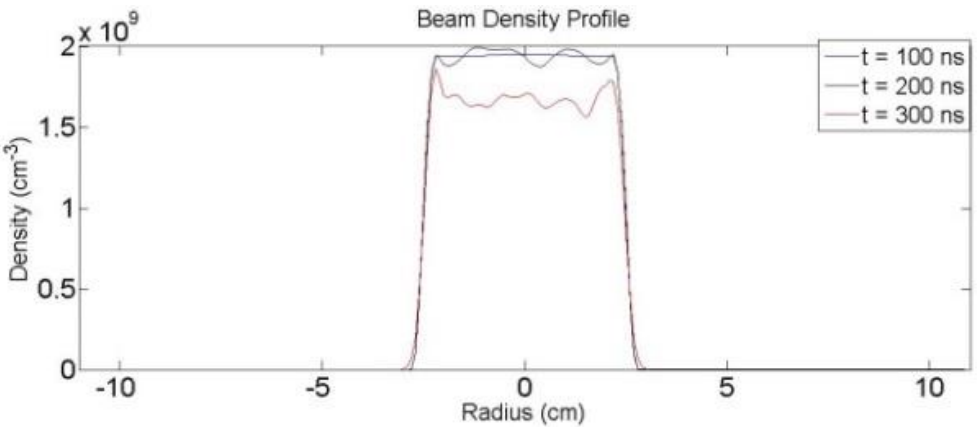
Beam Density Profile
x 10^9
Density (cm^-3)
Radius (cm)
t = 100 ns
t = 200 ns
t = 300 ns

b-

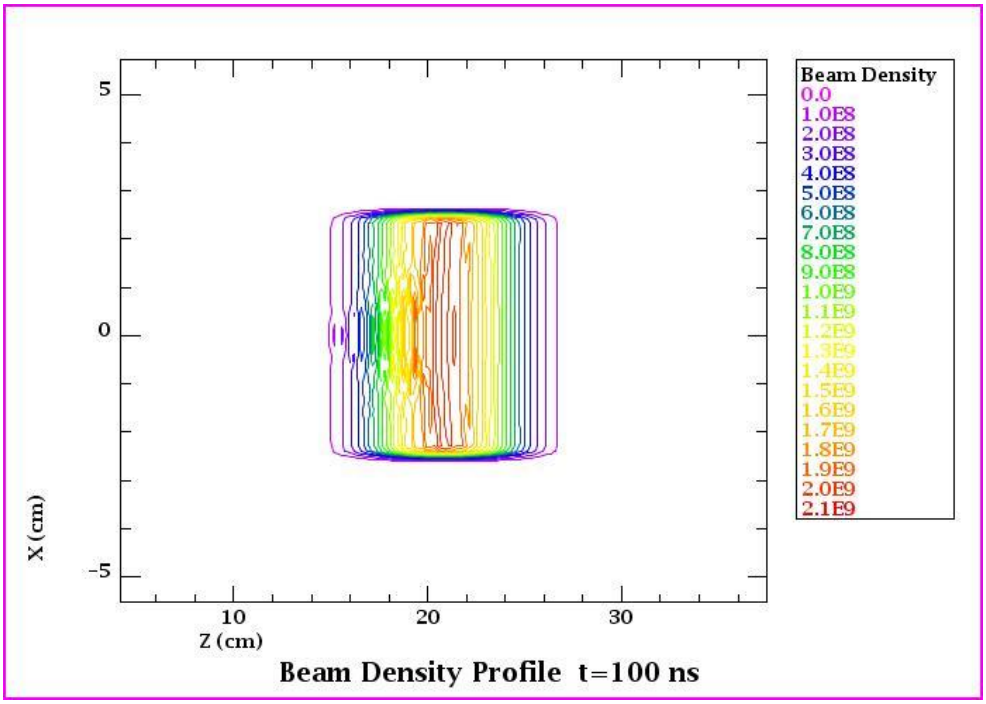
Beam Density
0.0
1.0E8
2.0E8
3.0E8
4.0E8
5.0E8
6.0E8
7.0E8
8.0E8
9.0E8
1.0E9
1.1E9
1.2E9
1.3E9
1.4E9
1.5E9
1.6E9
1.7E9
1.8E9
1.9E9
2.0E9
2.1E9
X (cm)
Z (cm)
Beam Density Profile t=100 ns

c-

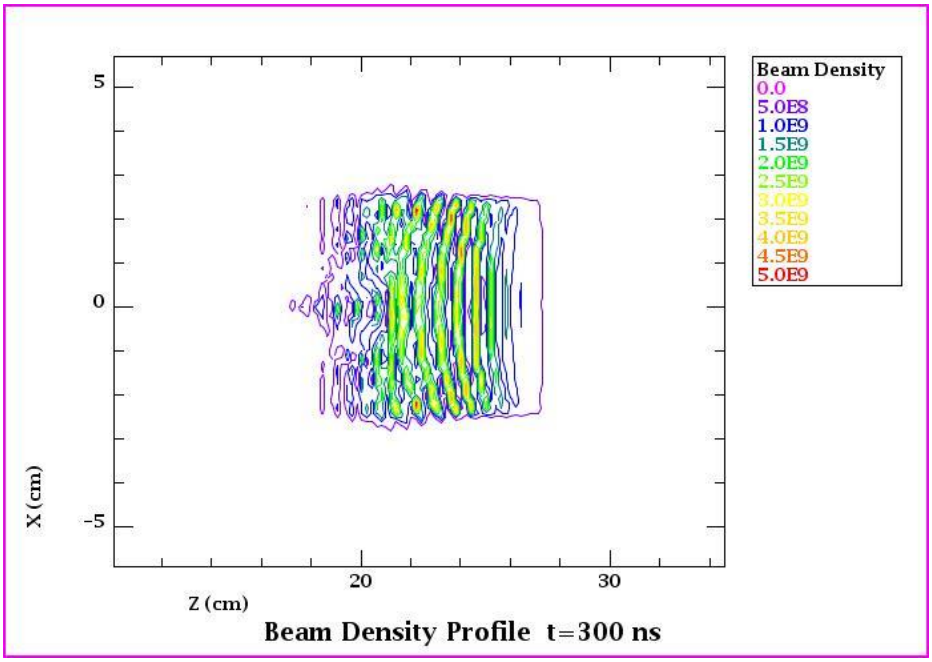

Fig.21. a: Radial Beam density Profiles at t= 100, 200 and 300 ns, b: Beam Density Contour at t = 100 ns (1 m of propagation), c: Beam Density Contour at t = 300 ns (3 m of propagation).

Looking at Fig.21. right we can see that even though the instability develops as can be observed by the modulation in density, the non-linear defocusing forces are not strong enough to significantly distort the beam profile and increase the beam spot size. Note at t= 100 ns which corresponds to the initial linear stage of the instability $r_b \sim 2.65\, cm$. The instability saturates around t = 240 ns. At t = 300 ns $r_b \sim 2.97\, cm$, yielding $\Delta r_b / r_0 \sim 0.12$ In an experimental perspective this shows that the detection of the two-stream instability in the ballistic propagation stage of the device will be diagnostically difficult.

III- Simulation of an Extracted Ion Beamlet

Although the detection of the instability through defocusing effects will be difficult for an ion beam with radius $r_b \geq \delta_{skin}$,where δ_{skin} denotes skin depth and is roughly 2 cm for NDCX-II parameters, for a beamlet extracted from the beam the change in radius normalized by initial radius can be much more dramatic and thus easier to detect. In the case of the beamlet since $r_{beamlet} \ll \delta_{skin}$ the total magnetic field, which is the sum of the classical pinching field and the non-linear defocusing field will be smaller. However the radial defocusing force due to the radial electric field which under NDCX-II parameters is much larger than the magnetic field will be enhanced if the beam profile is such that a reduction in radius will imply a larger gradient or stay the same if the reduction in radius does not alter the density gradient, since $F_x = -\frac{1}{4} m_e \nabla_x (v_m^e)^2$ and the gradient of the perturbation in axial velocity and the fields is the gradient of beam density as the mode is electrostatic . Hence the presence of two-stream instability can be easily diagnosed by extracting a beamlet of smaller radius and propagating it through the background plasma, for the same duration as the original beam. A beamlet of radius r_b =0.1 cm with NDCX-II parameters for profile shape, beam and background plasma density was simulated using PIC code LSP. Fig.22. shows the evolution of beam density profile in the beam frame as it propagates through background plasma.

a-

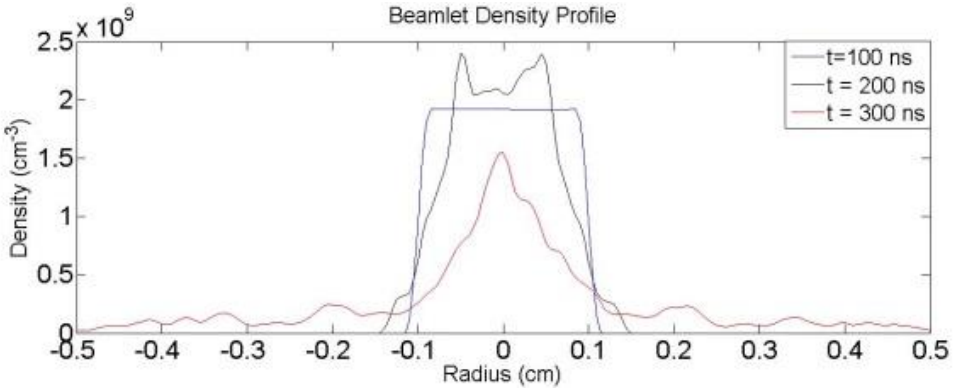

b-

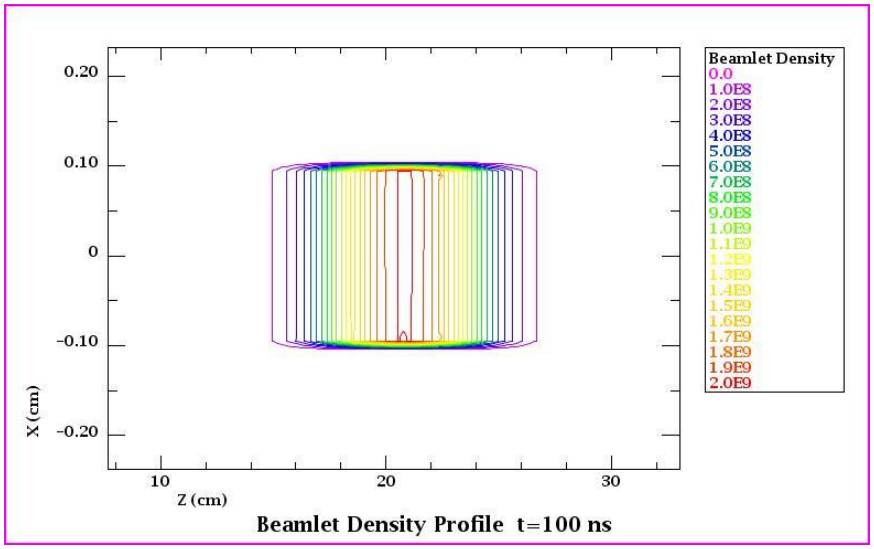

c-

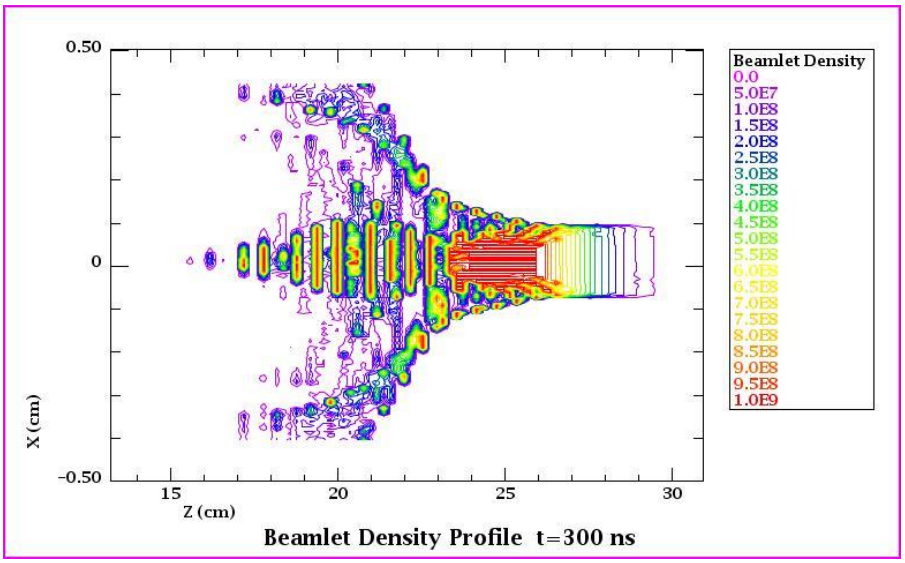

Fig.22. a: Radial Beamlet density Profiles at t= 100, 200 and 300 ns, b: Beamlet Density Contour at t = 100 ns (1 m of propagation), c: Beam Density Contour at t = 300 ns (3 m of propagation).

The results of the beamlet $r_b = 0.1$ cm simulation indicate that unlike the original beam, the extracted beamlet becomes significantly distorted and defocused due to the increase in non-linear defocusing forces created by the beam driven two-stream instability. In fact $\frac{\Delta r_b}{r_{b0}} > 5$ for t= 300 ns. Hence tracking the spot size of an extracted beamlet can be a useful tool to detect the presence of two-stream instability.

Next we need to demonstrate that the subsequent spreading of the beamlet is due to the non-linear defocusing forces generated by the two-stream instability and not because of poor neutralization or beam emittance. Note that all simulations performed for this work have cold beam and plasma species. To illustrate this we perform a simulation, where the ion beamlet will be charge and current neutralized by an electron beam of same density, profile and velocity. In this case the instability will not develop as the velocity distribution is no longer a sum of two delta functions at two different velocities ($v = v_{beam}, v = 0$) and thus there is no streaming of particles. Fig.23. below shows the evolution of the ion beam density contours and radial profile when it is neutralized by an electron beam.

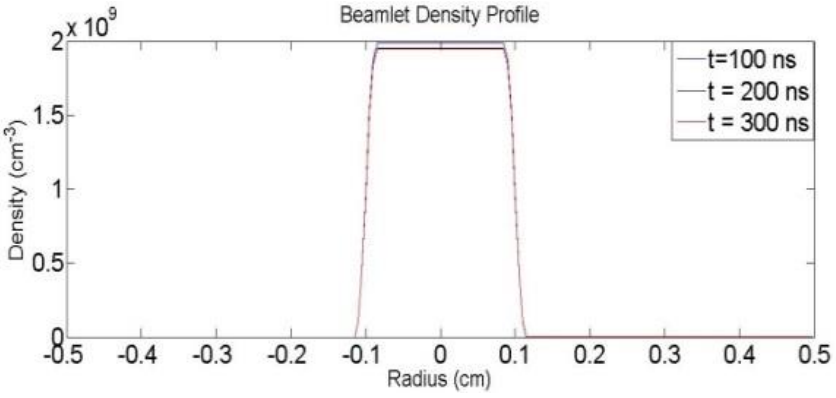

a-

b-

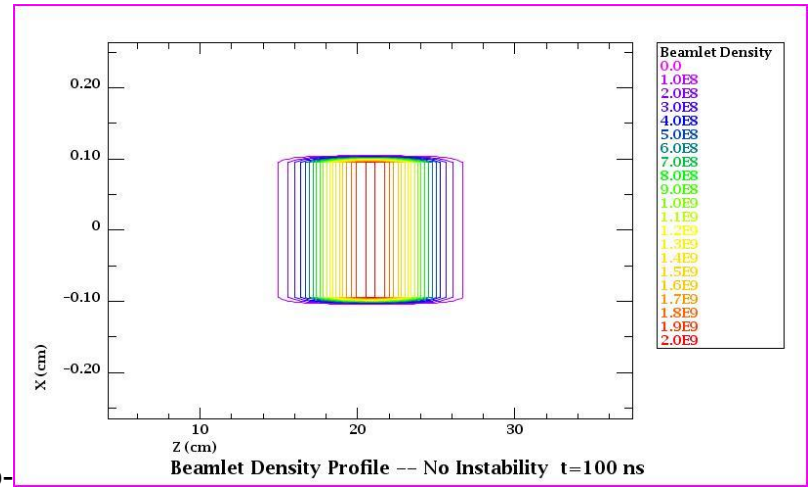

c-

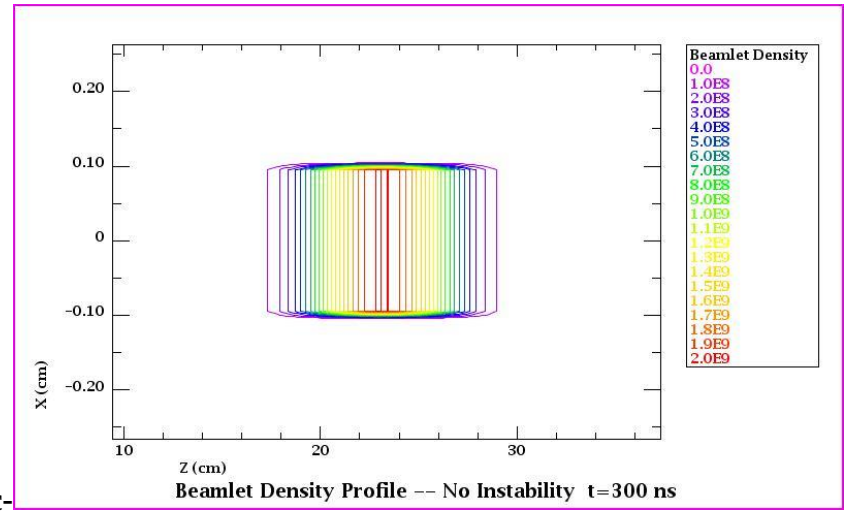

Fig.23. Top: Radial Beam density Profiles at t= 100, 200 and 300 ns, Middle Beam Density Contour at t = 100 ns (1 m of propagation), Bottom: Beam Density Contour at t = 300 ns (3 m of propagation).

The density contour plots of Fig.23. demonstrate that there is no modulation of beam density, which shows that as expected the two-stream instability is entirely absent. Moreover both the contour plots and the radial profile show almost no increase in spot size, which is significant as it validates that the defocusing of the ion beamlet in a stationary background

plasma is entirely due to the non-linear time-averaged forces generated by the two-stream instability.

IV- Conclusion:

In Part 2 of Chapter 4 we have shown that beam-driven two-stream instability can lead to the creation of non-linear defocusing fields which can significantly distort fast, light-ion (i.e. proton) beams. In the case of slower, heavy ion beams the presence of the instability might become much harder to detect. We proposed that a diagnostic can be used to extract a beamlet from the original beam. In the case of a beamlet, the increase in spot size relative to the initial spot size will be much more significant and easier to detect. This will provide an experimental tool to quantify for the presence of the two-stream instability in the beam-plasma system. The results of this section was presented and to be further submitted for publication [45-47].

Chapter 5:

Simulation of Electron-beam Driven Two-Stream Instability

5.1 1-D Fully Kinetic Simulation of an Electron Beam Propagating in Background Plasma performed in EDIPIC and LSP

I-Introduction

The interaction of electron beams with plasmas is of considerable importance particularly for hybrid DC/RF coupled plasma sources used in plasma processing [37]. An electron beam is formed by emission from one surface, is accelerated through a dc bias electric field and enters the bulk plasma. Emitted electrons excite electron plasma (Langmuir) waves through the two-stream instability. Due to the high localized plasmon pressure, ion acoustic waves are excited parametrically. The plasma waves saturate by non-linear wave trapping. Eventually coupling between electron plasma waves and ion acoustic waves deteriorates the Langmuir waves, which leads to a bursting behavior. The two-stream instability and the consequent ion fluctuations are studied over a wide range of system parameters using the particle-in-cell codes EDIPIC [38,39]

and LSP. The influenceof these instabilities on collisionless electron heating are presented for a hybrid RF-DC plasma source. The results of these simulations were reported [40,41].

II- Setup of Simulations

Table 4 and 5 below contain the parameters used in EDIPIC and LSP simulations for the electron beam- background plasma system.

- System length 3 cm
- Ion mass: 10, 20, 40, 60, and 80 amu
- All ions are specularly reflected from the walls
- Electrons with energy below 400 eV are specularly reflected from the walls
- Start with rectangular density profile
- Plasma density 1e16 m^{-3}
- No collisions
- Initial electron temperature 2 eV, ion temperature 0.1 eV
- Constant electron emission 1.25e20 m^{-2} s^{-1} from cathode at x=3 cm
- Voltage 800 V
- Grid has 1614 cells of size 18.585 μm
- Time step 0.739 ps
- 2000 particles of each species per cell
- Duration of simulation 10 μs

Table 4 EDIPIC Simulation Parameters.

- Argon plasma $n_p = 10^{10}\ /cm^3$
- Plasma frequency $\omega_p \sim 5.6 \times 10^9\ rads/s$
- e-beam $n_b = 10^8\ /cm^3$
- $KE_z = 800\ eV$
- $\beta \sim 0.05\ \ \gamma \sim 1$
- All species cold, 0 eV
- L ~ 6 cm, absorbing walls, no collisions
- 0.01 cm grid size
- Time step 0.033 ns
- 200 pic for plasma particles, 5 for beam
- Flat initial density profiles
- Similar parameters overall as the initial EDIPIC runs

Table 5 Parameters of LSP Simulations

III- Excitation, Saturation and Dissipation of the Two Stream Instability.

The streaming of the beam electrons against the stationary back ground plasma kinetically excite the Two-Stream Instability between the beam and plasma electrons. (The mode between the beam electrons and plasma ions can be shown to be always damped in the case). The frequency of the instability is determined by the simple kinetic relation $\omega \sim kv_b \sim \omega_{pe}$ where

ω_{pe} is the electron plasma frequency, v_b is the axial beam velocity and k is the wave number. As we will discuss shortly with reflecting boundary conditions at the anode end, the instability can be excited depending on the system size and the background density. When excited, the instability exhibits the following time evolution shown in Fig.24. below.

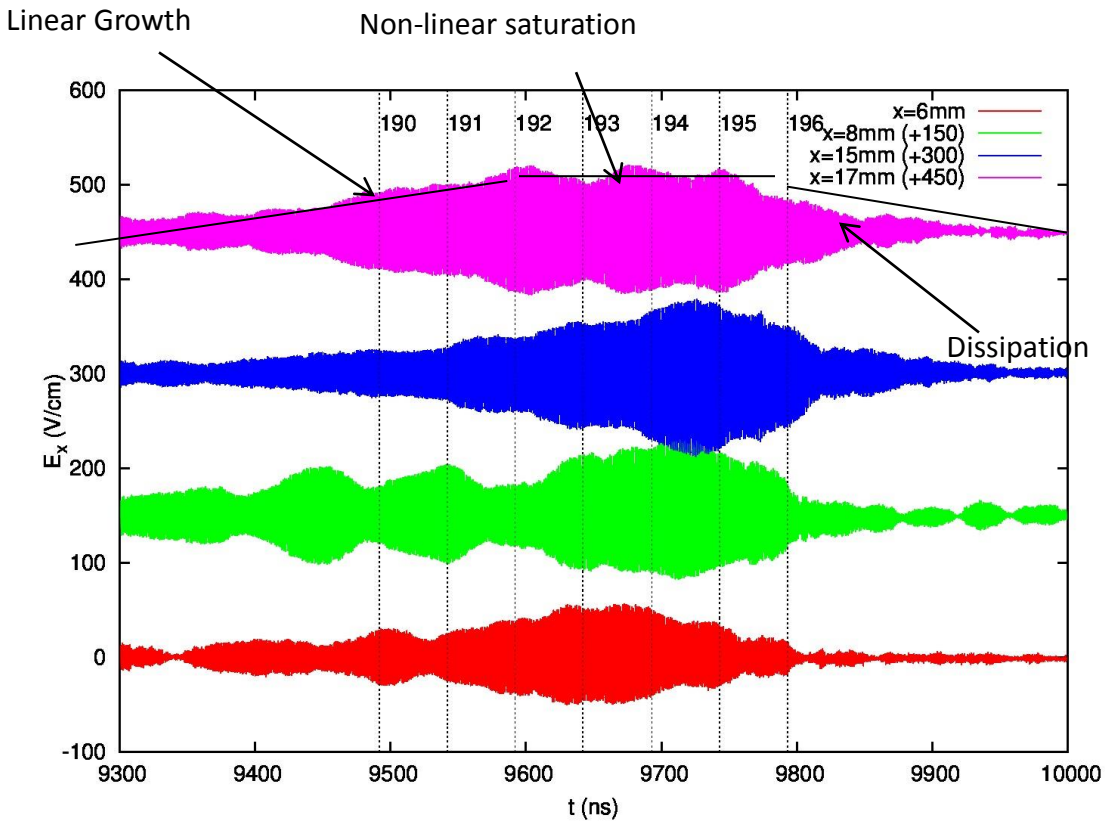

Fig.24 Axial Electric Field vs Time from different probe locations showing the linear growth, saturation and dissipation of the instability using EDIPIC.

The excitation of the two-stream instability depends whether or not the resonant wave number can be contained in the physical system or $k > 2/L_{sys}$ where L_{sys} is the system size. Thus when the system size is reduced below half the resonant wavelength, the instability will no longer develop. The same effect can be produced by reducing the background plasma density while

keeping beam velocity constant. Reducing the plasma density will reduce the electron plasma frequency and thus the resonant mode number. When the half wavelength of the resonant mode exceeds the system size due to the periodic boundary conditions the resonant mode will no longer be contained in the system and the instability will not develop. This effect using variation of the system size is demonstrated in Fig.5.2. It is also important to note that the occurrence of the instability is intermittent. Most of the EDIPIC simulations were run up to 10μs displaying periods of instability followed by quiet states.

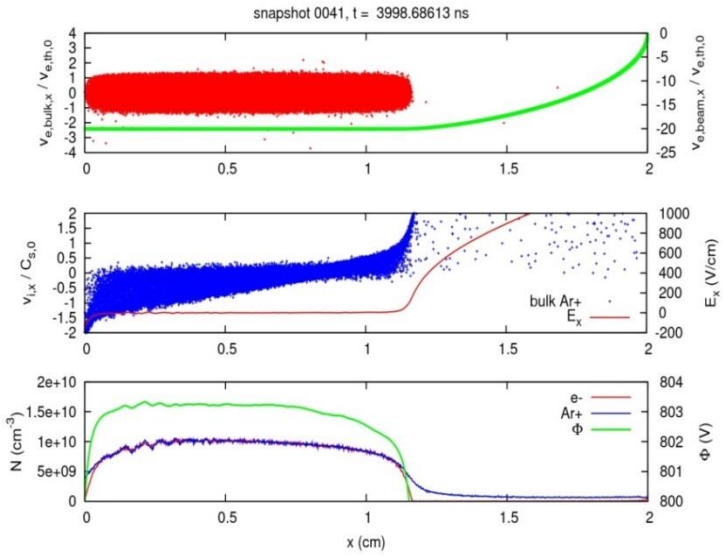

No Instability Short System Size using EDIPIC

Fig.25.a Top: e- phase space, red plasma e-, green beam e-.Middle: Ion Phase space and Ex. Blue ion velocities, red Ex Bottom: Density and Potential: red plasma e-, blue ions, green potential.For an Argon Plasma. System size is 2 cm. Note there are no oscillations in the phase space, the potential and the density. The instability is absent.

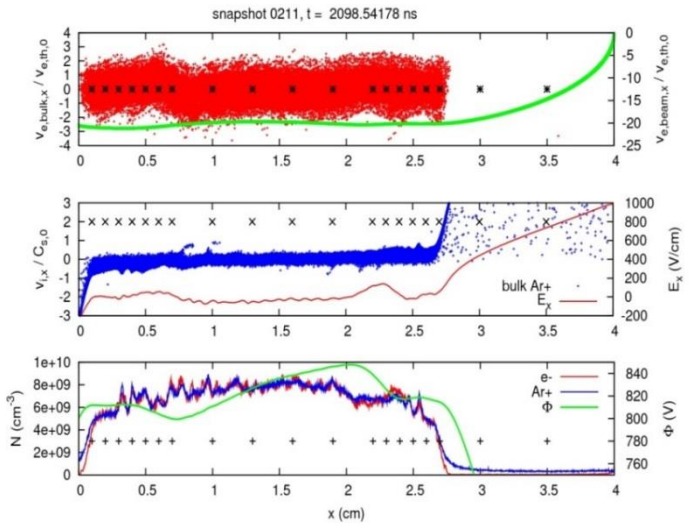

Instability Longer System Size using EDIPIC

Fig.25.b Top: e- phase space, red plasma e-, green beam e-.Middle: Ion Phase space and Ex. Blue ion velocities, red Ex Bottom: Density and Potential: red plasma e-, blue ions, green potential.For an Argon Plasma. System size is 4 cm. Note there are oscillations in the phase space, the potential and the density. The electrostatic two-stream instability is present.

A closer inspection of the phase space reveals that the instability saturates by the wave-particle trapping of beam electrons, a fact that is demonstrated both in EDIPIC and LSP simulations. Fig.26. is the phase space of the LSP simulation taken during the linear growth and saturation stage of the instability demonstrating particle trapping.

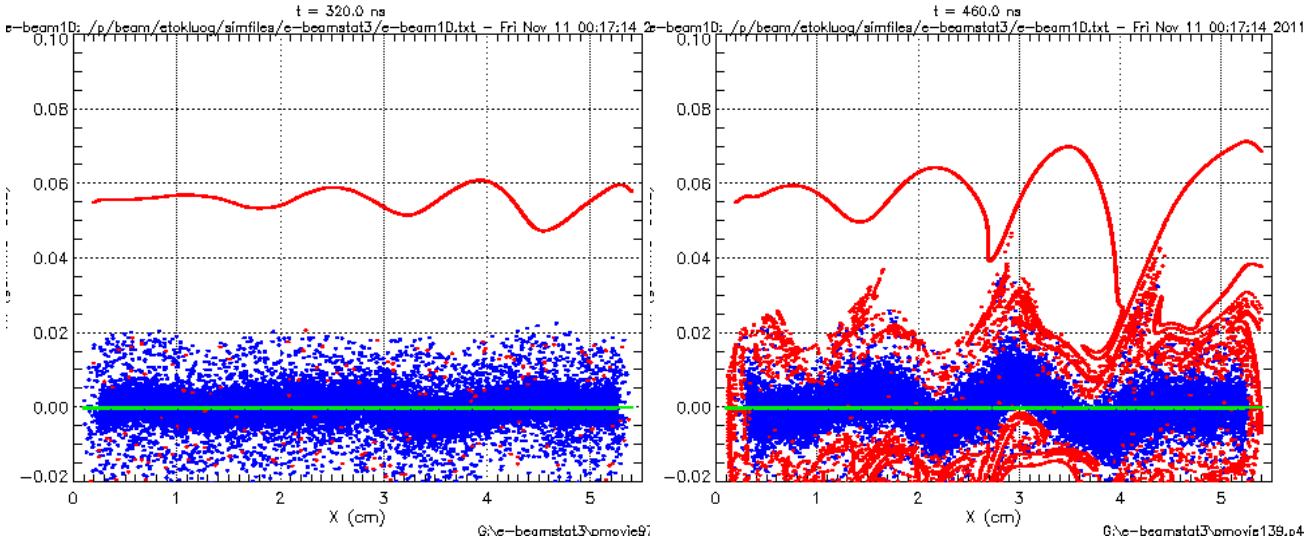

Fig.26. Phase Space Evolution: Left: t=320 ns Linear Stage, Right t= 460 ns non-linear stage showing particle-trapping of electrons (blue: plasma e-, red beam e-, green plasma ions). Trapping of electrons seems to be the primary mechanism of non-linear saturation.

An analysis of the distribution function for the plasma electrons gives important insight for the dissipation mechanism of the instability. The 1^{st} order axial Electric field created by the electrostatic instability creates axial collisionless scattering of the plasma electrons. This results in the increase of the axial electron temperature and the distribution function widens, to an extent that the tails of the distribution reach the phase velocity of the instability, which is v_b the axial

directed beam velocity. This results in landau damping and the instability is dissipated. Fig.27 shows the widening of the distribution function for EDIPIC simulations of different background Ion Species.

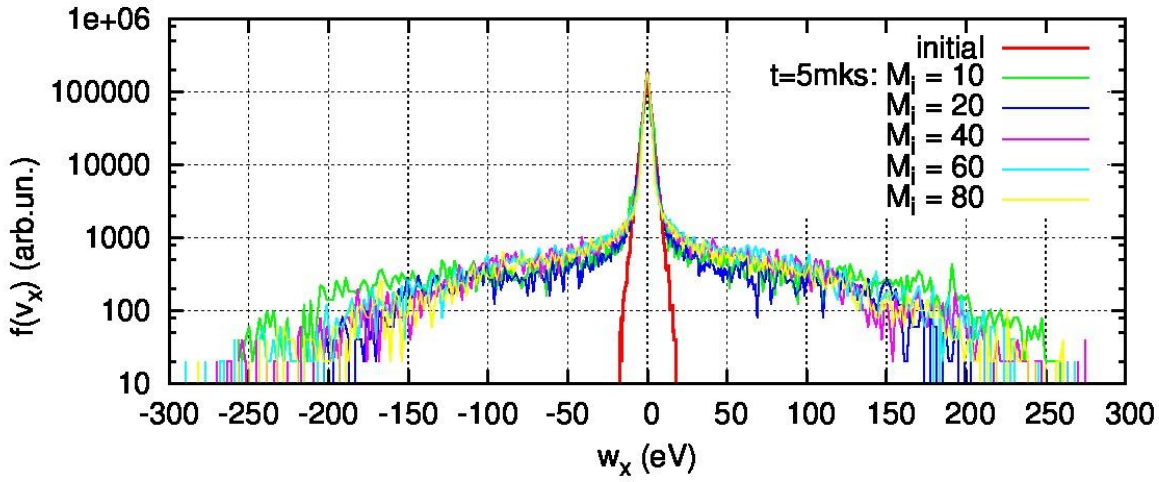

Fig.27. Collisionless heating of plasma electrons due to high E-fields for different ion mass. Final f for plasma e- is given at t = 5 μs.

IV-Ion Dynamics, Cavity Formation and Ion Acoustic Waves

An interesting result of the development of the Two-Stream Instability is non-linear ion dynamics. Ion dynamics come primarily from the non-linear ponderemotive force generated by the axial electric field associated with the instability which is given by Eqn 68.

$$F_x \sim \nabla_x |E_x|^2 / 8\pi \tag{68}$$

It is important to understand why the axial gradient in the first order electric field is generated. In the beam-plasma system the electron beam is injected from the cathode end and travels through the plasma until it hits the anode. The instability is thus first created at the cathode end and it propagates through the plasma as it grows. Thus a wave front at the anode end has more time to grow compared to a wave front closer to the cathode end. This results in an electric field that is largest at the anode end. The consequence is an axial gradient which is proportional to twice the axial wavenumber. Since the magnitude of the electric field is largest at the anode end, the ponderomotive field pressure is also the highest at this location. Due to this field pressure plasma electrons with their small inertia are the first to be displaced, setting up an ambipolar field which causes the ion density to be locally depleted as well. Fig.28 shows the formation of the Ion Cavity both in EDIPIC and LSP simulations.

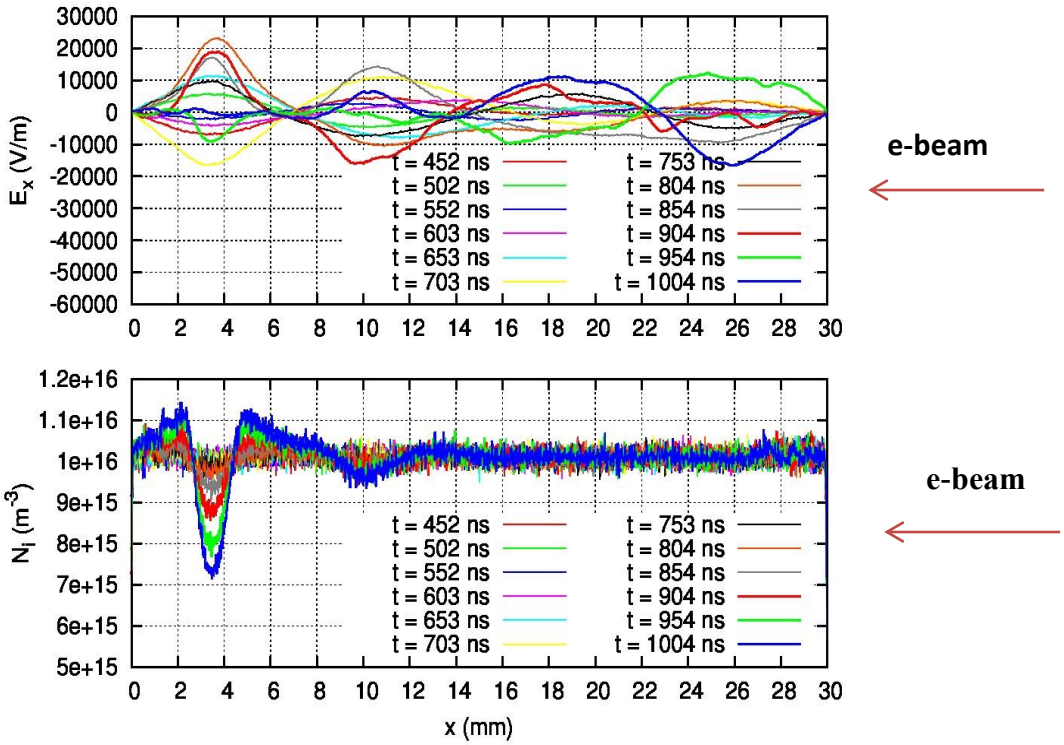

Fig.28.a. E_x-field and N_i (ion density)slices for mass = 20 amu. Ion cavity formation at the peak of two stream standing wave due to ponderomotive force from EDIPIC simulation. Note the cavity starts forming at the anode end where the field is the largest.

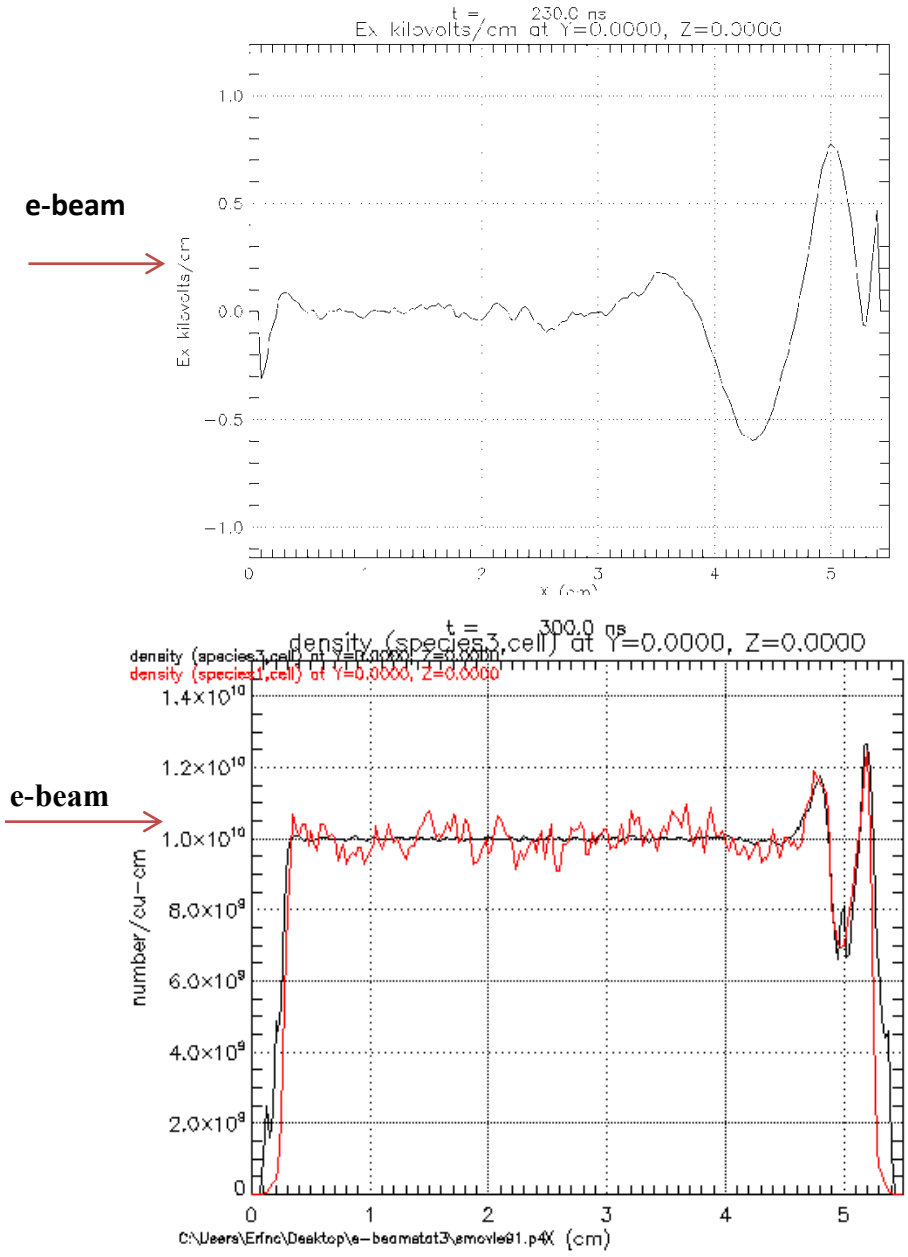

Fig.28.b. Top: Axial Electric Field vs axial position t = 230 ns, Bottom: Ion Density (Black), plasma e- density (red) vs x. Left t= 300ns showing Ion Cavity formation at the anode end from the LSP simulation.

Once the ion cavity is formed, it propagates as an Ion Acoustic wave towards the cathode end. Fig.29 shows the propagation of the IA mode through the plasma from the LSP simulation as a perturbation in the ion density.

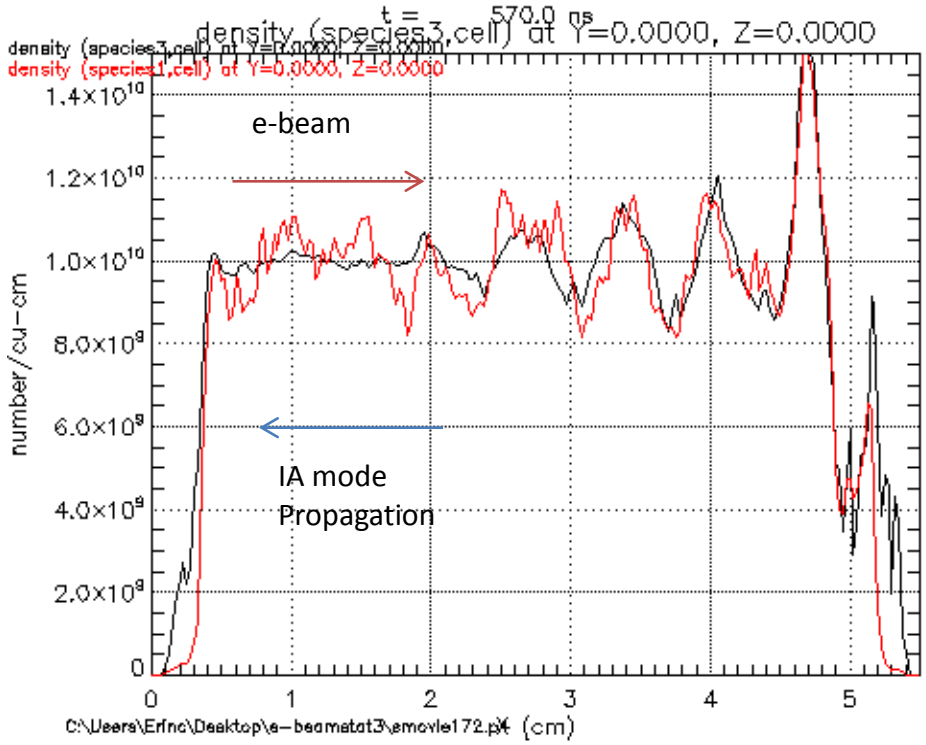

Fig 29. Plasma density vs position at t=570 ns from LSP simulation. Red is electron and black is ion density. Excitation and propagation of IA mode from the anode end to the cathode is evident.

Using a spatial array of probe diagnostics in the simulation, the propagation of the IA mode can be tracked and its phase velocity can be measured. Fig.30. shows the ion density and electric field recorded by an array of probes versus simulation time performed during the

EDIPIC simulation. Table 6. shows the comparison of the measured phase velocity versus C_s, the ion acoustic speed.

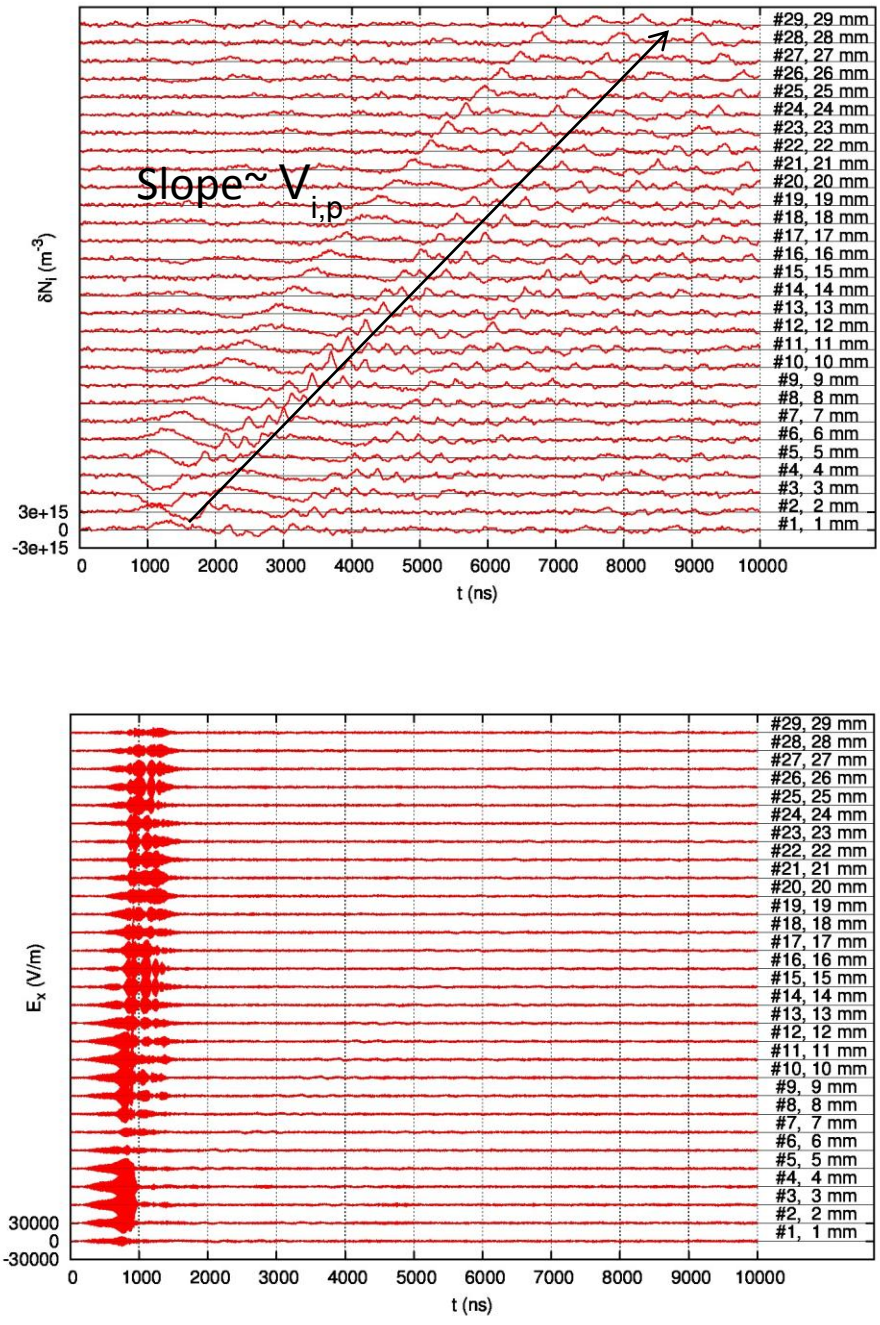

Fig.30. Top: Ion Density at Probe Location vs time. Bottom: Axial Electric Field at Probe location vs time.

M_i (amu)	T_e (eV)	C_s (m/s)	$V_{i,p}$(m/s)	$V_{i,p}$ / C_s
10	**2**	**4390**	**5200**	**1.18**
20	**2.3**	**3330**	**3714**	**1.11**
40	**2**	**2195**	**2800**	**1.28**
60	**2.25**	**1901**	**2333**	**1.3**
80	**2.1**	**1590**	**2131**	**1.34**

Table 6. Measurement of Ion Acoustic Mode phase velocity and comparison with the sound speed for different ion species and electron temperature performed in EDIPIC.

5.2 2-D Simulation of an Electron Beam Propagating in Background Plasma

I- Introduction

One major short coming of EDIPIC in modeling beam-plasma systems is that this code is 1-D, although a 2-D version of the code is now being developed. To study the effects of two-stream instability in a beam-plasma system, we carried out further simulations using LSP in Cartesian 2-D coordinates. The system size and beam-plasma parameters were chosen to replicate a real low-temperature device [54,55]. In Sect. II a brief summary of simulation and beam-plasma parameters for this two-dimensional numerical investigation is presented.

The two dimensional simulation replicates the major results of the 1-D study, in terms of the excitation of the two-stream instability between beam and plasma electrons, the particle trapping of this mode and the consequent saturation and the parametric development of ion cavities and excitation of IA modes due to the non-linear ponderomotive force generated by the axial electric field. However it extends the 1-D simulation results in the discovery of the excitation of oblique plasma waves the spectrum of which evolve in time, suggesting correlation and potentially mode coupling between waves with different two-dimensional wave numbers. This turbulent spectrum demonstrates an interesting time evolution which will be discussed in detail in Sect. III. A very important result of modes with oblique mode numbers is that these modes have associated transverse electric fields which result in transverse collisionless scattering of the beam electrons. Consequently the distribution function of the beam electrons evolve in

time, in parallel with the evolution of the k-spectrum. This interesting result will be discussed in more detail in Sect. IV. The results of this study were presented in various conferences[55-60].

II- Setup of Simulations

As mentioned earlier, the parameters for the 2-D LSP simulation were chosen to replicate a real low-temperature device descried in Ref. 54, 55 Table 7 summarizes the beam-plasma parameters and the simulation settings such as the solver, grid size and time step used for this numerical investigation.

- T = 600 ns, Δt = 0.002 ns,
- $\Delta x = \Delta z = 0.003$ cm, 400 cells in each direction.
- Electrostatic Alternating Direction Implicit Solver, Static ADI is used.
- H+ plasma $n_p = 1 \times 10^{10}\ /cm^3$, e-beam $n_b = 1 \times 10^{10}\ /cm^3$
- KE = 30 eV directed axial energy for beam electrons
- T = 0 eV for all 3 species.
- Collisionless Plasma Model,Beam Injection Model

Table 7. Summary of Parameters and Settings for the 2-D LSP simulation of the e-beam plasma system.

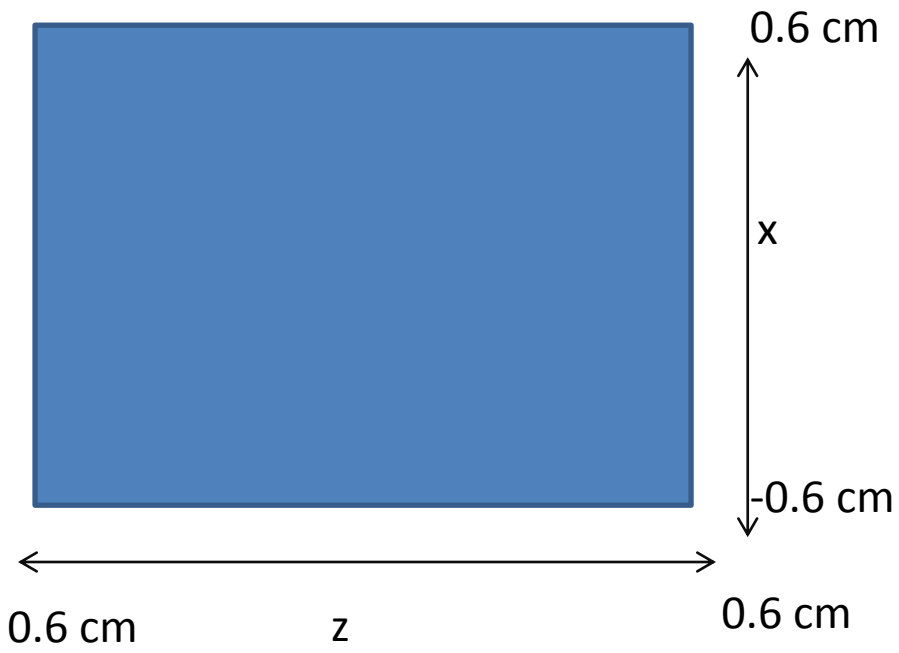

Fig. 31. Depiction of the Physical Simulation Domain and the coordinates used. The beam is injected parallel to the z-axis from the left (cathode) to the right (anode). The beam thickness is 1.2 cm in total, equaling the width of the background plasma.

In Fig.31 we provide a brief description of the physical system and the coordinate system used in this simulation. It is important to note that the beam thickness is chosen to be 1.2 cm in total, which equals the entire width of the background plasma in x-direction, in order to avoid edge related gradients to scatter beam electrons transversely. Since the collisionless plasma model is used, any scattering that is observed is purely due to the transverse electric field associated with the Langmuir turbulence.

III- Excitation of Oblique Modes and Evolution of the K-Spectrum

In this section we will present the results from the 2-D simulation run using contour plots of the scalar potential taken at different times and the k-space discrete Fourier transforms of the scalar potentials performed using MATLAB signal processing toolbox using the built-in two dimensional fast fourier transform function, fft2. We will use $\tilde{\phi}$ to denote the k-space transform of scalar potential ϕ. The k-space transform of $\tilde{\phi}$ is given by:

$$\tilde{\phi}(k_{\perp}, k_{\parallel}) = \sum_{x,y} \phi(x,z)\exp(ik_{\perp}x + ik_{\parallel}z) \qquad (69)$$

Note since $\tilde{\phi}$ is a complex quantity with phase information in contour plots we will plot it's magnitude, corresponding to the amplitude of the signal versus position as usual. The phase space of particle velocities versus axial (z) and transverse (x) coordinates are also provided at the sampling times in order to provide an understanding of the current state of the instability in terms of linear growth, saturation and dissipation.

At t=25 ns inspecting Fig.32 we see a fully developed axial Langmuir wave. The contour plot of $|\tilde{\phi}|$ reveals that the mode is primarily axial, with $k \sim k_{res} \sim 55\ cm^{-1}$. The peak amplitude of fluctuations is less than 10V. The phase space from this time slice reveals that the mode has already saturated by the wave-particle trapping of beam electrons at this stage.

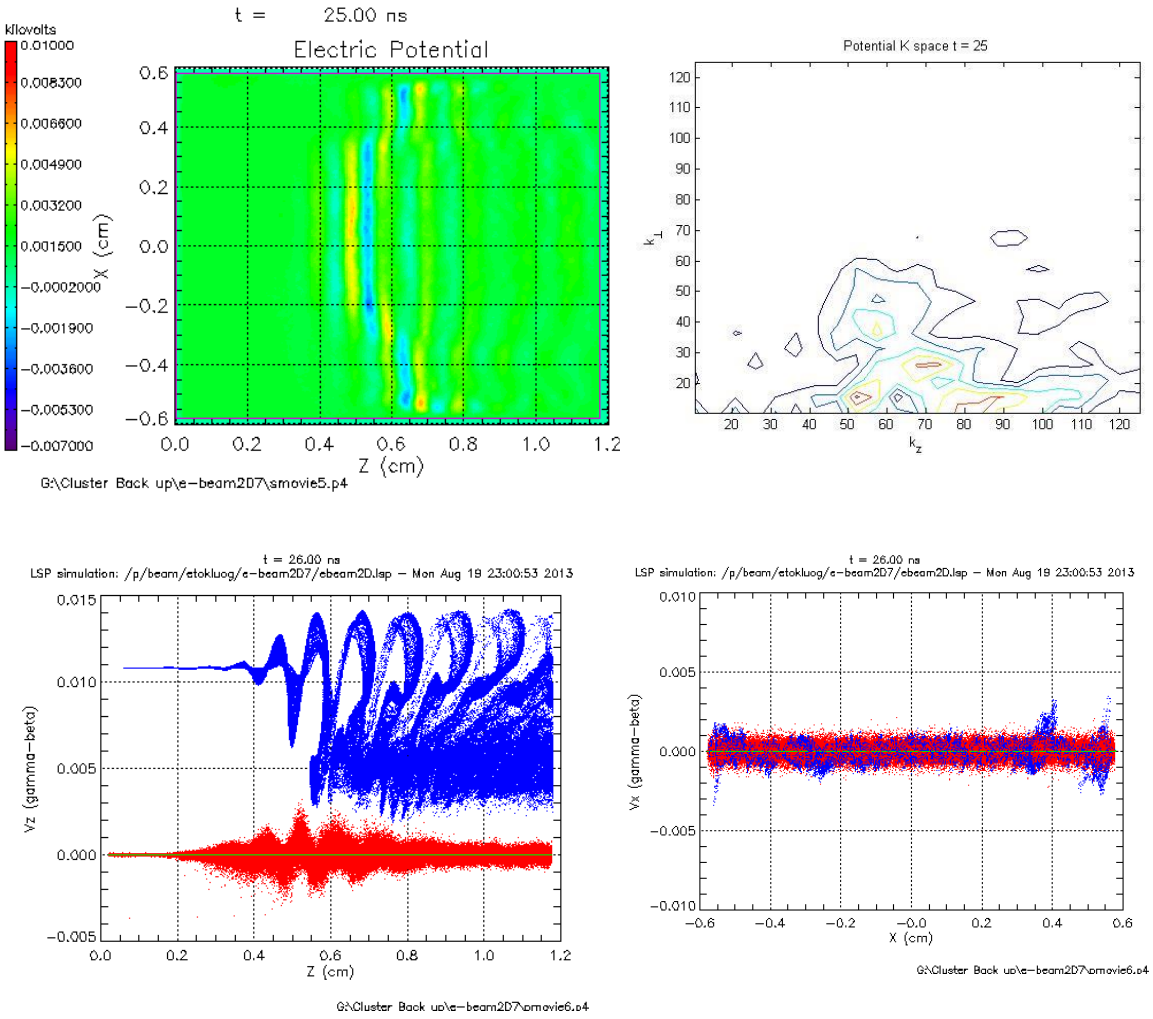

Fig.32. Top, Left: Potential Contour Plot t=25 ns. Right: Potential K space spectrum t= 25 ns. The k-spectrum has peaks at (50, 15) and (70, 30) 1/cm.

Bottom, Red: Plasma Electrons, Blue: Beam Electrons. cm z=[0.2,0.4] cm Left: Vz vs z x =[-0.4, 0.4] . Right: Vx vs x. z =[0.3, 0.7]. Instability has saturated by particle trapping.

At t= 100 ns the system has gone into a turbulent state. It is evident from the contour plots of the scalar potential that there are a several coexisting oblique modes. The spectral analysis of the turbulence reveals that the peak of the spectrum has shifted to an oblique mode with $(k_{\perp}, k_{\parallel}) \sim (30,30)\ cm^{-1}$ with a peak amplitude of around 10V. There are modes with smaller amplitudes at (25, 50) cm^{-1} and (40,60) cm^{-1}. The phase space shows that the turbulence is stronger at the anode end, the axial velocity of particles demonstrate a turbulent state and the transverse velocity clearly has spatial structures which correspond to the transverse components of the oblique modes. Fig. 33 demonstrates the above mentioned key results.

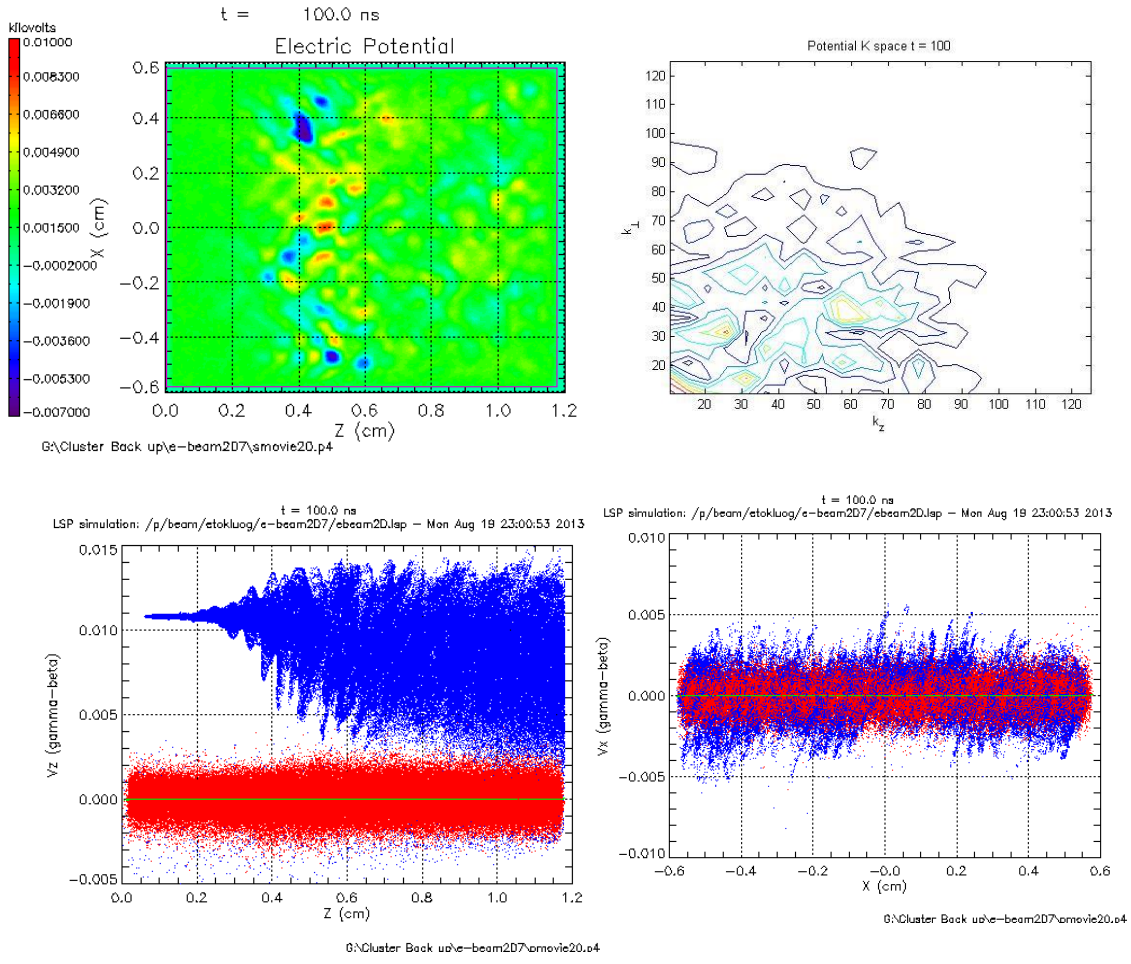

Fig.33. Top, Left: Potential Contour Plot t=100 ns. Right: Potential K space spectrum t= 100 ns. The peak of the k-spectrum has shifted to ~(30,30) 1/cm

Bottom, Red: Plasma Electrons, Blue: Beam Electrons. cm z=[0.2,0.4] cm Left: Vz vs z x =[-0.4, 0.4] . Right: Vx vs x. z =[0.3, 0.7]. Spatial Modulation of Vx is observed.

At t = 200 ns the turbulence has fully developed. The mode at (30,30) cm^{-1} is the most dominant mode at this stage with an amplitude of 10V, there is another strong low k mode at (15,15) cm^{-1} and the mode at (35,50) cm^{-1} is still present although at a weaker state. The spectrum demonstrates a clear energy flow from high k axial modes to low k oblique modes. The wavenumbers for these modes are commensurate. This suggests a correlation between the modes in the lines of 3-wave coupling, however the frequencies associated also have to be commensurate with requires further spectral analysis in the time-frequency domain. However the non-linear nature of the dispersion relation implies that one of these modes should not be a Langmuir wave. This will require the simulation to be rerun with a grid of point probe diagnostics to capture time domain signals. The phase space also confirms that the state of the system is strongly turbulent and as in t= 100 ns the transverse velocity of particles reveal spatial structures indicative of the presence of fluctuations with transverse components. Fig.34. demonstrate the above mentioned key results.

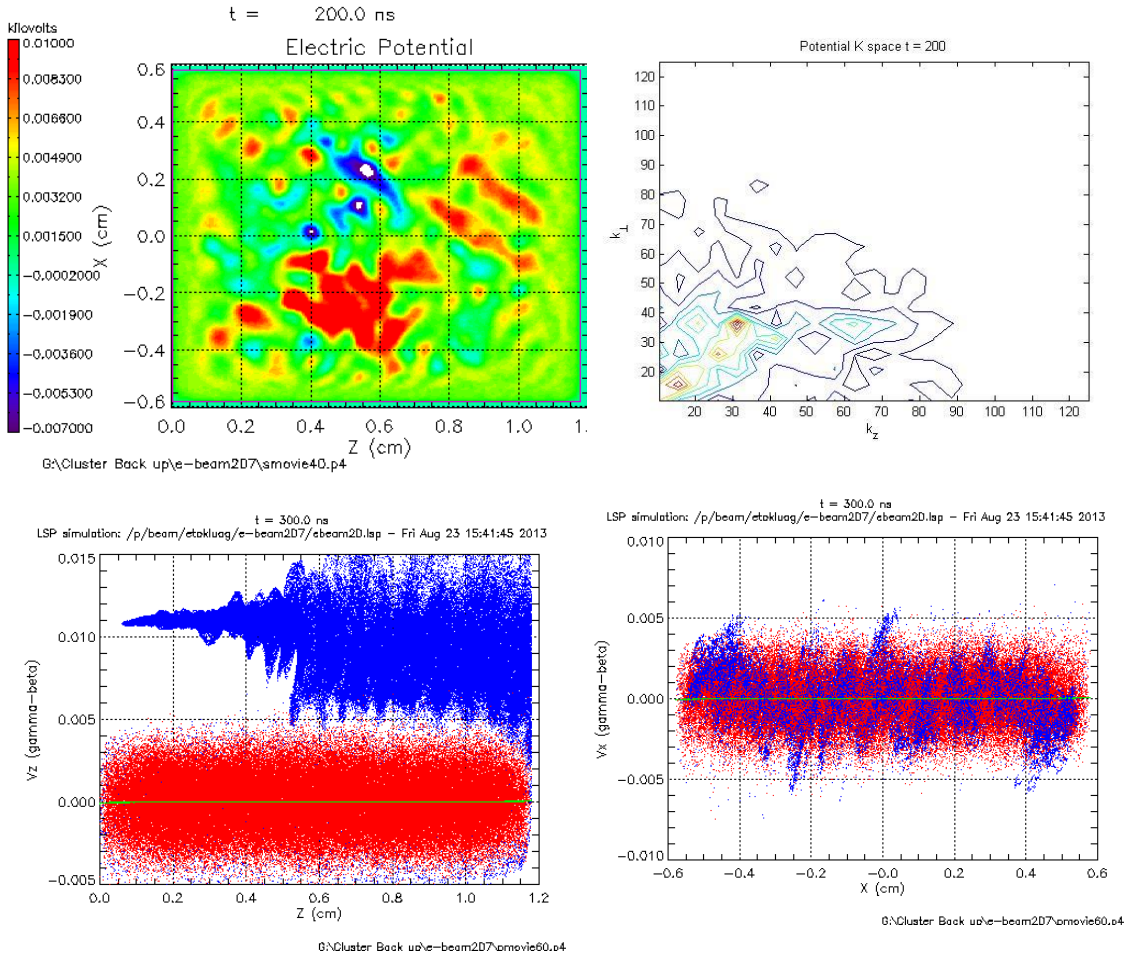

Fig.34. Top, Left: Potential Contour Plot t=25 ns. Right: Potential K space spectrum t= 25 ns. The k-spectrum has peaks at ~(15,15), (30,30) and (35,50) 1/cm
Bottom, Red: Plasma Electrons, Blue: Beam Electrons. cm z=[0.2,0.4] cm Left: Vz vs z x =[-0.4, 0.4] . Right: Vx vs x. z =[0.3, 0.7]. Spatial Modulation of Vx is observed.

The data taken at t = 300 ns of the simulation reveals some interesting results. At this stage the turbulence starts to weaken. This can clearly be seen in the phase space. The (30,30)

and (15,15) modes still coexist with peak amplitudes around 8V. As we will describe in detail in the next section, the weakening of the turbulence results in less collisionless scattering of beam electrons. Fig.35 displays the scalar potential and phase space data taken at t = 300 ns.

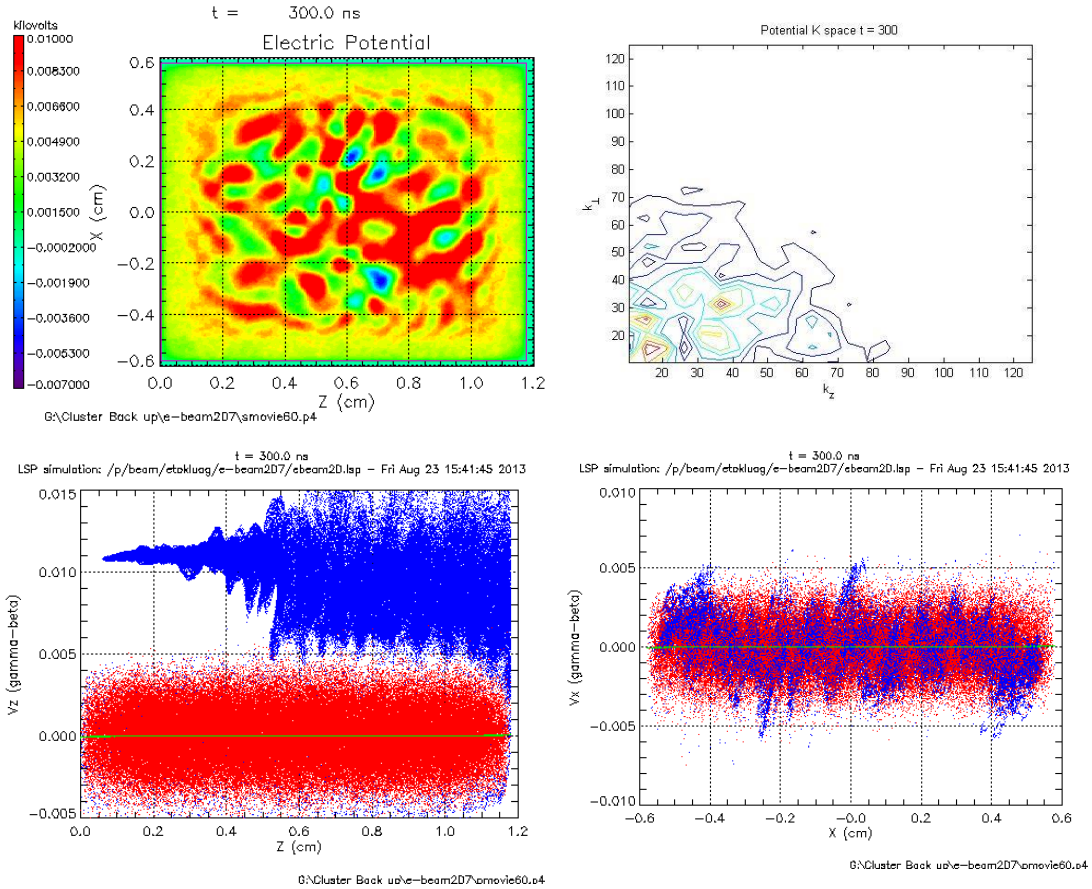

Fig.35 Top, Left: Potential Contour Plot t=300 ns. Right: Potential K space spectrum t= 300 ns. The k-spectrum has peaks at (15,15), (15,25) and (40,30) 1/cm

Bottom, Red: Plasma Electrons, Blue: Beam Electrons. cm z=[0.2,0.4] cm Left: Vz vs z x =[-0.4, 0.4] cm . Right: Vx vs x. z =[0.3, 0.7] cm. Spatial Modulation of the transverse velocity is still evident.

At the final stage of the simulation the turbulence continues to weaken and the resulting collisionless scattering is also reduced. The k-spectrum demonstrates a very interesting time

evolution as the low k modes at (15,15) and (30,30) cease to exist and are replaced by a dominant higher k oblique mode at (40,45) cm^{-1}. The presence of a single dominant mode is also evident observing the contours of the scalar potential as wave fronts traveling at almost a 45 degree angle are clearly visible. Fig.36. presents the data taken at t= 500 ns of the simulation.

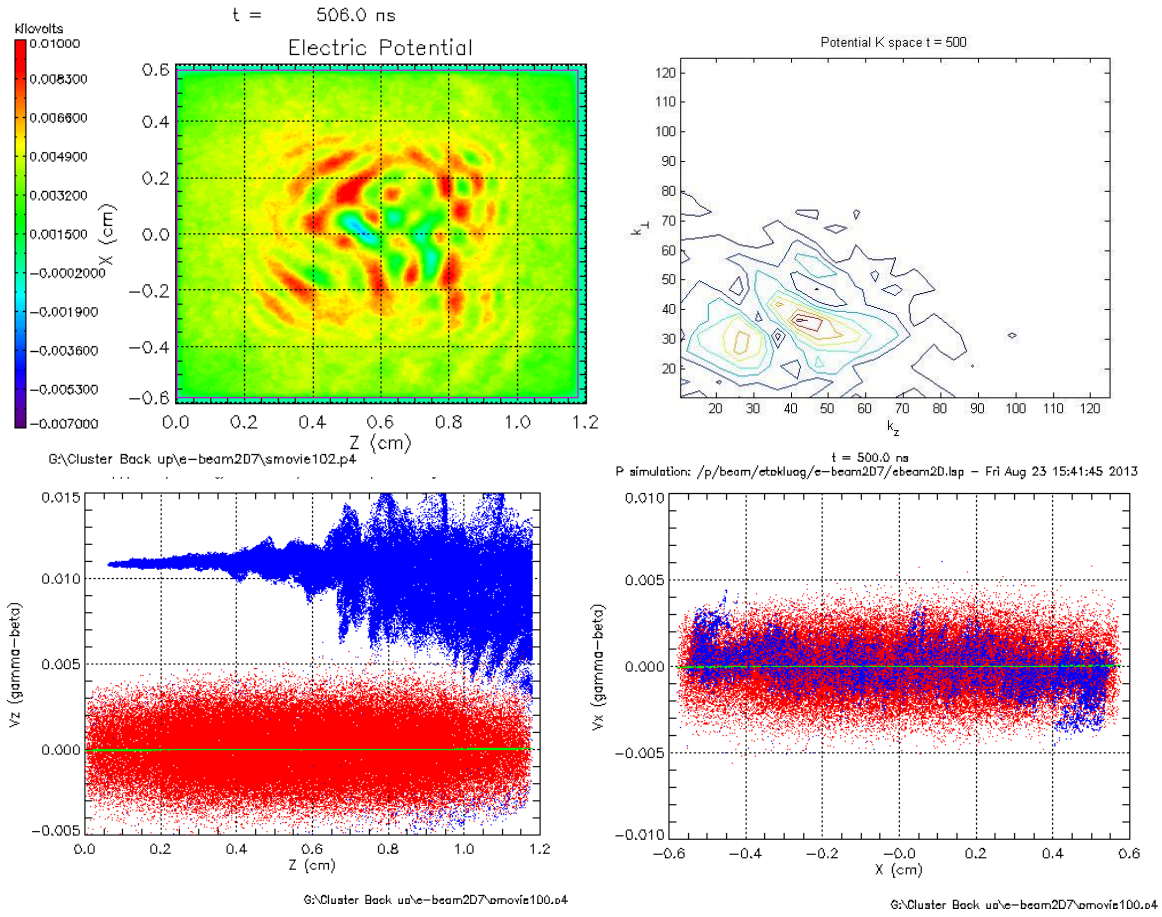

Fig.36 Top, Left: Potential Contour Plot t=500 ns. Right: Potential K space spectrum t= 500 ns. The low k peaks disappear. Spectral maximum is at (40,45) 1/cm.

Bottom, Left: Potential Contour Plot t=500 ns. Right: Potential K space spectrum t= 500 ns

IV-Collisionless Scattering and Ion Dynamics:

One important result of the excitation of oblique modes is the collisionless transverse scattering of electrons. This is important in the understanding of energy transverse from the beam to the plasma and the evolution of electron distribution functions for both plasma and beam electrons which become anisotropic, which was studied theoretically and demonstrated experimentally [54,55].

In order to capture this physical affect the simulation is set using the collisionless plasma model. Thus any transverse or axial scattering we will observe in the V_x vs V_z phase space is purely due to the Lorentz force created by the electric field. In order to minimize the edge effects of the beam and plasma profiles we have chosen the beam width to span the entire length of the plasma, as the edge gradients will generate fields that will also scatter particles. To study the collisionless scattering associated with the oblique modes of the turbulence, the data presented in the section will be taken at the center of the plasma transversely x = [-0.4, 0.4] cm the entire width of the system being x = [-0.6, 0.6] cm. The simulation domain is divided into 3 parts axially: region 1 the cathode z = [0.2,0.4] cm, region 2 mid-plasma z = [0.5,0.7] cm and region 3 the anode z = [0.8,1.0] cm. The entire length of the system is z = [0.0, 1.2] cm.

Looking at Fig.37.a. we can observe the V_x vs V_z phase space taken at the above described 3 regions of the simulation domain. Both the plasma electrons (red particles) and the beam electrons (blue particles) are initially cold, having delta function like distribution functions which is evident in the cathode region. In the mid-plasma and anode regions due to the presence

of the resonant axial Langmuir mode the particles scatter axially. Since beam electrons in the anode region have traversed the entire length of the plasma, they are exposed to the fields for a longer duration of time and thus are scattered more. This is a common feature that we will observe in all 5 time slices.

The state of the velocity phase space at t = 100 ns can be seen in Fig.37.b. Due to the excitation of oblique modes, the beam and plasma electrons are scattered transversely. It is important note that each dot represents an individual particle in the Fig.37. By collecting particles and sorting them in velocity bins it is possible to extract the particle distribution function. The transverse scattering is more pronounced at the anode end due to the longer time of exposure to the fields for the beam electrons and due to the fact that turbulence is stronger at the anode end since the wavefronts also had more time to grow. Thus both the plasma and the beam electrons are scattered more at this region. The velocity spread in the transverse direction has tripled compared to its state at t= 25 ns.

a-

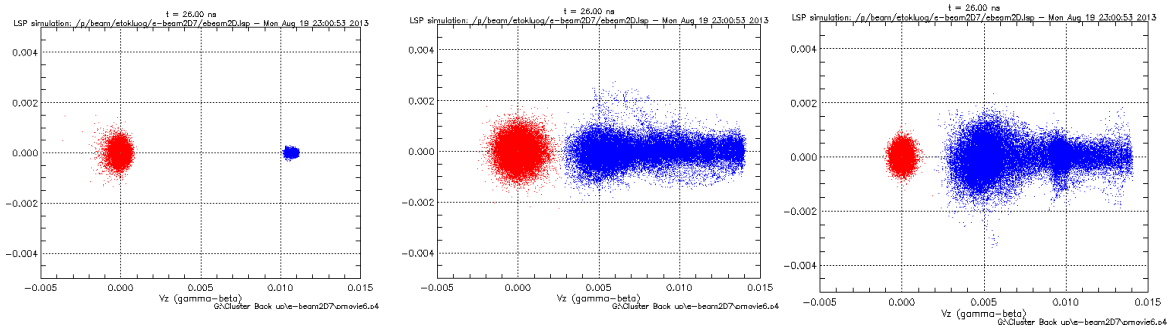

b-

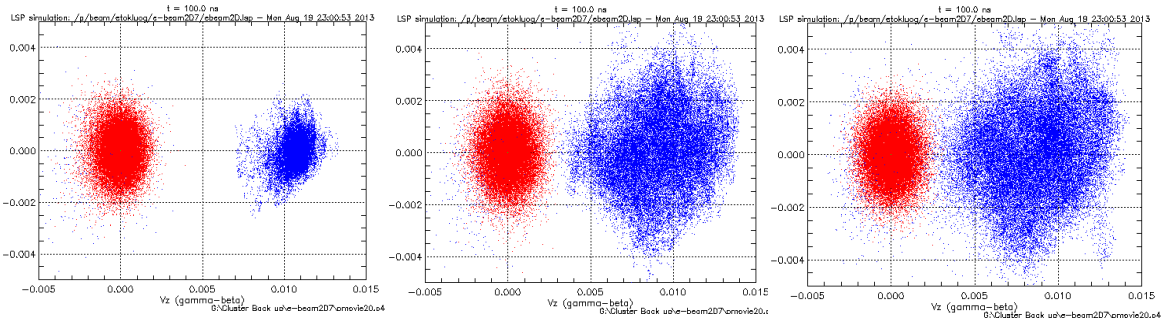

c-

d-

e-

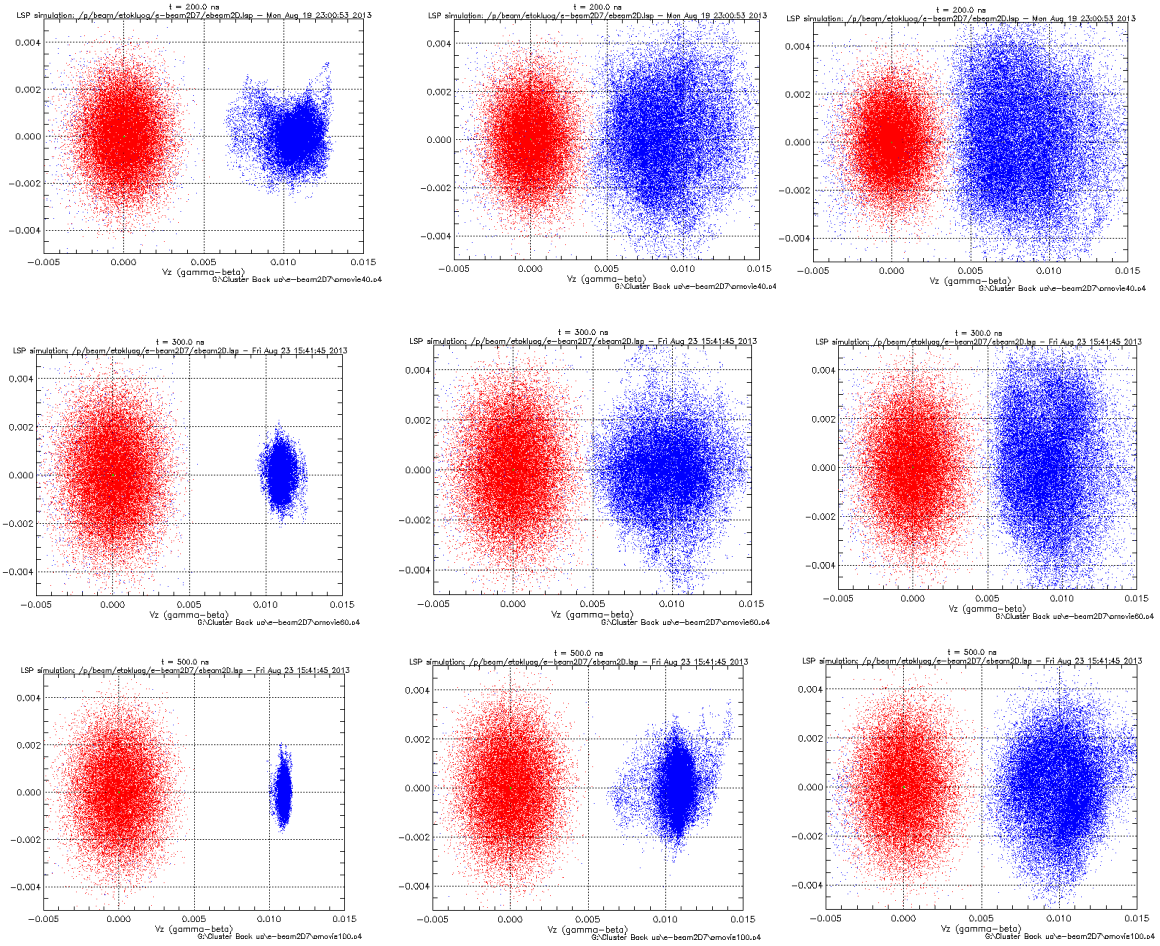

Fig. 37. Red: Plasma Electrons, Blue: Beam Electrons. Left: Region 1 x =[-0.4, 0.4] cm z=[0.2,0.4] cm. Middle: Region 2, x =[-0.4, 0.4] cm z=[0.5,0.7] cm. Right: Region 3 x =[-0.4, 0.4] cm z=[0.8,1.0] cm.a- t = 25 ns, b- t = 100 ns, c- t = 200ns, d- t = 300 ns and e- t= 500 ns.

At t = 200 ns, the turbulence is in a strong state. The velocity spread of the particles become spherical due to significant transverse scattering due to the presence of several coexisting low-k oblique modes, the (15,15) 1/cm and (30,30) 1/cm modes being the most dominant, as can be seen in Fig.37.c. At t= 300 ns the turbulence starts to weaken and the scattering is also reduced as can be seen in5.14.d. At t= 500 ns the state of the beam plasma system is almost non-turbulent with a dominant high-k oblique mode. The reduction of the turbulence has immediate consequences in the scattering of the particles. As can be seen in

Fig.37.e the scattering in all three regions of the simulation domain has been significantly reduced compared to the t= 200 ns and t= 300 ns states. Since fresh beam particles are injected during the simulation, the reduction of transverse scattering is mostly easily observed in the beam electrons.

The time evolution of the turbulent spectrum is clearly correlated with the strength of the collisionless scattering that the particles experience. When the system is a strongly turbulent state with coexisting low k modes, the distribution functions of the electrons are significantly altered. When the turbulence weakens and is dominated by a high-k mode towards the end of the simulation consequently the transverse scattering is reduced. It is important to understand the time evolution of the spectrum and the interaction the modes with each other as it is evident that the modes are immediately responsible for the collisionless scattering of beam and plasma particles and the collisionless heating of the plasma which is an important mechanism of power delivery from the beam to the plasma. This analysis will require further investigation as continuation of this work.

Chapter 6:

Conclusion:

In this work we have investigated two major instability driven non-linear mechanisms that relate to the main branches of research in plasma physics: magnetic confinement and inertial fusion. The initial part of this work was a theoretical study of the non-linear saturation mechanism of slab Electron Temperature Gradient (ETG) modes. In toroidal geometry the modes can be responsible for the high levels of anomalous transport observed in tokamaks. Supported by the experimental evidence from the Q-Machine CLM a theoretical model based on the non-linear interaction of stable and unstable modes in the form of 3-wave coupling was determined, with the 3rd partner of the triplet being an IA mode. This model explains the high correlation levels observed between the modes, correctly estimates the frequency difference between the stable and unstable ETG radial harmonics and produces a saturation level which is ~ 10% of the electron temperature that is consistent with experimental observations in the CLM.

The second part of this thesis focuses on the numerical studies of beam-plasma interactions conducted in Princeton Plasma Physics Laboratory under the supervision of Dr. Igor Kaganovich of the Non-Neutral group. We investigated the effects of the non-linear time-averaged fields generated by two-stream instability in the case of an ion-beam propagating in background plasma. The investigation revealed that the saturation mechanism of the instability is either the trapping of plasma electrons or beam ions depending on beam-plasma parameters such

as beam and plasma density as well as the beam ion mass. The saturation mechanism is directly correlated with the amplitude of electron oscillations in phase space. The time-averaged electron oscillations are directly responsible for creating a non-linear reversed magnetic field and the radial gradient of the squared magnitude of the oscillations are responsible for the creation of a radial ambiploar defocusing electric field in the form of a ponderomotive force. Hence the magnitude of the non-linear fields depend directly on the choice of beam density, plasma density and ion mass. We summarized this dependence in the form of a unitless parameter which we named α. Using particle-in-cell simulations we have demonstrated the dependence of these non-linear defocusing fields on these parameters and investigated the scaling. We have determined that in the transition region where the instability saturation mechanism switches from electron trapping to ion trapping or vice versa, the defocusing fields are maximized, a result that we confirmed analytically and also with the numerical solution of the underlying Ampere's Law for the vector potential. The identification of a maximal defocusing region in the parameter space gives important insight to experimentalists in the design of future inertial fusion devices that may be subject to the two-stream instability. The investigation was further carried to propose a diagnostic tool to detect the instability in High Energy Density and Heavy Ion Fusion devices. The convective nature of the instability makes it difficult to detect and study in heavy ion systems, especially when the distortion of the beam profiles are less pronounced due to the higher inertia of the beam ions. However in the case a small radius beamlet, the distortion and defocusing is much more easily observed as the percentage of change in the spot size is increased. Proof-of-concept simulations with parameters similar to the NDCX-II experiment were performed and it was shown that beamlets extracted from the beam and propagated in

background plasma an equal distance as the original beam can be used to diagnose the two-stream instability simply by tracking the beamlet spot size.

Finally we extended the study of beam-plasma interactions to electron beams. The particle-in-cell code LSP was initially used to benchmark 1-D simulations performed by Dimitri Sydrenko from University of Alberta. Important observations made include the dependence of the excitation of the instability on the plasma density and system size, collisionless heating of the plasma and the coupling of the electron-electron two stream instability to ion cavities and ion acoustic modes through non-linear ponderomotive force. The results from the two codes were shown to be in close alignment. LSP was then later used to simulate a low temperature experimental device in a 2-D setting. Many of the main results from the 1-D simulations were again confirmed. The 2-D simulations further revealed the excitation of oblique modes with transverse mode numbers, which result in transverse fields. These fields were shown to collisionlessly scatter beam and plasma electrons. The evolution of the turbulent spectrum was studied using Fourier transform techniques. The time evolution suggest interaction and power transfer between the modes, which can be non-linear as in the case of three wave coupling. However further investigation both in simulation and in theory to understand the evolution of this turbulent spectrum. The study of two-stream instability dependent dynamics is important to understand to power delivery and collisionless scattering in low temperature beam plasma devices which has applications in low temperature plasma etching and materials processing.

References:

[1] E.K. Tokluoglu, V.Sokolov and A.K. Sen, Phys. Plasmas **19** , 102306 (2012)

[2] Parker S.E. and Sen A.K. 2002 *Phys. Plasmas* **9** 3440

[3]W.W.Lee, "Long time simulations of microturbulence," Bull. Am. Phys. Soc. 51-2, 111 (2006)

[4] Jenkins, Lee, Phys. Plasmas 14, 032307 2007

[5] W. Horton, Rev. Mod. Phys. **71**, 135 (1999).

[6] W.W.Lee PSACI PAC Meeting Presentation June 2007

[7] Brower, D. L., W. A. Peebles, and N. C. Luhmann, Jr., 1985, Phys. Rev. Lett. 54, 689.

[8] Mazzucato et.al. 1996, Phys. Rev. Lett. 77, 3145.

[9] R. Scarmozzino, A. K. Sen and G. A. Navratil, Phys. Fluids **31 (6)**, 1773 (1988).

[10] X.Wei, V.Sokolov, and A.K. Sen, Phys. Plasmas **17**, 042108 (2010).

[11] B. B. Kadomtsev, in Reviews of Plasma Physics, edited by M. A. Leontovich (Consultant Bureau, New York, 1970), Vol. 5, 309.

[12] B. Coppi and G. Rewoldt, in Advances in Plasma Physics, Edit by A. Simon and W.B. Thompson (John Wiley and Sons, New York, 1976), Vol. 6, 421.

[13] W. Dorland, F. Jenko and M. Kotschenreuther and B.N. Rogers, *Phys. Rev. Lett.* **85**, 5579 (2000)

[15] R. E. Waltz, J. Candy and M. Fahey, *Phys. Plasmas*, **14**, 056116 (2007)

[16] Y. C. Lee, J. Q. Dong, P. N. Guzdar and C. S. Liu, *Phys. Fluids* **30 (5)**, 1331 (1987)

[17] W. Horton, B. G. Hong and W. M. Tang, *Phys. Fluids* **31** (10), 2971 (1988)

[18] Z. Lin, L. Chen and F. Zonca, *Phys. Plasmas* **12**, 056125 (2005)

[19] W. M. Nevins, J. Candy, S. Cowley, T. Dannert, A. Dimits, W. Dorland, C. Estrada-Mila, G. W. Hammett, F. Jenko, M. J. Pueschel and D. E. Shumaker, *Phys. Plasmas* **13**, 122306 (2006)

[20] *W. Horton, H. V. Wong, P. J. Morrison, A. Wurm, J. H. Kim, J. C. Perez, J. Pratt, G. T. Hoang, B. P. LeBlanc and R. Ball*, *Nucl. Fusion* **45**, 976 (2005)

[21] *E. Z. Gusakov, A. D. Gurchenko, A. B. Altukhov, A. Yu. Stepanov, L. A. Esipov, M. Yu. Kantor and D. V. Kouprienko*, Plasma Phys. Control. Fusion **48**, A371 (2006).

[22] L. Schmitz, A. E. White, T. A. Carter, W. A. Peebles, T. L. Rhodes, K. H. Burrell, W. Solomon and G. M. Staebler, Phys. Rev. Lett. 100, 035002 (2008).

[23] E. Mazzucato, D. R. Smith, R. E. Bell, S. M. Kaye, J. C. Hosea, B. P. LeBlanc, J. R. Wilson, P. M. Ryan, C. W. Domier, N. C. Luhmann, Jr., H. Yuh, W. Lee and H. Park, Phys. Rev. Lett. 101, 075001 (2008).

[24] W.Horton *et al*, Transport Task Force Workshop, San Diego, California (2011).

[25] R. Scarmozzino, A. K. Sen and G. A. Navratil, Phys. Fluids **31 (6)**, 1773 (1988).

[26] X.Wei, V.Sokolov, and A.K. Sen, Phys. Plasmas **17**, 042108 (2010).

[27] Kim Y.C. and Powers E.J. 1979 *IEEE Trans. Plasma Sci.* **7** 120

[29] V.Sokolov and Sen A.K. Nucl. Fusion **45** (2005) 439–449

[30] Weiland J. 2000 *Collective Modes in Inhomogeneous Plasma* (Bristol: Institute of Physics Publishing)

[31] Kim S.Y. and Sen A.K. 1985 *Phys. Fluids* **28** 3287

[32] Hasegawa A. and Mima K. 1977 *Phys. Rev. Lett.* **39** 205

[33] LSP Manual, LSP is a software product of Vosscientific (www.vossci.com), Alburquerque, NM 87108

[34] D.R. Welch et al. Journal of Computational Physics 227 (2007) 143–155

[35] LSP Particle-in-Cell Techniques, D.R.Welch et.al. Vosscientific (www.vossci.com), Alburquerque, NM 87108, PPPL (2013)

[36] D.R.Welch et.al. Phys.Plasmas **13**, 063105 (2006)

[37] 1. R.N. Sudan, Physical Review Letters. **37**, 1613 (1976)

[38] 2. K.W. Lee and J.Buchner, Physics of Plasmas **17**, 042308 (2010)

[39] 3. F.W. Chambers, Physics of Fluids **22,** 483 (1979)

[40] 4. M. Masuzaki, K. Kamada and H. Shirataki, Journal of Physical the Physical Society of Japan **56**, 1274, (1987)

[41] 5. E.A.Startsev, I.D. Kaganovich and R.C. Davidson (to be published), European Physical Journal (2013)

[42] 6. LSP is a software product of Vosscientific (www.vossci.com), Alburquerque, NM 87108.

[43] 7. E.A.Startsev, I.D. Kaganovich and R.C. Davidson (to be published), Heavy Ion Fusion 2013

[44] 8. I. D. Kaganovich, R. C. Davidson, M. A. Dorf, E. A. Startsev, A. B Sefkow, A. F. Friedman and E. P. Lee, Physics of Plasmas **17**, 056703 (2010).

[45] Erinc Tokluoglu, Edward A. Startsev, Igor Kaganovich and Ronald C. Davidson . BAPS.2012.DPP.JO7.4

[46] Erinc Tokluoglu, Edward A. Startsev and Igor Kaganovich, to be submitted New Journal of Physics (2014)

[47] Erinc Tokluoglu, Edward A. Startsev and Igor Kaganovich, to be submitted Phys.Rev.Lett (2014)

[48] Edward A. Startsev, Igor Kaganovich, Ronald C. Davidson and Erinc Tokluoglu, Effects of Beam Plasma Instabilities on Neutralized Propagation of Intense Ion Beams in Background Plasma, Internation Symposium on Heavy Ion Fusion (2012)

[49] L. Chen and M. Funk, Langmuir wave standing wave resonance in DC/RF plasma, Proceedings of ICRP 2010.

[50] D. Sydorenko, *et al*, Phys. Plasmas, **14,** 013508 (2007).

[51] D. Sydorenko, *et al*, Phys Rev Lett., **103**, 145004 (2009).

[52] I.D. Kaganovich et.al. Excitation of Ion Acoustic Waves by Electron Beams, DOE PSC (2012).

[53] Dmytro Sydrenko, Erinc Tokluoglu, Edward A. Startsev, Igor Kaganovich and Ronald C. Davidson BAPS.2012.DPP.TP8085S

[54] Mustafaev, Technical Physics, Vol. 46, No. 4, 2001, pp. 472–483. Translated from Zhurnal Tekhnichesko Fiziki, Vol. 71, No. 4, 2001, pp. 111–121.

[55] Mustafaev and Mezentsev, J.Physics D: Appl. Phys. **19** (1986) L69-L73

[56] Erinc Tokluoglu, Alexander Khrabrov and Igor Kaganovich DOE PSC 2013.

[57] Erinc Tokluoglu, Alexander Khrabrov and Igor Kaganovich, BAPS.2013.GEC.MR1.16

[58] Igor Kaganovich, Dmytro Sydorenko, Erinc Tokluoglu, Edward A. Startsev and Ronald C. Davidson BAPS.2013.DPP.TM10.9